SELF-ORGANIZED QUANTUM DOTS FOR SINGLE PHOTON SOURCES

von
DIPLOM-PHYSIKER ERIK STOCK
aus Bremen

Von der Fakultät II – Mathematik und Naturwissenschaften
zur Erlangung des akademischen Grades

Doktor der Naturwissenschaften
-Dr. rer. nat. -

genehmigte Dissertation

Promotionsausschuss:

Vorsitzender: Prof. Dr. Michael Lehmann
Berichter/Gutachter: Prof. Dr. Dieter Bimberg
Berichter/Gutachter: Prof. Dr. Vladimir Haisler

Tag der wissenschaftlichen Aussprache: 03.12.2010

Berlin 2011

D 83

ABSTRACT

Efficient generation of single or entangled photons is the crucial prerequisite for novel quantum key distribution systems and quantum information processing. Single semiconductor quantum dots (QDs) with their unique electronic structure are capable of emitting such photons on demand using pulsed current injection.

In the work at hand self-organized InGaAs/GaAs quantum dots are investigated as sources of single photons both on a fundamental level for understanding of their quantenmechanical properties and in ready-to-use devices. The characterization is done using a micro-photoluminescence and -electroluminescence setup with the required high spatial and spectral resolution. The second order photon correlation function is measured in a Hanbury-Brown Twiss setup equipped with state-of-the-art avalanche photodiodes and new superconducting single photon detectors for increased time-resolution.

Three types of devices each of them representing an important development stages towards a high efficient ultra-fast single photon source are characterized. The first device is a simply pin diode structure with a layer of QDs. A single QD is pumped electrically by applying a bias well below the flatband condition. Concurrent resonant tunneling of electrons and holes can be observed in this device by optical means.

In the second type of devices the maximum pump rate is increased by an AlO_x aperture, which constricts the current to pump only a single QD. This device is the ultimate limit of a light emitting diode (LED) and demonstrates a record pure spectrum with clear single photon emission.

In the third device the out-coupling efficiency and repetition rate is significantly improved by the realization of a resonant cavity LED. This device allows perfect single photon emission at record pumping rates of up to 1 GHz with a twenty times enhanced out-coupling efficiency. Since the optical response is too fast for APDs, new superconducting detectors are used in photon correlation measurements.

Electron-phonon coupling strongly influences the luminescence line shape, dephasing and coherence of the emitted phonons and thereby the most important characteristics of a non-classical light source. In this work, for the first time, the optical and acoustic phonon scattering in a single InGaAs QD is investigated. By comparing experimental data with calculated spectra a quantitative understanding of the line shape and the dominating phonon modes is achieved.

A vanishing fine-structure splitting (FSS) of the exciton bright state is crucial for the generation of entangled photon pairs. A new approach, using QDs on (111) GaAs, to reduce the FSS is investigated. The first spectroscopic study on single QDs grown on (111) GaAs substrates are presented and significant reduction of the FSS for this new kind of QDs is demonstrated.

ZUSAMMENFASSUNG

Die effiziente Erzeugung von einzelnen Photonen oder verschränkten Photonenpaaren ist der Schlüssel für neuartige Quantenkryptografie und Quantencomputer. Einzelne Halbleiter Quantenpunkte (QPe) mit ihren einzigartigen elektronischen Eigenschaften, haben bereits bewiesen, dass sie solche Photonen durch elektrische Pulse erzeugen können.

In der vorliegenden Arbeit werden selbstorganisierte InGaAs/GaAs Quantenpunkte sowohl auf der fundamentalen Ebene als auch in fertigen Bauelementen auf ihre Eignung als Einzelphotonenquelle untersucht. Für diese Charakterisierung wird ein Mikro-Photolumineszenz und -Elektrolumineszenz Aufbau benutzt, der die notwendige Orts- und Spektralauflösung besitzt.

Drei verschiedene Bauelemente werden untersucht, wobei jedes einen bedeutenden Schritt in der Entwicklung zu einer hocheffizienten und sehr schnellen Einzelphotonenquelle darstellt. Im ersten Bauteil, das nur aus einer pin-Struktur besteht, kann ein einzelner QP elektrisch gepumpt werden, indem eine Spannung deutlich unterhalb der Flachband-Spannung angelegt wird. Gleichzeitiges resonantes Tunneln von Elektronen und Löcher in den QP kann mit optischen Methoden nachgewiesen werden. Um die maximale Pumprate zu erhöhen, wird im zweiten Bauelement der Strompfad durch eine AlO_x Apertur auf einen einzelnen QP eingeschränkt. Dieses Bauelement repräsentiert den absoluten Grenzfall einer Leuchtdiode und zeigt ein extrem reines Spektrum mit eindeutiger Einzelphotonencharakteristik.

Durch die Realisierung einer resonanten Kavitäts Leuchtdiode kann die Auskoppeleffizienz und die maximale Wiederholungsrate verbessert werden. Dieses Bauelement zeigt perfekte Einzelphotonenemission bei einer Rekord-Wiederholungsrate von bis zu 1 GHz sowie einer um den Faktor 20 verbesserten Auskoppeleffizienz. Die optische Reaktion dieses Bauteils ist zu schnell für herkömmliche Lawinenfotodioden und es werden daher neuentwickelte supraleitende Detektoren verwendet.

Die Elektron-Phonon Wechselwirkung beeinflusst sowohl die spektrale Linienform, die Dephasierung als auch die Kohärenzlänge des emittierten Photons und damit die entscheidendsten Parameter einer nichtklassischen Lichtquelle. In dieser Arbeit wird um ersten Mal die Wechselwirkung von Exzitonen mit akustischen und optischen Phononen in einem einzelnen InGaAs QP im Detail analysiert. Durch Vergleich mit theoretischen Modellen wird ein Verständnis für die Linienform und die entscheidenden Phononenmoden erzielt.

Die Feinstrukturauspaltung (FSA) ist bedeutend für die Erzeugung von verschränkten Photonenpaaren. Ein neuer Ansatz die FSA zu reduzieren wird untersucht. Die ersten spektroskopischen Untersuchungen an einzelnen QP gewachsen auf (111) GaAs werden gezeigt und eine deutliche Verringerung der FSA präsentiert.

PUBLICATION

Parts of this work have been published in the following articles

1. *"Acoustic and Optical Phonon Scattering in a Single In(Ga)As Quantum Dot,"*
   E. Stock, M.-R. Dachner, T. Warming, A. Schliwa, D. V, M. Richter, V.A. Haisler, A. Knorr, and D. Bimberg
   Physical Review B rapid, vol. 83, p. 041304 (2011)

2. *"High Speed Single Photon Source Based on Self-Organized Quantum Dots"*
   E. Stock, W. Unrau, A. Lochmann, J. A. Töfflinger, M. Öztürk, A. I. Toropov, A. K. Bakarov, V. A. Haisler and D. Bimberg
   Semicond. Sci. Technol. vol. 26 p 014003 (2011)

3. *"Spatial Imaging of Resonant Electrical Injection of Carriers into Individual Quantum Dots,"*
   A. Baumgartner, E. Stock, A. Patane, L. Eaves, and D. Bimberg
   Physical Review Letters, vol. 105, p. 257401 (2010)

4. *"Single-Photon Emission from InGaAs Quantum Dots Grown on (111) GaAs,"*
   E. Stock, T. Warming, I. Ostapenko, S. Rodt, A. Schliwa, J.A. Tofflinger, A. Lochmann, A.I. Toropov, S.A. Moshchenko, D.V. Dmitriev, V.A. Haisler, and D. Bimberg,
   Applied Physics Letters, vol. 96, p. 93112 (2010)

5. *"In(Ga)As Quantum Dots Grown on GaAs(111) Substrates for Entangled Photons Pairs"*
   I. Ostapenko, E. Stock, T. Warming, S. Rodt, A. Schliwa, M. Öztürk, J. A. Töfflinger, A. Lochmann, D. Bimberg, A.I. Toropov, S.A. Moshchenko, D.V. Dmitriev, and V. A. Haisler,
   Journal of Physics: Conference Series vol. 245, 012003 (2010).

6. *"Phonon Interaction on a Single Quantum Dot Emission Line"*
   E. Stock, A. Baumgartner, M.-R. Dachner, T. Warming, A. Schliwa, and A. Patanè, L. Eaves, M. Richter, A. Knorr, M. Henini, and D. Bimberg,"
   OSA Technical Digest (CD) IWD7, CLEO, Baltimore, USA, (2009)

7. *"(111)-Grown In(Ga)As/GaAs Quantum dots as Ideal Source of Entangled Photon Pairs,"*
   A. Schliwa, M. Winkelnkemper, A. Lochmann, E. Stock, and D. Bimberg,
   Physical Review B, vol. 80, p. 161307 (2009)

8. *"Electrically Pumped, Micro-Cavity Based Single Photon Source Driven at 1 GHz,"*
   A. Lochmann, E. Stock, J.A. Tofflinger, W. Unrau, A. Toropov, A.

Bakarov, V.A. Haisler, and D. Bimberg
Electronic Letters, vol. 45, pp. 566, (2009)

9. *"Hole-hole and Electron-hole Exchange Interactions in Single InAs/GaAs Quantum Dots,"*
T. Warming, E. Siebert, A. Schliwa, E. Stock, R. Zimmermann, and D. Bimberg
Physical Review B, vol. 79, p. 125316 (2009)

10. *"Quantum Dots for Single- and Entangled-Photon Emitters,"*
D. Bimberg, E. Stock, A. Lochmann, A. Schliwa, J. A. Tofflinger, W. Unrau, M. Munnix, S. Rodt, V.A. Haisler, A.I. Toropov, A. Bakarov, and A.K. Kalagin,
IEEE Photonics Journal, vol. 1, p. 58 (2009)

11. *"Cavity-Enhanced Emission in Electrically Driven Quantum Dot Single-Photon-Emitters,"*
A. Lochmann, E. Stock, M.C. Munnix, J.A. Tofflinger, W. Unrau, D. Bimberg, A. Toropov, A. Bakarov, and V. Haisler,
SPIE Photonic Materials, Devices, and Applications III, Dresden, Germany vol. 7366, p. 736604, (2009)

12. *"Non-classical Light Emission from a Single Electrically Driven Quantum Dot,"*
M. Scholz, S. Buttner, O. Benson, A.I. Toropov, A.K. Bakarov, A.K. Kalagin, A. Lochmann, E. Stock, O. Schulz, F. Hopfer, V.A. Haisler, and D. Bimberg
Optics Express, vol. 15, p. 9107, (2007)

13. *"Electrically Driven Quantum Dot Single Photon Source,"*
A. Lochmann, E. Stock, O. Schulz, F. Hopfer, D. Bimberg, V.A. Haisler, A.I. Toropov, A.K. Bakarov, M. Scholz, S. Büttner, and O. Benson
Physica status solidi (c), vol. 4, p. 547, (2007)

14. *"Electrically Driven Single Quantum Dot Polarised Single Photon Emitter,"*
A. Lochmann, E. Stock, O. Schulz, F. Hopfer, D. Bimberg, V.A. Haisler, A.I. Toropov, A.K. Bakarov, and A.K. Kalagin,
Electronic Letters, vol. 42, p. 774, (2006)

15. *"Electrically Pumped InAs Single Quantum Dot Emitter,"*
A. Lochmann, E. Stock, O. Schulz, F. Hopfer, D. Bimberg, V.A. Haisler, A.I. Toropov, A.K. Bakarov, A.K. Kalagin, M. Scholz, S. Buttner, and O. Benson
Proc. SPIE Workshop on Optical Components for Broadband Communication, vol. 6350, p. 63500F , (2006)

PATENT:

1. *"Single Photon Source"*
   A. Schliwa, E. Stock, D. Bimberg
   German patent application, pending

FURTHER PUBLICATIONS:

1. "Comparison between two types of photonic-crystal cavities for single-photon emitters"
   W. Fan, Z. Hao, E. Stock, J. Kang, Y. Luo and D. Bimberg.
   Semicond. Sci. Technol. vol. 26 p 014014 (2011)

2. *"Spectroscopic Access to Sngle-hole Energies in InAs/GaAs Quantum Dots,"*
   E. Siebert, T. Warming, A. Schliwa, E. Stock, M. Winkelnkemper, S. Rodt, and D. Bimberg
   Physical Review B, vol. 79, p. 205321, (2009)

3. *"Effect of Excitation Level on the Optical Properties of GaAs/AlGaO Microdisks with an Active Region Containing InAs Quantum Dots,"*
   A.M. Nadtochiy, S.A. Blokhin, A.V. Sakharov, M.M. Kulagina, Y.M. Zadiranov, N.Y. Gordeev, M.V. Maksimov, V.M. Ustinov, N.N. Ledentsov, E. Stock, T. Warming, and D. Bimberg,
   Semiconductors, vol. 42, p. 1228, (2008)

4. *"Novel Concepts for Ultrahigh-speed Quantum-dot VCSELs and Edge-emitters "*
   N.N. Ledentsov, F. Hopfer, A. Mutig, V.A. Shchukin, A.V. Savelev, G. Fiol, M. Kuntz, V.A. Haisler, T. Warming, E. Stock, S.S. Mikhrin, A.R. Kovsh, C. Bornholdt, A. Lenz, H. Eisele, M. Dahne, N.D. Zakharov, P. Werner, and D. Bimberg,
   Proc. of SPIE: Physics and simulation of optoelectronic devices XV, vol. 6468 p. 64681O, (2007)

5. *"Submonolayer Quantum Dots for High Speed Surface Emitting Lasers,"*
   N.N. Ledentsov, D. Bimberg, F. Hopfer, A. Mutig, V.A. Shchukin, A.V. Savelev, G. Fiol, E. Stock, H. Eisele, M. Dähne, D. Gerthsen, U. Fischer, D. Litvinov, A. Rosenauer, S.S. Mikhrin, A.R. Kovsh, N.D. Zakharov, and P. Werner,
   Nanoscale Research Letters, vol. 2, p. 417-429, (2007)

6. *"20 Gb/s 85 Degrees C Error-free Operation of VCSELs Based on Submonolayer Deposition of Quantum Dots,"*
   F. Hopfer, A. Mutig, G. Fiol, M. Kuntz, V.A. Shchukin, V.A. Haisler, T. Warming, E. Stock, S.S. Mikhrin, I.L. Krestnikov, D.A. Livshits, A.R. Kovsh, C. Bornholdt, A. Lenz, H. Eisele, M. Dähne, N.N. Ledentsov, and D. Bimberg,
   IEEE Journal of Selected Topics in Quantum Electronics, vol. 13, p. 1302, (2007)

7. *"Room-temperature 1.3-μm Lasing in a Microdisk with Quantum Dots,"*
N.V. Kryzhanovskaya, S.A. Blokhin, A.G. Gladyshev, N.A. Maleev, A.G. Kuzmenkov, E.A. Arakcheeva, E.M. Tanklevskaya, A.E. Zhukov, A.P. Vasilev, E.S. Semenova, M.V. Maximov, N.N. Ledentsov, V.M. Ustinov, E. Stock, and D. Bimberg,
Semiconductors, vol. 40, p. 1101, (2006)

8. *"The Impact of Thermal Effects on Emission Characteristics of Asymmetrical AlGAO-waveguide Microdisks Based on Quantum Dots,"*
S.A. Blokhin, A.V. Sakharov, A.M. Nadtochy, M.M. Kulagina, Y.M. Zadiranov, N.Y. Gordeev, M.V. Maximov, V.M. Ustinov, N.N. Ledentsov, E. Stock, T. Warming, and D. Bimberg,
Applied Physics Letters, vol. 91, p. 121103, (2007)

9. *"Direct Observation of Tunneling Emission to Determine Localization Energies in Self-organized In(Ga)As Quantum Dots,"*
M. Geller, E. Stock, R. Sellin, and D. Bimberg,
Physica E, vol. 32, p. 171, (2006)

10. *"Optical Studies of Asymmetric-waveguide Submonolayer InGaAs QD Microdisks Formed by Selective Oxidation,"*
S.A. Blokhin, N.V. Kryzhanovskaya, A.G. Gladyshev, N.A. Maleev, A.G. Kuzmenkov, E.M. Arakcheeva, E.M. Tanklevskaya, A.E. Zhukov, A.P. Vasilev, E.S. Semenova, M.V. Maximov, N.N. Ledentsov, V.M. Ustinov, E. Stock, and D. Bimberg
Semiconductors, vol. 40, p. 476, 2006

11. *"Hole Capture into Self-organized InGaAs Quantum Dots,"*
M. Geller, A. Marent, E. Stock, D. Bimberg, V.I. Zubkov, I.S. Shulgunova, and A.V. Solomonov
Applied Physics Letters, vol. 89, p. 232105 (2006)

12. *"Tunneling Emission from Self-organized In(Ga)As/GaAs Quantum Dots Observed via Time-resolved Capacitance Measurements,"*
M. Geller, E. Stock, C. Kapteyn, R.L. Sellin, and D. Bimberg,
Physical Review B, vol. 73, p. 205331 (2006)

13. *"Carrier Storage and Sonfinement in GaAs-based Self-organized Quantum Dots,"*
M. Geller, A. Marent, E. Stock, A.P. Vasiev, E.S. Semenova, A.E. Zhukov, V.M. Ustinov, and D. Bimberg, M. Stutzmann,
ed., Rust, Germany, p. 504. (2005)

14. *"Energy Selective Charging of type-II GaSb/GaAs Quantum Dots,"*
M. Geller, C. Kapteyn, E. Stock, L. Müller-Kirsch, R. Heitz, and D. Bimberg
Physica E, vol. 21, p. 474 , (2004)

CONTENTS

Part I

INTRODUCTION

1 INTRODUCTION

The present time is often called the information age. The modern service sectors become more and more virtualized and the information technology (IT) sector is one of the leading economic sectors in modern industrialized countries. Information becomes more and more valuable; in fact most part of the money is stored only as information. Hence the security of information is gaining more importance.

The race between code-breakers and cryptographers has already started in the ancient Egypt and will probably never end [Sino0]. Simple uncrackable cryptography exists if sender and receiver hold the same secret key, having the same length as the messages [Sha49]. These systems have one major disadvantage: The key must be exchanged in an absolutely secure way. Since 1978 modern cryptography systems can bypass this problem by using asymmetric cryptography [Riv78], which secrecy is based on the factorization of products of large prime numbers. Unfortunately modern computer systems are able to decode this system in rapidly decreasing times [Kle10].

Quantum key distribution opens the possibility to exchange a key secured by fundamental physical laws [Gis02] and hence to solve the main obstacle for simple absolute secret cryptography. The main idea is based on the quantum physical law, that a quantum bit (qubit) can neither be cloned [Woo82] nor measured without any perturbation. The secret key is encoded in qubits and an eavesdropper will add errors to the received key. Quantum key distribution is probably the first field were quantum physics with its counter-intuitive laws will be directly applied. Commercial systems for quantum key distribution are already sold by a few numbers of companies.

A crucial requirement for the implementation of such cryptography systems is the generation of single qubits. The polarization state of a single photon represents such a qubit and is used in the first quantum key distribution protocol, the well know BB84 protocol [Ben84]. Currently available commercial systems use attenuated laser pulses to approximate a single photon source. Due to the large number of empty pulses and possible photon number split attacks these systems have a reduced key exchange rate and security compared to systems with true single photon sources [Wak02]. To realize a long distance quantum cryptography network [Pee09] quantum repeater based on sources of entangled photon are required [Bri98, Dö99].

Self-organized semiconductor quantum dots (QDs) [Bim99] are capable of emitting single photons or pairs of entangled photons using well established semiconductor technology. The strong spatial confinement of electrons and holes on length scales smaller than the de-Broglie wavelength results in a unique electronic structure with discrete energy levels [Sti99]. Therefore QDs are often referred to as “artificial atoms in a dielectric cage”. In con-

trast to trapped atoms QDs are semiconductor based and novel compact optoelectronic devices can be realized [Bimo8].

1.1 STATE OF THE ART

The following sections give a short review on the state of the art in the specific fields investigated in this work. For a better classification the reviews are split into three sections according to the structure of the result part of the work at hand.

1.1.1 *Single photon sources*

The first evidence of anti-bunched light emission has been obtained 1977 by Kimble et al. in the fluorescence of single sodium atoms [Kim77]. In this experiment the atomic current was chosen to be low enough to ensure that only one atom can contribute to the fluorescence. This experiment triggered a series of studies on the non-classical light emission from single atoms. All these experiments suffer from the lack to trap a single atom for a time longer than a few microseconds [Die87, Die88]. It lasted till 1992 for the first observation of photon anti-bunching from a dye center in a solid system [Bas92].

Most quantum optic experiments used parametric down conversion of a laser pulse in a $\chi^{(2)}$nonlinearity. This generates time-bin [Bre99] or polarization entangled photon [Ou88] pairs. Unfortunately, the conversion efficiency of parametric down conversion is very low and increasing the laser power results in an enhanced probability to generate four photons [Sca04]. Consequently this system is not a true single photon source.

In 2000 the first stable solid-state source of single photons based on vacancy centers in diamond has been demonstrated [Kuroo]. This is a three-level system and therefore the second-order correlation function $g^{(2)}$exhibits also bunching. Furthermore the long decay time of a few tens of nanoseconds reduces the maximum repetition rate. An excellent overview of different single photon sources is given in [Lou05]

The application of quantum dots as single photon sources has been proposed 1999 by Kim et al. [Kim99] and was demonstrated one year later in colloidal [Micooa] and self-organized quantum dots [Micoob]. The first electrically pumped single photon source based on semiconductor QDs has been realized in 2002 by Yuan et al. [Yua02]. In this device a large number of QDs were pumped and a shadow mask was used to select the luminescence from a single QD.

Electrical pumping of single QDs poses two main challenges: The first is the control of the current path in a way that only one QD is pumped, and the second is to assure that the QD is equally filled by electrons and holes to achieve uncharged excitonic emission. The latter is of interest for the generation of entangled photons: The uncharged biexciton-exciton decay cascade leads to the creation of entangled photon pairs (provided the fine-structure splitting FSS is small enough) [Benoo].

The out-coupling efficiency of QD based single photon sources can be enhanced by resonant coupling to a micro-cavity [Pel02]. In fact, the first demonstration by Michler et al. [Mic00b] already used a microdisk in the experiment. A second advantage of micro-cavity based devices is the higher possible repetition rate. The exciton life time is reduced by the Purcell-effect [Pur46] and, consequently, the time jitter of photon emission can be reduced to less than 100 ps [Ben05b]. This allows repetition rates up to 1 GHz [Loc09]. A very high quality factor [Lö5] of the micro-cavity is not desired since the device should not work in the strong coupling regime [Rei04].

Today the study of single photon emission from quantum dot is a very intense field. ISI Web of knowledge finds for the query "Topic=(Single photon) and Topic=(quantum dot)" 118 and 126 entries for the year 2009 and 2010 respectively. A good overview about semiconductor quantum dot based single photon sources can be found in [Shi07, Mic10].

1.1.2 *Phonon coupling*

In contrast to single photon emitters based on atomic systems [Kim77], the coupling of a QD to its semiconductor matrix drastically influences the properties of the photons. In particular, the excitonic recombination process is accompanied by a lattice distortion and the generation of polarons [Kru02, Fö3]. This scattering process between the exciton and phonons leads to a dephasing which results in a reduction of the coherence length of the photons. However, most quantum optic experiments (like on indistinguishable photons or quantum cryptography systems using double Mach-Zehnder interferometers [Gis02]) require long coherence length. Also theory predicts, that exciton-phonon scattering may be the limiting factor for generation of entangled photon pairs [Hoh07, Car10].

On the other hand, luminescence broadening by phonon scattering is useful in experiments with respect to the strong light-matter coupling: The phonon assisted luminescence can be amplified by the cavity and the cavity luminescence can be observed even in micro-pillars containing only a single QD [Rei04]. Hence, to study the strong light-matter coupling theoretically [Lau08, Tar10] a complete luminescence spectrum including phonon scattering must be used [Ulh10].

Phonon scattering has been mostly studied until now on polar CdSe QDs, where the phonon coupling is much stronger than e.g. in the non polar InGaAs QD system. The latter one, however, was most successful for device applications in the last decade, such as the generation of electrically driven single photons and entangled photon pairs [Bim09, Shi07]. Photoluminescence measurements on ensembles of InGaAs QDs lead to the conclusion, that coupling to optical phonons might be enhanced in QDs as compared to bulk material [Hei99b].

However, the line shape of single longitudinal optical (LO) phonon replica have never been studied experimentally. In this respect electrically pumped single QDs allow to study the exciton-phonon interaction on the fundamental

level: A single electron-hole pair recombines under generation of a single photon and a phonon.

A number of theoretical approaches exist to describe at least in parts the exciton/electron-LO phonon interaction. One of them suggests the importance of a second-order elastic interaction between QD charge carriers and LO phonons [Usko0]. The resulting Gaussian shape of the LO replica was, however, found to be an artifact [Mulo6, Usko6]. Another strong coupling model suggested a coupling of LO phonons to excited electronic states in the QD or the wetting layer [Mulo7], leading to a more triangular shape of the LO phonon replica. Only recently, an exact solution of the electron-phonon interaction in the quantum optical regime was presented [Car10]. None of the models has been compared to experimental data on single QDs so far.

1.1.3 *QDs with reduced fine-structure splitting*

As proposed by Benson et al. [Beno0] a single QD is an excellent source for entangled photon pairs if the fine-structure splitting (FSS) of the exciton bright states is reduced to less than the homogeneous line width.

For In(Ga)As QDs on (001) GaAs the FSS is non-zero, even for perfect symmetric QDs, due to the asymmetric piezoelectric field. In experiment values from -80 µeV up to 520 µeV [Bayo2, Hö4, Lano4, Kowo5, Sego5] have been observed. Consequently, in the first experimental demonstration of entangled photons from QDs post growth manipulation such as spectral filtering [Ako06] and magnetic fields [Steo6] were used. Other attempts to reduce the FSS include thermal annealing [Youo5, Sego6], additional stress [Seio6] or electric fields [Hö4, Kowo5]. These techniques are complex and have to be adjusted for every single QD. Only if by accident the asymmetric field becomes very small or is compensated by the QD elongation, the FSS will be small enough for the generation of entangled photons [Sego5, Hafo7].

In contrast to QDs on (001) GaAs, the piezoelectric field for QDs grown on (111) GaAs substrate is directed along the growth direction [Povo4] and cannot lower the symmetry below C_{3v}. Using 8 band k·p theory in conjunction with the configuration interaction method it has been proposed recently that in this case the FSS is expected to be zero [Scho9, Sino9, Bimo9]. Therefore triangular shaped InAs QDs grown on (111) GaAs surface might be intrinsic sources for entangled photon pairs [Scho8].

On (111) GaAs the surface energies are different from that on (001) surfaces, which makes the growth of self-organized QDs very challenging. In previous attempts to grow InAs QDs on (111) GaAs substrates tetrahedral shaped recesses were used [Sug95]. This leads to the formation of rather large dots with a homogeneous line width of a few meV and it remained open whether such QDs are suitable for single or entangled photon pair emission. Another attempt to grow QDs on (111) substrates [Tsa98] resulted in a high density of very small QDs with a small activation energy, which are electronically close to quantum wells. Up to now no sharp and intense luminescence lines from self-organized QD grown on (111) GaAs have been reported.

1.2 THE AIM OF THIS WORK

In the work at hand semiconductor self-organized quantum dots are investigated for their application as sources of single and entangled photons. The achieved results demonstrate milestones in the development of highly efficient single photon sources and give insight into fundamental properties of QDs, such as phonon scattering and the excitonic fine-structure splitting.

This work is organized in seven chapters in the following way:

After the introduction in the first chapter the second chapter briefly describes the fundamental background required for the understanding of the results presented in this work.

Chapter 3 reports on the experimental techniques used in this work. Beside the description of the custom-built setup special intention is given to single photon measurement techniques. Superconducting detectors representing a new type of single photon detectors will be analyzed and compared to typically used avalanche photo diodes (APDs). A complete analysis of photon correlation measurements is presented, including possible errors and how to account for them.

The main results on single photon devices are presented in chapter 4. Three types of devices with increasing complexity are discussed: The "poor man's single photon source" consisting of a simple pin diode without any current constriction shows single QD emission by concurrent resonant tunnel injection of electron and holes. The second type of devices demonstrates the first highly efficient electrical pumping of a single QD with a record pure spectrum and clear antibunching of the emitted photons. Finally the resonant cavity light emitting diode (RCLED) uses resonant coupling to a microcavity to enhance the out-coupling efficiency. Due to the Purcell effect this device can be driven with up to 1 GHz, the highest reported repetition rate of a single photon source. The optical response of this device is too fast for APDs, hence superconducting detectors were used. The purity of the spectrum and the high out-coupling efficiency of the RCLED enable single photon emission for temperatures up to 80 K.

Chapter 5 presents the first observation of acoustic and optical phonon scattering in a single electrical driven QD. By comparing the experimental data with calculated spectra the influence of the wave function shape on the phonon scattering is analyzed. For a correct description wave function calculated by 8-band-k·p theory and the phonon life time were to be used.

In chapter 6 a new proposal for the generation of entangled photon is studied. The first spectroscopic measurements on single QDs grown on (111) GaAs are presented. By a systematic analysis of the spectra a "fingerprint" of luminescence lines is identified. The measured fine-structure splitting is lower than for (001) grown QDs, making this a promising approach for the generation of entangled photons.

The work is concluded by a summary and an outlook in chapter 7.

Part II

FUNDAMENTALS AND EXPERIMENTAL TECHNIQUES

2

THEORETICAL BACKGROUND AND FUNDAMENTAL CONCEPTS

This chapter describes the main theoretical concepts, necessary to understand the experimental results presented in this work. In the first part the principle of quantum key distribution is described. Its possibility to exchange message securely motivates the development of single photon and entangled photon pair sources. In section 2.2 the photon characteristic of different sources are discussed. The third part describes self-organized semiconductor quantum dots. Special attention is given to their electronic structure, mainly the exciton fine-structure splitting, which is of importance for the generation of entangled photons. Finally, in section 2.5 the main properties of microcavities are described and how they are helpful for single photon emitters.

2.1 QUANTUM KEY DISTRIBUTION

Quantum key distribution is often incorrectly referred to as *Quantum Cryptography*, as it is the best established example of the group of quantum cryptography tasks. It is probably the first application, where counter-intuitive laws of quantum mechanics are directly used and it will be briefly described in this section. An excellent overview of different protocols and techniques is given by Gisin et al. [Gis02] and Scarani et al [Sca09].

The idea of quantum key distribution (QKD) is to exchange a key by the sender Alice and the receiver Bob, where the security is based on fundamental quantum mechanical laws. Afterward this key can be used to encode a message using classical cryptography techniques. If the key length is equal the message length, the encoding can be done by a simple XOR (eXclusive OR) operation and will be absolutely secure [Sha49]. QKD is secure in terms of an eavesdropper will be detected by sure, but not in terms of being non-destroyable.

QKD based cryptography uses two channels: The public channel to exchange information, which are useless for an eavesdropper Eve and to transmit the encoded message. This channel can be for example the internet, since it requires no security. The second channel is the so called quantum channel, since quantum bits (qubits) are transmitted on it. Up to day this channel has to be a point-to-point connection between Alice and Bob. The development of quantum cryptography networks is still under progress.

In the following the best known protocol, the BB84, will be described. Bennett and Brasard introduced this protocol in 1984 [Ben84] based on an idea of Wiesner published the year before [Wie83]. The BB84 is often utilized using polarized photons but in fact it can be used with any pairs of conjugated states. A qubit can be any quantum mechanical state which can be described by the superposition of two orthogonal states. Unlike a classical

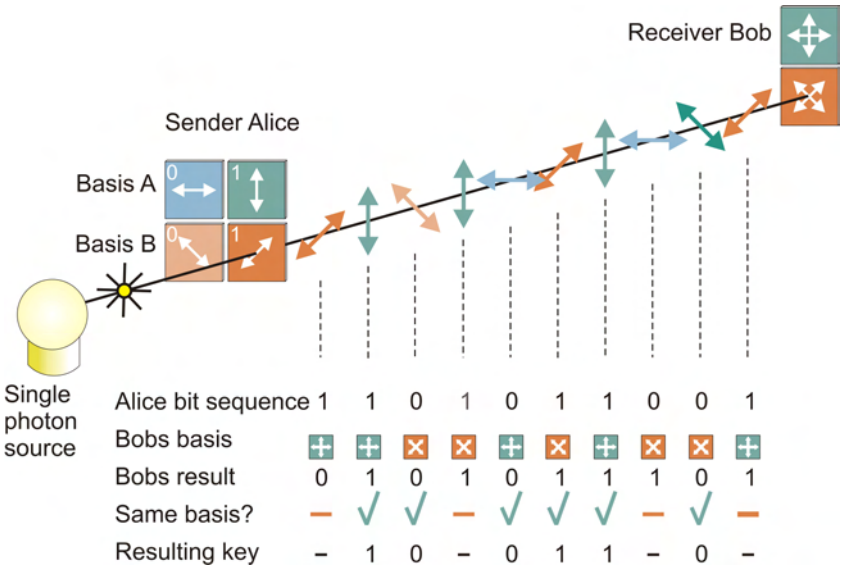

Figure 2.1: Working principle of the BB84 protocol. Alice uses two conjugated basis to encode a random sequence of bits. Only bits where Alice and Bob used the same basis are taken as the key.

bit a qubit should not be either 1 or 0, but can also be a superposition of both. For a better understanding polarized photons will be used in the following.

The main idea is to use two complete quantum mechanical bases A and B, which are conjugated. Consequently, one basis vector in basis A can be described as the superposition of the two basis vector in B. For polarized photons this basis can be two of the rectilinear ↕↔, diagonal ⤢⤡ or circular basis. Taking the first two of them it is given:

$$\nearrow = \frac{1}{\sqrt{2}}(\updownarrow + \leftrightarrow) \,.$$

Figure 2.1 shows the working principle of the BB84 for polarized photons. Alice encodes a series of random bits in the polarization state of randomly chosen basis A or B. Bob measures the incoming photons also in a randomly chosen basis (second line in figure 2.1). If Bob measures not in the same basis as used by Alice his result will coincide only in 50 % with the bit, sent by Alice. Upon completing the measurement by Bob, Alice tells him in which basis the bit was encoded. This can be done via the public channel, since no information about the bits of the key is given. Only those bits are taken as key, for which Alice and Bob used the same basis.

Parts of this key are then compared on the public channel to measure the quantum bit error rate (QBER). The QBER is defined as the ratio of wrong bits to correct bits. As will be described in the following section an eavesdropper must increase the QBER significantly. If the QBER is too high, Alice and Bob decide to abort the protocol. Otherwise, they apply *error correcting* and *privacy amplification* tools (called post processing) to distill a secret key [Ren05].

Eavesdropping

The fact that Alice chooses her basis randomly and informs Bob only after he measured the photon, is the key for uncovering an eavesdropper. Eve can measure the photons only in a randomly chosen basis. To cover her presence she sends a photon to Bob, which has the same polarization she has measured. If Eve uses a different basis than Alice (which happens in 50%) the photon which will be a pure state in a different basis than used by Alice. If now Bob measures in the same basis as Alice (which is the "wrong" one for this photon), he will only by with a probability of 50 % measure the same bit as was send by Alice. Consequently an eavesdropper will add an error of 25 %, which can be easily detected by comparing parts of the key. For a perfect system without any perturbation or losses, the probability to detect Eve is given by:

$$P = 1 - \left(\frac{3}{4}\right)^n, \tag{2.1}$$

where n is the number of bits compared by Alice and Bob. For example, by comparing only 30 bits Eve will be detected to 99.98 %.

A realistic system will have some intrinsic perturbation and losses, resulting in a non-zero QBER. In principle Eve might replace the real noisy quantum channel with an ideal noise-free channel, thus adding only the same amount of noise as the original channel. Depending on the used post processing technique a QBER of up to 12 % is accepted to ensure secure communication by the BB84 protocol [Ren05, Sca08].

The second possible technique to attack a QKD system may be to copy the photons send by Alice and to measure only the copy. Thus, the QBER at Bob will not be increased. The exact copy of quantum state however is forbidden by the no-cloning theorem [Woo82]; hence this attack is not possible.

Commercially available QKD-systems use attenuated laser pulses, having a small probability of two photons per pulse (see equation 2.3). This allows applying a *Photon Number Splitting* (PNS) attack: Eve separates only one photon and measures it, while the second arrives at Bob without any perturbation. This attack is impossible for *true* single photon sources. The other disadvantage of attenuated laser pulses is the large fraction of empty pulses, which are usually at least 90 %. A dark count at Bob's detector during an empty pulse will increase the QBER. The number of pulses containing multiple photons should not exceed the number of dark counts at Bob's detector. Consequently, systems using attenuated lasers have a significantly less transmission rate and distance in comparison to systems using true single photon sources [Wak02, Gob04].

Entangled Photon Pairs

The second well known QKD protocol is the Ekert protocol [Eke91]. This protocol uses all three bases of a polarized photon mentioned above. One photon is measured at Alice, thus preparing the polarization of the other

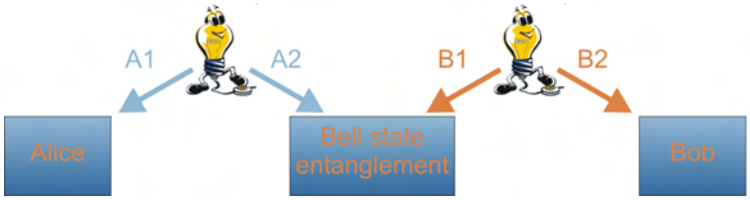

Figure 2.2: Long-distance quantum key distribution with entangled photon sources. By a Bell state entanglement in the middle the two photons A1 and B1 become entangled.

photon at Bob. Although this protocol is similar to the BB84 the entangled photons allow to test the violation of Bells inequality and Eve can be detected easier.

A source of entangled photon pairs may allow building up a long-distance quantum key distribution network [Bri98, Dö99]. The idea is depicted in figure 2.2. The photons of two source of entangled photon pairs A2 and B2 are getting entangled by a Bell state measurement in the middle. Thus the photons A1 and B2 become entangled and can be used in QKD for example using the Ekert protocol . Up to day the entanglement of three out of the four Bell states of A2 and B1 has been demonstrated yet [Hou06].

2.2 PHOTON STATISTIC

Since its introduction by Glauber in 1963 [Gla63] the photon statistic on a fixed position for a stationary field is described by the second order correlation function:

$$g^{(2)}(t) = \frac{\langle I(0)\rangle \langle I(t)\rangle}{\langle I(0)\rangle^2}, \tag{2.1}$$

where $I(t)$ is the intensity of a light field at a time t and $\langle\rangle$ represents the integration over time. The intensity is proportional to the square of the electric field, thus the name second order correlation function.

The first order correlation function describes the distribution of the electric field and can be measured using a Michelson-Interferometer. It is of interest for the coherence length, but will not discussed in this work.

The second order correlation $g^{(2)}$-function can be measured with a Hanbury-Brown Twiss interferometer. This technique will be described in details in section 3.3 on page 44.

In the second quantization the $g^{(2)}$-function can be described as:

$$g^{(2)}(t) = \frac{\langle a^\dagger(0)a^\dagger(t)a(0)a(t)\rangle}{\langle a^\dagger(0)a(0)\rangle \langle a^\dagger(t)a(t)\rangle}, \tag{2.2}$$

with the photon creation and annihilation operators $a^\dagger$ and a. The second order correlation function can be interpreted as the probability to detect a photon at time t after the detection of a photon at $t = 0$. Depending on

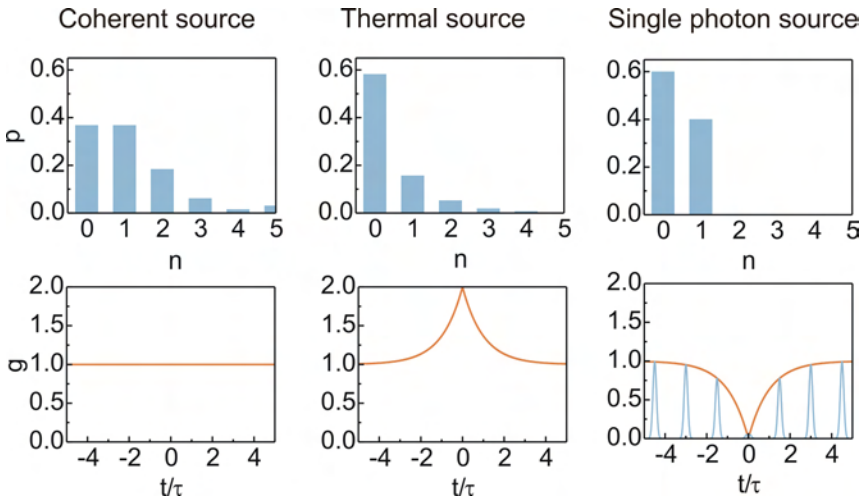

Figure 2.3: Top: photon distribution for three types of light source. The mean number for Poisson and Boltzmann distribution (left and center) was chosen to μ=1. Bottom: Corresponding second order correlation function. The time axes are given in units of the coherence time.

the photon distribution three types of light sources are characteristic. The corresponding photon distribution and second order correlation function are shown in figure 2.3. The photon distribution is an intrinsic property of a light source and cannot be altered by changing the intensity. Attenuation leads to a reduced number of photons for a given time but has no influence on the distribution.

The best representation of a classical field are coherent states, which are per definition eigenstates of the photon annihilation operator. It can be shown, that the photon distribution of a coherent state is given by a Poisson distribution:

$$P(n,\mu) = \frac{e^{-\mu}\mu^n}{n!}, \tag{2.3}$$

where n is the number of photons and μ is the mean photon number.

For a Poisson distribution the variance is equal the mean number, thus for a coherent source the $g^{(2)}$value is constant 1 (see figure 2.3 left).

The best coherent light sources are lasers and the probability of finding n photons in a short laser pulse is given by equation 2.3. QKD often uses laser pulses with a mean number of $\mu = 0.1$ photons per pulses. Thus the probability to have more than one photon per pulse is still 0.5 %.

The second type of light source has a super-Poissonian photon distribution, meaning the variance is larger than the mean. A typical example is a thermal light source, for which the photons follow a Boltzmann distribution (figure 2.3 center). Photons from such sources tend to *bunch* together, which means that the probability to detect a second photon soon after the first is increased. For thermal light sources the coherence time is usually shorter than the time resolution of single photon detectors, hence it is not possible to observe the bunching.

The third type of light sources has a sub-Poissonian distribution. For these sources the photons are well separated, they are *anti-bunched*. Such light sources are often referred to as non-classical light sources. A typical example is any two level systems: After the relaxation into the lower state, by emitting a photon, the system has to be excited again, before it can emit a second photon. Thus the photons are separated by the excitation plus relaxation time.

As will be shown in the following QDs, represents such a two level system and thus are ideal candidates for single photon sources.

2.3 QUANTUM DOTS

If the carrier motion in a semiconductor material is limited by a potential to the range of their *de-Broglie* wavelength, their density of states (DOS) changes dramatically in comparison to bulk material. Depending on in how many directions the carrier propagation is limited to the *de-Broglie* wavelength these structures are referred as:

Quantum wells with a constriction in one dimension. In these structures the charge carriers are free to propagate in a plane and the density of states is a continuous step function.

Quantum wires limit the mean free path of the charge carriers in two dimensions by a wire of material with smaller band gap. The density of states is still continuous with some saltus.

Quantum dots confine the charge carrier in all three dimensions and have a delta function like density of states.

The confinement is usually achieved by an electrical potential or by embedding a semiconductor material with a band gap E_{gQD}in another material with a larger band gap E_{gbulk}. The second case is schematically illustrated for a quantum dot in the left panel of figure 2.4. The QD material has a smaller band gap than the surrounding bulk material, resulting in an attractive potential for electrons and holes. Due to the strong confinement of the electron- and hole wavefunctions only discrete energies are allowed in the QD, labeled as e_0/h_0 and e_1/h_1 for the electron/hole ground and first excited states. As depicted in the diagram both electrons and holes are confined in this type I QD. In a type II QD only one type of charge carriers is confined, whereas the electrons have a repulsive potential. These kinds of quantum dots are an ideal candidate for novel memory systems [Mar07].

2.3.1 *Structural Properties*

Modern epitaxy techniques such as molecular beam epitaxy (MBE) [Her96] or metal organic chemical vapor phase deposition (MOCVD) [Str99] allow the production of semiconductor materials with monolayer accuracy. Under ideal conditions on top of one semiconductor material a second semiconductor with different lattice constant will grow pseudomorphically. Above

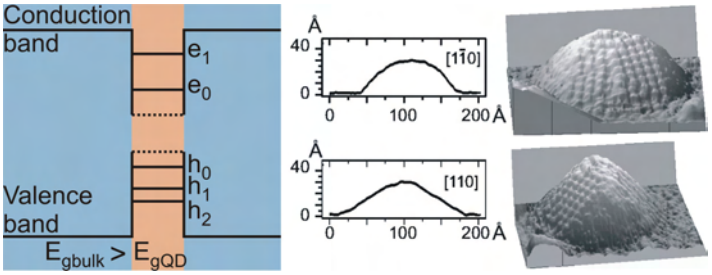

Figure 2.4: Left: Band diagram for a QD in one dimension. e_0/h_0 and e_1/h_1 are the electron/hole ground and first excited states. Right: Scanning tunneling microscope images of an InAs QD and the height profile along the [1$\bar{1}$0] and [111] direction, taken from [Mar01]

a critical layer thickness [Leo94] the induced strain can be reduced by the formation of islands with nanometer size on top of a wetting layer. The islands can be capped with the first material, having preferably a larger band gap E_{gbulk} than the island material E_{gQD}. This results in self-organized QDs grown in the so called Stranski-Krastanov mode. In this work GaAs (lattice constant a = 5.65 Å band gap E_{gbulk} = 1.42 eV at 300 K), was used as bulk material and InAs (lattice constant a = 6.05 Å, band gap E_{gbulk} = 0.35 eV at 300 K) as QD material. During the overgrowth material diffusion occurs resulting in InGaAs QDs in GaAs.

Depending on the growth conditions spatial QD densities between 10^9-10^{11}can be achieved. The QDs have a base length in the range of ten nanometers with a height of a few nanometers. The QDs usually have the shape of truncated pyramids with bases along the [1$\bar{1}$0] and [111] crystal axes.

The QD growth described above is self-organized; hence the position and size of the QDs are randomly distributed. By e-beam lithography of nano-holes [Ishoo], AFM induced oxidation [Sono5] or focused ion beam [Meh07] the substrate can be pre-patterned and the position of the QDs can be controlled. Due to the defects induced by the patterning these site-controlled QDs often exhibit weak and spectrally broad luminescence [Atk08, Alb10a].

2.3.2 *Electronic and Optical Properties*

The confinement of electron and hole wavefunctions in all directions leads to a quantization of the electronic states in the QDs. As depicted in figure 2.4 the electron ground state e_0 has a higher energy than the conductance band (dashed line) of the QD material and is well separated from the first excited state e_1.The same holds for the hole states. This is similar to the electronic structure of an atom, which is why QDs consisting of hundred thousands of atoms are often called “artificial atoms”.

In the simplest estimation the energy level structure of a QD can be compared to the standard harmonic oscillator of quantum mechanics. Since holes have a larger effective mass than electrons their level separation is

smaller than for electrons. For a complete description of the electronic structure 8-band-k·p [Sti99, Sch07] or pseudo-potential theory [Wan99] must be used.

The energy levels of the QDs are strongly influenced by their structural properties. The main interactions are:

- The QD **material** constitutes the band gap in the QD and thereby the energetic position of the lowest electron and hole levels.
- The QD **size** determines the confinement energy: The smaller the QDs are, the larger the confinement energy will be. As a consequence the energy difference of the electron and hole ground states will increase resulting in larger energies of the emitted photons.
- The QD **shape** influences the electron and hole wavefunction overlap. Due to the coulomb interaction the few particle energies change.
- The **strain** induced by the QD growth changes the band gap of the surrounding bulk and the QD material.
- The **symmetry** of the QD structure and the resulting potential determines the level degeneracy.

Charge carriers injected into the QD will relax to the lowest unfilled level in the quantum dot and can recombine under emission of a photon. Since self-organized QDs on one wafer differ at least in size and shape, the luminescence of an ensemble of QDs is inhomogeneously broadened to a few tens of micro electron volt. Sharp luminescence lines can be only observed in single QD spectroscopy with a spatial resolution of at least $1\,\mu m^2$.

The homogeneous line width of a single QD is given due to the Heisenberg uncertainty principle by the life time T_2 of the recombining complex. For excitons in InGaAs/GaAs QDs the homogeneous line width has been measured in the range of a few micro electron volts [Leooo] and is experimentally often limited by spectral diffusion [Töo].

Few particle complexes

Depending on the localization energy a QD can be filled with a number of electrons and holes. A single electron and hole pair is called an exciton (label: X), two/one electrons and one/two holes form a negatively/positively charged exciton or so called trion (X^-/X^+). The uncharged biexciton XX consists of two electrons and holes in the ground states. Further occupation of the first excited states of electrons and holes leads to higher complexes. Figure 2.4(a) shows the corresponding charge carrier fillings of the QD.

Due to the strong confinement in the QD the charge carriers cannot be described as separate single particles instead they form the above men-

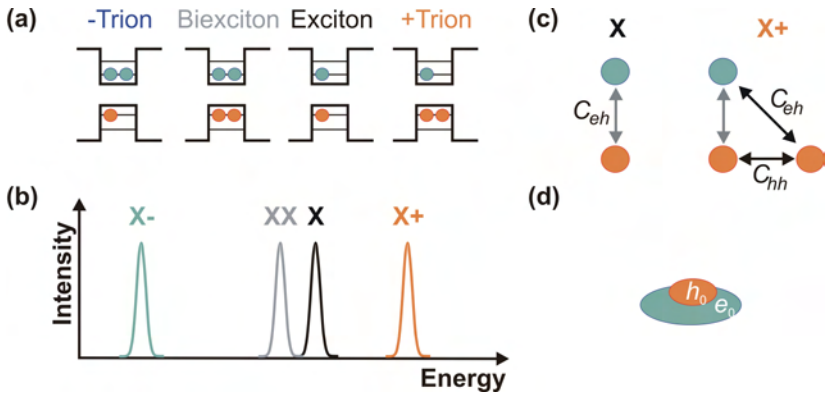

Figure 2.5: Schematic diagram of the different complexes in a QD: (a) charge carriers and (b) energetic position of the uncharged exciton and biexciton as well as the trions (c) coulomb interaction and (d) wavefunction distribution of the electrons and holes

tioned *quasiparticles*. These quasiparticles can be described by the following Hamiltonian H:

$$H = H_e + H_h + H_{coul} \tag{2.1}$$

where H_e and H_h are the electron and hole single particle Hamiltonians. The Hamiltonian of the Coulomb interaction H_{coul} leads to a change of the quasiparticle energy with respect to single particles. For two charge carriers i, j the mean field Coulomb interaction is given by:

$$C_{coulomb} = \iint \frac{q_i q_j}{4\pi\epsilon_0\epsilon_r} \frac{|\psi_i(\mathbf{r}_i)|^2 |\psi_j(\mathbf{r}_j)|^2}{|\mathbf{r}_i - \mathbf{r}_j|} d\mathbf{r}_i d\mathbf{r}_j \,. \tag{2.2}$$

For an uncharged exciton the electron-hole Coulomb interaction C_{eh} (see figure 2.3.3 (c) is attractive. As a consequence the exciton energy is less than the sum of the energies of the single electron and hole. This exciton binding energy is calculated to be about a few tens of mili-electron volts [Sti99] and cannot be measured directly in QDs since states consisting of independent electron and hole particles do not exist. Since the confinement energy in QDs is much larger than the binding energy, complexes with an "anti-binding" energy can exist [Rod05].

In InAs and GaAs the holes have a larger effective mass than the electrons [Lan87], resulting in stronger localized wavefunctions (see figure 2.5 (d). This has a strong influence on the Coulomb interaction and hence the quasiparticle energy: In positive trions X^+ the two holes have a stronger wavefunction overlap than the electrons and holes. Consequently the additional repulsive hole-hole Coulomb interaction $C_{hh}$is larger than the attractive electron-hole Coulomb interaction C_{eh} and the energy of the X^+ is larger than of the uncharged X. The same arguments lead to a smaller energy of the X^- in comparison to the X.

A biexciton (XX) has one electron-hole pair more than the X; hence the additional C_{hh} and C_{ee} are both present. Whether the biexciton luminescence appears at larger or lower energy than the exciton cannot be described within this simple picture. In fact it mainly depends on the QD size and the magnitude of the correlation effects [Rod05].

Figure 2.5 (b) shows a schematic spectrum with the energetic position according to the above argumentation.

The coulomb interaction of the quasiparticles makes selforganized QDs ideal for single photon sources: The recombination energy of an exciton differs from that of a biexciton or other complexes. As a consequence at the wavelength of the exciton the QD can emit a second photon only after it is refilled in the same state. This is way QDs are referred to as *turnstile* single photon devices [Kim99, Mic00b, Sol02].

2.3.3 *Fine-Structure Splitting*

Beside the mean-field Coulomb interaction described above the quantum mechanical exchange interaction leads to a further splitting of the exciton states. This will be briefly discussed in the following. A more detailed description can be found in [Bay02, Seg08].

Due to the biaxial strain in InGaAs QDs the hole bands are well separated. As a consequence the holes in the QDs are mainly "heavy-holes" with a spin of $|\pm 3/2\rangle$ projected on the z-direction. The electrons have a spin of $|\pm 1/2\rangle$. Since both charge carriers are Fermions with a half integer spin, the solution of the Schrödinger equation has to be anti-symmetric. If two identical charge carriers a, b exchange their position the resulting situation should be identical. Hence, if $\psi_a^1 \otimes \psi_b^2$ is a solution so should be $-\psi_a^2 \otimes \psi_b^1$. This results in a so called exchange interaction term in the coulomb Hamiltonian in equation 2.1 in the form of:

$$\left\langle \psi_a^1 \psi_b^2 \right| H^{exchange} \left| \psi_a^2 \psi_b^1 \right\rangle . \tag{2.3}$$

The consideration of the spin states of electrons and holes leads to a splitting of the originally degenerate states. The main structure of the exchange Hamiltonian $H^{exchange}$ can be derived from group theory: The Hamiltonian should be invariant against all symmetry operations, for which the system does not change. For a C_{2v} symmetry the Hamiltonian can be split into three parts:

$$H^{exchange} = \underbrace{2\Delta_0 J_z S_z}_{H_0^{exchange}} + \underbrace{\Delta_1 (J_x S_x - J_y S_y)}_{H_1^{exchange}} + \underbrace{\Delta_2 (J_x S_x + J_y S_y)}_{H_2^{exchange}}, \tag{2.4}$$

where $\mathbf{J} = (J_x, J_y, J_z,)$ and $\mathbf{S} = (S_x, S_y, S_z,)$ indicate the total spin operators of the hole and electron. The terms $H_0^{exchange}$ and $H_2^{exchange}$ are invariant for any C_{4v} or D_{2d} operations and are called isotropic exchange interaction.

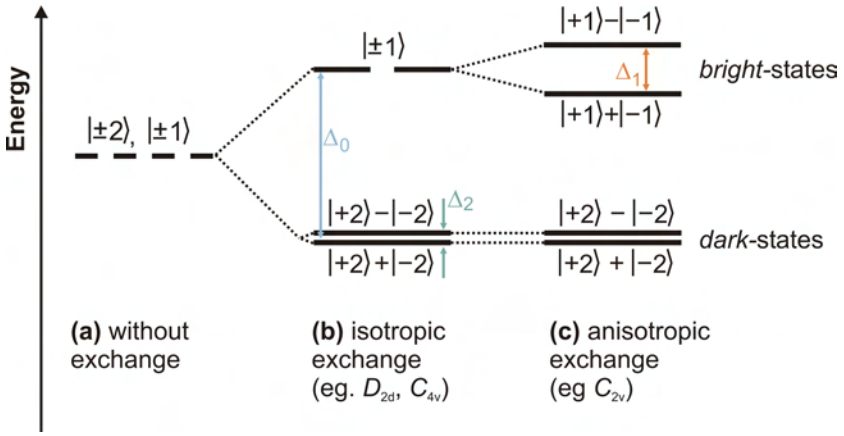

Figure 2.6: Schematic diagram of the splitting of the exciton state due to different exchange interaction terms

The third term $H_1^{exchange}$ leads to an additional splitting for systems with symmetry of less than C_{3v} and is called the anisotropic exchange. The parameters Δ_i in equation 2.4 are without physical meaning and simple describe the strength of the corresponding splitting.

An exciton consists of an electron with a spin of $|\pm 1/2\rangle$ and a hole with $|\pm 3/2\rangle$. The energy splitting of the exciton ground state with a total spin of $|\pm 2, \pm 1\rangle$ is schematically demonstrated in figure 2.6. The isotropic exchange Hamiltonian $H_0^{exchange}$ splits the fourfold degeneracy of the exciton ground state into two doublets with $|\pm 2\rangle$ and $|\pm 1\rangle$. Since photons have a spin of $|\pm 1\rangle$ only the upper doublet can couple to the photonic field and is called the *bright* state. The $|\pm 2\rangle$ state can only recombine non-radiatively or under two photon emission. Hence this state is not observable in luminescence experiments and called the *dark* state. A magnetic field leads to an intermixing of the $|\pm 2\rangle$ and $|\pm 1\rangle$ states and gives access to the dark states in luminescence experiments [Bayo2]. The splitting Δ_0 of the dark and bright states were derived from extrapolation to a zero magnetic field and estimated to a few hundreds of micro electron volts with a strong dependence on the QD size [Bayo2].

Electrons and holes are often injected into the QD without any spin control. Consequently the occupation probability of the bright and dark states is equal. The occupied dark state can only be emptied either by a further excitation into the biexciton state or by a spin flip into the exciton bright state, but will not contribute to the luminescence. Hence, the luminescence from the exciton is suppressed in comparison to a system with only bright states. This so called dark-state blocking is large important for InP/GaInP QDs [Reio8b].

As shown in figure 2.6 (c) the anisotropic $H_1^{exchange}$ term leads to splitting of the bright state for symmetry of less than C_{3v}. Δ_1 is called the fine-structure splitting (FSS) of the exciton and is of utmost importance for the generation of entangled photons from a QD.

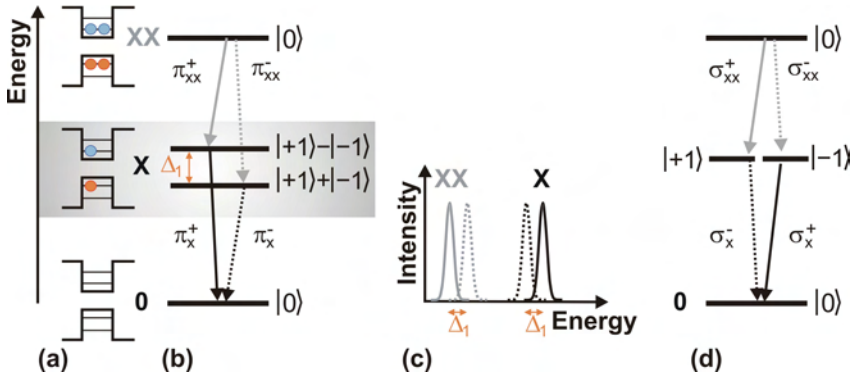

Figure 2.7: (a) Occupation of the QD and (b) electronic structure for the uncharged biexciton XX and exciton bright states X. (c) The FSS Δ_1 leads to a doublet splitting of the X and XX luminescence. (d) For a zero FSS the XX-X photons are entangled.

Generation of entangled photons

As proposed by Benson et al. in 2000 [Benoo] the biexciton-exciton recombination cascade from self-organized QDs can be used for the generation of entangled photon pairs. Figure 2.7 a) shows the QD occupation with electron and holes for the biexciton and exciton state. The biexciton consists of two electrons and two holes in the ground state. Due to the Pauli principle their spins must be oriented in opposite directions, resulting in a total spin of the biexciton of $|0\rangle$. According to equation 2.4 the biexciton exhibits no splitting due to the exchange interaction.

The biexciton decays into one of the split exciton bright states under emission of a single photon. Since the exciton states are a superposition of the $|+1\rangle$ and $|-1\rangle$ state, the emitted XX photon will be linearly polarized according to the anisotropy direction of the confining potential. As far as the bright states have different energies the polarization of the XX photon determines the photon energy. Hence, in luminescence experiments the XX recombination consists of a doublet with orthogonal polarized emission lines separated by the fine-structure splitting. A schematic spectrum of the XX-X cascade is shown in figure 2.7(c).

Depending on the polarization of the XX photon the QD is now well defined in one of the exciton bright states (see figure 2.7(b). If no spin flip occurs the X will recombine under emission of a photon having the same polarization as the XX photon and the energy of the X photon is predefined by the XX photon.

In the case described above the XX and X photons are regulated but not entangled. This changes drastically if the confining potential is has at least C_{3v} symmetry and the exchange splitting is zero. Now the exciton bright state is two-fold degenerate (see figure 2.6b) consisting of pure $|+1\rangle$ and $|-1\rangle$ states. As a consequence the XX photon is either $|\sigma^+_{xx}\rangle$ or $|\sigma^-_{xx}\rangle$ circular polarized and the polarization is *not* encoded in the energy. Since both polarizations have the same energy and transition probability the polarization of the XX photon is not defined.

Depending on which electron hole pair has recombined the QD is now without a clear definition in one of the bright states and can emit the X photon. Hence the polarization of the X photon is undefined but depends on the polarization of the XX photon. The XX-X photon cascade then represents maximally entangled Bell states [Benoo]:

$$\Psi = \frac{1}{\sqrt{2}} \left(\left| \sigma^{+}_{xx} \right\rangle \left| \sigma^{-}_{x} \right\rangle + \left| \sigma^{-}_{xx} \right\rangle \left| \sigma^{+}_{x} \right\rangle \right) \tag{2.5}$$

The generation of polarization entangled photons from a single self organized QD has been demonstrated in 2006 independently by the groups of D. Gershoni [Ako06] and A. Shields [Ste06]. The entanglement of the latter one has been discussed intense [Lin06, Gil07, Ste07]. Recently entangled photons from electrically pumped QDs have been demonstrated [Sal10].

Another mechanism for the generation of entangled photons has been proposed recently [Rei08a, Avr08]. In this approach the entanglement is achieved by color coincidence across generation rather than within generation. For this the $|\pi^{+}\rangle$ biexciton should have the same energy as the $|\pi^{-}\rangle$ exciton (see figure 2.7 (b). The which-path information for the two polarization states is than only encoded in the time ordering of the biexciton and exciton. By a polarization dependent time-reordering this which-path information can be eliminated, resulting in entangled photon pairs [Tro08]. For this approach the exciton and biexciton should have the same energy, which is simply a function of the QD size [Rod05, Sch07, Sch09]. This approach has not been demonstrated experimentally yet.

QDs grown on (001) vs. (111) GaAs

For a non-zero fine-structure splitting Δ_1 the two photon state of the XX-X cascade can be described by [Ste08]:

$$\Psi \propto \frac{1}{\sqrt{2}} \left(\left| \pi^{+}_{xx} \right\rangle \left| \pi^{+}_{x} \right\rangle + e^{i\Delta_1 \tau/\hbar} \left| \pi^{-}_{xx} \right\rangle \left| \pi^{-}_{x} \right\rangle \right), \tag{2.6}$$

where τ is the time delay between the biexciton and exciton. Hence, the FSS is limiting the entanglement of generated photons. According to equation 2.4 the FSS is a measure of the anisotropy of the confining potential. For InGaAs/GaAs QDs three effects are mainly contribution to an anisotropic confinement potential:

1. A **structural elongation** of the QD. As visible in figure 2.4(b) QDs grown on (001) GaAs tend to have a different size along the $[1\bar{1}0]$ and [110] direction. This is related to the different mobilities of ad-atoms during growth.

2. The strain induced in the material during the QD growth results in an asymmetric **piezoelectric potential** [Gru95, Sti99]

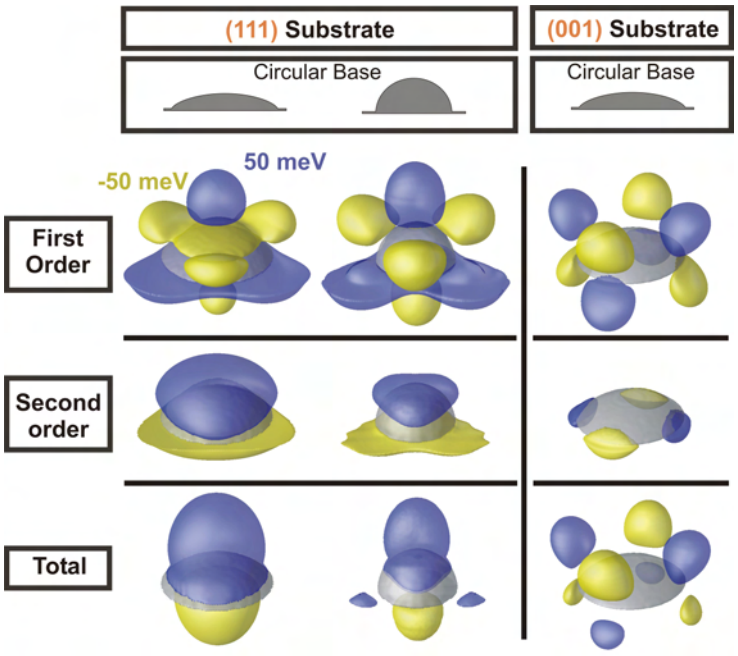

Figure 2.8: Piezoelectric field for lens shaped QD grown on (111) left and (001) GaAs substrate

3. The QD-matrix interfaces, even for a perfect pyramid, are not equivalent due to the atomistic symmetry present in the zinc-blende lattice. This interface effect is enhanced by strain and relaxed by intermixing [Bes03].

4. Randomly distributed In in alloyed InGaAs [War09].

These effects lead to a reduction of the carrier confinement symmetry to C_{2v} or lower and are an intrinsic characteristic of the (001)-substrate orientation. For InGaAs/GaAs QDs usually substrates oriented in the (001) direction are used. All samples in this work were grown on this substrates orientation except the ones in chapter 6.

For InGaAs QDs grown on (001) GaAs FSS values ranging from -80 µeV up to 520 µeV [Bay02, Hö4, Lan04, Kow05, Seg05] have been observed. The FSS can be manipulated by different techniques such as thermal annealing [You05, Seg06], additional external stress [Sei06] or electric fields [Hö4, Kow05]. In fact, both experiments demonstrating the generation of entangled photon pairs for the first time employed an electric field [Ste06] or spectral filtering [Ako06].

Three of the four above mentioned effects, which lower the symmetry, can be eliminated by changing the substrate orientation to (111). From AFM studies [Lob98] on this substrate direction an at least three-fold rotational symmetry of the QD structure can be expected.

The difference of the piezoelectric field has been studied using strain depend 8-band-k·p theory in conjunction with the configuration-interaction (CI) method [Sch09]. Figure 2.8 compares the impact of the substrate orientations on the piezoelectric potential for lens-shaped QDs chosen as model

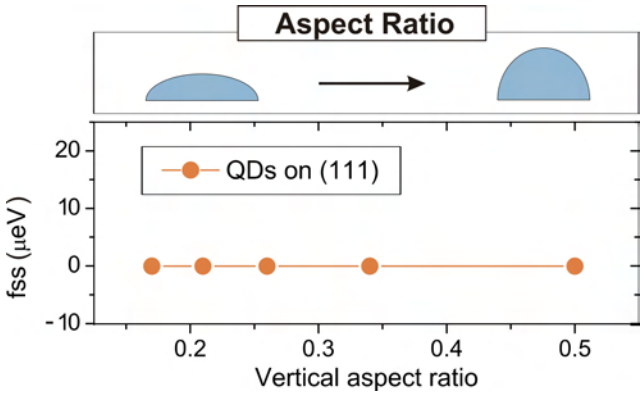

Figure 2.9: Fine-structure splitting calculated by strain dependent 8-band-k·p theory [Sch09]. In contrast to (001) GaAs, for the (111) substrate the fine-structure splitting is expected to be zero for all aspect ratio.

system: for the (111)-grown QDs the potential shows C_{3v} symmetry and a strong gradient along the growth direction, in contrast to the (001)-grown counterpart with only C_{2v} in-plane symmetry and no significant potential drop along the (001) axis. The field distribution of the (111)- grown QD is similar to the one of c-plane wurtzite-type GaN/AlN or InN/GaN QDs [Win06]. The magnitude of the potential drop, however, is much larger for the nitride QDs and the field is additionally superposed by pyroelectric effects, which do not occur in zinc-blende crystals.

In QDs In concentrations up to 100% can be achieved, which consequently leads to a large strain inside the QDs. As a result, nonlinear piezoelectric effects cannot be neglected in QDs. As can be seen in figure 2.8 for (001)- grown InAs QDs, first- and second-order effects compensate each other inside the QD, whereas in (111)-grown InAs QDs (figure 2.8, left and center) the second- order contributions are clearly dominant and therefore determine the orientation of the piezoelectric field.

The few-particle properties such as fine-structure splitting and biexciton binding energies are calculated using the configuration interaction model [Bra00, Sch09] taking into account direct Coulomb interaction, exchange (including dipole-dipole terms) and large parts of correlation effects. In figure 2.9 the calculated values of the fine-structure splitting as function of the QDs vertical aspect ratio are shown. In contrast to (001)-QDs non-alloyed (111)-QDs exhibit no FSS as expected from the symmetry considerations and constitute a promising system for the generation of entangled photon pairs.

2.3.4 *Electrical Pumping in a pin Diode*

A semiconductor QD can be filled with charge carriers either optically or electrically. In photoluminescence experiments, the absorbed photon lifts an electron from the valence band into the conduction band, thus generating an electron and a hole. The energy difference between the photon energy and the band gap can be transferred to phonons. If the electrons and holes

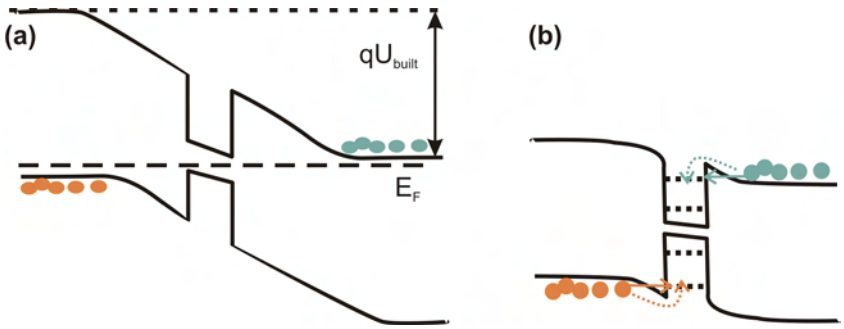

Figure 2.10: Band diagram of a pin junction with embedded QDs: (a) In thermal equilibrium the built-in potential prevents carrier injection into the QD. (b) For an applied bias close to the flatband condition the charge carrier can be injected either by resonant tunneling (straight arrow) or overband (dashed arrow) injection.

are generated in the vicinity of a QD they will relax to the lowest free level and can recombine there.

For the realization of compact devices electrical injection of charge carriers is more preferable. This can be realized using a pin junction:

When the impurity type in a single crystal semiconductor structure changes from acceptors (p-type) to donors (n-type) a pn junction is formed. On the p-side, the holes are the majority carriers and a form an attractive potential for electrons in the n-side. The electron diffusion into the p-side leaves positively charged donors in the n-side. The same is valid vice versa for the holes and the p-side. As a result in the middle of the pn junction a region without free charged carriers, the *depletion region* is formed. The charged ions in the depletion region create an electric field, which opposes the carrier diffusion.

The width and electric field distribution strongly depends on the doping profile and can be controlled for example by embedding an undoped intrinsic region in the middle of the pn-junction, thus creating a pin-diode.

Figure 2.10 shows the band diagram of a pn junction with embedded QDs. In thermal equilibrium the QDs are in the depletion region. The Fermi-energies of the p- and n-side are matched, resulting in a built-in potential. The built-in potential $U_{built-in}$ depends on the doping and can be described for an abrupt pn junction in a non-degenerated semiconductor by[Sze98]:

$$U_{built-in} = \frac{kT}{q} \ln\left(\frac{n_{no}}{n_{po}}\right), \tag{2.7}$$

where n_{no} and n_{po} denote the concentration of free electron and holes, k being the Boltzmann constant and T the temperature.

To inject charge carrier into QDs a bias in forward direction has to be applied. Thus electrons and holes are injected from n- and p-side by lowering the potential barrier. If the applied bias equals to the built in potential $U_{built-in}$ the diode is in the *flat-band condition* and charge carriers are injected along the bands into the QD. For a slightly lower bias, as depicted

in figure 2.10 b) a triangular barrier may persists. Nevertheless, charge carriers can be injected into the QD either by resonant tunneling into excited states of the QD (straight line) [Fryoob] or by thermal activation above the barrier (dotted line).

The electric field at the QD position will not decrease linearly with the applied bias. The ratio between the drop of the electric field and the applied bias is called the lever arm.

Current Constriction by an Oxide Aperture

The current flow can be constricted by an oxide aperture as it is commonly used in Vertical Cavity Surface Emitting Lasers (VCSEL) [Haio2]: $Al_xGa_{1-x}As$ layers with a high content of Al can be oxidized to Al_xO_y in vapor. In an etched mesa structure the oxidation process will start at the side wall surface and propagate towards the mesa center. If the oxidation process is stopped at the right time, only a small aperture of $Al_xGa_{1-x}As$ will remain in the mesa center. Since Al_xO_y has a much larger band gap than $Al_xGa_{1-x}As$ the current will flow only through the aperture. Thus the current path can be controlled to pump only one single QD.

Quantum Confined Stark Effect

An electric field in the QDs has influences on their optical properties. An electric field induces the following three effects to the electron and hole wavefunctions:

1. The electron and holes will follow the electric field. Hence the recombination energy will be lowered
2. The overlap between both wave functions will is reduced resulting in lower oscillator strength. Consequently the integrated intensity of the luminescence will decrease.
3. Due to the spatial electron-hole separation the exciton binding energy reduces, resulting in increased recombination energy.

Since the first effect is larger than the third one this results in a red shift of the luminescence for an increasing electric field [Mil85]. Following the notation in atomic spectroscopy this is called the *Quantum Confined Stark Effect* [Fryooa].

Note, that in electroluminescence the electric field in the QD is *decreasing* for an increased applied bias in forward direction. Hence, the luminescence demonstrates a blue shift for increasing bias.

2.4 PHONON COUPLING

The QDs are part of a crystal structure and interact with lattice vibrations. The lattice vibrations are described by a quasiparticle the phonon. This section briefly describes the most important properties of phonons, a good overview can be found in [Iba08, Str01].

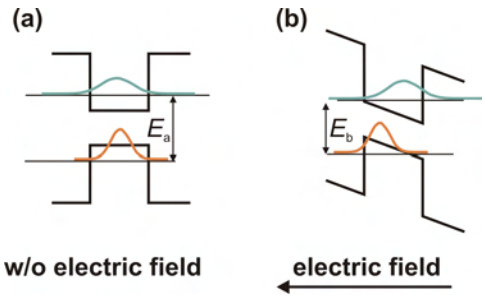

Figure 2.11: Schematic electron (blue) and hole wavefunction (orange) (a) Without an electric field. (b) In an electric field the electron and holes are separated and the recombination energy decreases.

The multi-particle state of the crystal atoms and electrons is described by the following Hamiltonian:

$$H = H_{ion} + H_{elec} + H_{elec+ion}\,, \tag{2.1}$$

where H_{ion} is the operator for the ion, H_{elec} for the electron and $H_{elec+ion}$ describes the interaction between both. The corresponding eigenvalue equation describes the total energy of the whole system. In the *adiabatic approximation* the electrons follow the movement of the ion instantaneous, since electrons have a much smaller mass than the ions. Also it is assumed, that the ions respond only slowly to changes in the electron configuration. The Hamiltonian thus can be separated into a part for the ions and one for the electrons and the interaction between both systems can be treated by perturbation theory.

Since the ions in the solid state move only slightly from their equilibrium positions, their potential can be described by a Taylor expansion. In the *harmonic approximation* the Taylor expansion is stopped at the quadratic terms. The resulting Hamiltonian for the ions reads:

$$H_{ion}(\mathbf{X},\mathbf{P}) = \sum_i \frac{P_i^2}{2M_i} + \frac{1}{2}\sum_{i,j} X_i W_{i,j} X_j\,, \tag{2.2}$$

where M_i is the mass of each atom, and X_i and P_i are position and momentum operators for the i-th atom. W_{ij} describes the coupling potential between the i-th and j-th atom. This Hamiltonian is similar to a system of coupled harmonic oscillators, where the matrix element W_{ij} of the Taylor expansion of the potential acts as spring constant.

Assuming a perfect crystal with infinite translation invariance the deflection of the ions can be *Fourier transformed* and described by *Bloch-waves*:

$$u_\alpha(\mathbf{k},\omega) = u_\alpha e^{i(\mathbf{kX}-\omega t)}\,, \tag{2.3}$$

where $u_\alpha(\mathbf{k},\omega)$ represents the oscillation state in which all ions are oscillating with the frequency ω and the amplitudes u_α is propagating as plane wave in direction of the wave vector $\mathbf{k}$. The index α runs along all possible

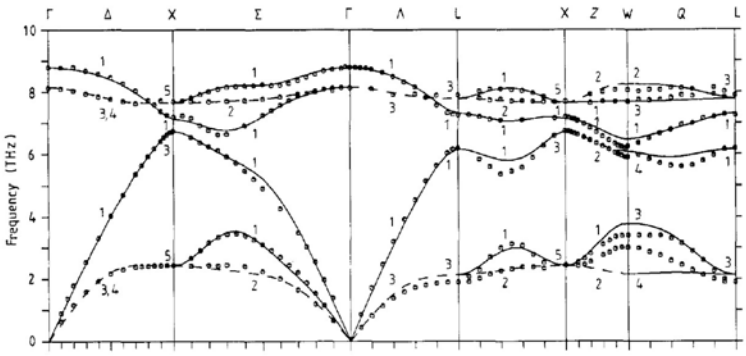

Figure 2.12: Phonon dispersion curve of GaAs. The experimental data at T = 12 K are given by crosses. The lines describe results of model calculations using the rigid-ion model. The letters on top gives the notation for the symmetry direction or points. The number i refer to the symmetry representation R_i of the corresponding branches. Taken from reference [Str90].

coordinates in the unit cell. In zinc-blende crystals the two different atoms give rise to three moving directions resulting in $\alpha = \{1,2,..,6\}$.

By this Fourier transformation the eigenvalue problem of equation 2.2 is solved by:

$$\sum_{\alpha} \left[D_{\alpha'\alpha}(\mathbf{k}) - \omega^2 \delta_{\alpha'\alpha} \right] u_{\alpha'} = 0 \,, \tag{2.4}$$

where $D_{\alpha'\alpha}$ are the Fourier transformed matrix elements of the potential W_{ij}.

The resulting $\omega(\mathbf{k})$ is the phonon dispersion. For a simple chain of single atoms this is given by: $\omega(\mathbf{k}) = 2\omega\,|\sin(ka/2)|$.

In ionic crystals with two different atoms two types of phonons appear: If both atomic species in the unit cell oscillate in phase the corresponding quasiparticle is referred to as *acoustic* phonons, since the situation is similar to the propagation of sound. If the atoms are oscillating in opposite phase a time dependent electrical dipole is induced. This dipole can couple to an electromagnetic field. Consequently these phonons are called *optical* phonons. For two atomic systems both types of phonons have three modes depending on the direction of the oscillation in comparison to the wave vector $\mathbf{k}$: For longitudinal phonons the ions oscillate in the direction of $\mathbf{k}$, whereas the oscillation in the two perpendicular lead to transverse phonons. Hence, the phonon modes are labeled as longitudinal acoustic (LA), transverse acoustic (TA) longitudinal optical (LO) and transverse optical (TO) phonons.

Figure 2.12 shows the dispersion curve of GaAs, measured by neutron scattering and calculated using the rigid-ion model [Str90].

Due to $\mathbf{k}$ conversation in photoluminescence experiments mainly the phonons near the Γ-point interact with photons. The following table gives

the values for optical phonons in GaAs and InAs at 100 K at the Γ-point [Lan87]:

Material	LO (meV)	TO (mev)
GaAs	36.39	33.37
InAs	30.00	27.34

2.4.1 *Electron-Phonon Interactions*

The electronic state of the semiconductor is influenced by the phonon coupling and can be described by a Hamiltonian H_{e-ph}. In the following only the two main interactions with optical phonons will be described:

An optical phonon leads to a microscopic deflection of the atom position in a unit cell. As a result the binding energy and thereby the energy bands changes. This *deformation potential coupling D* can be described by the Hamiltonian

$$H_{e-ph} = D_{n,j}\frac{u}{a}, \tag{2.5}$$

where u is relative change of the atom position and a the lattice constant.

In polar semiconductors such as GaAs a long-wavelength LO phonon leads to macroscopic dipole. The influence of this dipole on the electrons is described by the *Fröhlich coupling*. The strength of the electron-phonon interaction is expressed by a dimensionless Fröhlich coupling constant α, which has been determined for a number of semiconductor materials.

In polar crystals the Fröhlich interaction is the dominating part of the phonon electron interaction. A good description of the Fröhlich coupling in QDs can be found in [Min01].

The strength of the optical phonon coupling is usually measured by the Huang-Rhys factor S. It describes the probability of optical phonon emission during the radiative recombination of an electron-hole pair [Hua50]. S is described by the sum in the k-space over the phonon-exciton matrix elements M_k.

$$S = \sum_k \frac{|M_k|^2}{(\hbar\omega_{LO})^2}\,. \tag{2.6}$$

Fundamentally S can be measured by comparing the intensity of the zero-phonon I_{ZPL} line with the n-th phonon replica I_n [Hei99b]:

$$I_n/I_{ZPL} = S^n e^{-S}/n!\,, \tag{2.7}$$

2.4.2 *Phonons in Quantum Dots*

In the description of phonons above a perfect infinite extended crystal was assumed. The growth of quantum dots may invalidate this assumption due to several effects:

- The QDs consist of a different material, having a different phonon dispersion and hence different energy.
- The QD growth is strain driven. Strain in a material changes the coupling potential between the atoms W_{ij} and consequently the phonon energy [Cer72].
- The QDs represent a defect in the crystal, and thus complicate the description using *Bloch waves*. Single ad-atom in crystal leads to *local vibrational modes* [Thu95].

Nomura et al. [Nom92] calculated the localized modes in spherical CdSe and GaAs micro-crystals. The resulting phonon modes are similar to the spectra of the H-atom, but are barely relevant for realistic QD structures.

A theoretical study of the influence of QDs on the phonon energy has been done by Grundmann et al. 1995 [Gru95]: In a first step they calculated the strain induced by the QD growth in a box of arbitrary voxels (volumetric pixel). For each voxel the strain-induced shift of the phonon frequency was calculated. By a statistic analysis common frequencies existing on a macroscopic scale are found. As a result LO-type InAs phonons with an energy of 32.1 meV localized in the QD are predicted.

Since the phonon replica intensity is some orders of magnitudes smaller than the zero phonon line, the phonon interaction has been studied mostly on QDs ensembles. Here the homogeneous broadening hides details of the phonon coupling. In photoluminescence and photoluminescence excitation spectroscopy an enhanced LO-exciton coupling has been found [Hei99b] for QDs compared to bulk material. The separation of the electron and hole wavefunction in the QDs results in a dipole, for which the Fröhlich coupling is enhanced.

The phonon coupling is also of importance for the electronic state in the QDs. The energy of states with different spins differs in energy in QDs, due to the exchange interaction (see section 2.3.3). Hence, even if a spin-flip occurs by scattering with the nuclear spin of crystal atoms, a phonon has to be involved for energy conservation. Therefore phonons have an influence on the dark-state blocking mentioned in section 2.3.3.

2.5 MICROCAVITIES

The emission properties of dipole can be influenced by coupling to the optical modes of a microcavity. The following section gives a brief introduction into the microcavities. An excellent description microcavity in semiconductor is given by Kavokin, Baumberg and Malpuech [Kav08].

Microcavities have a resonator length in the order of the resonant wavelength λ and the minimum length is given by: $l_{min} = \lambda/(2n)$, where n is the refraction index.

Microcavities are usually realized by two planar mirrors. In semiconductor devices such a mirror can be made of alternating layers with different refraction index. Given a correct layer thickness these distributed bragg

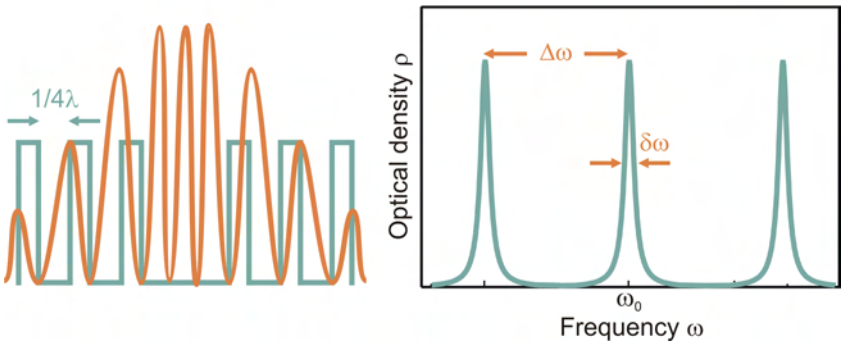

Figure 2.13: Left: Electric field and refractive index distribution in a DBR based 3/2 λ cavity. Right: Optical density in a one dimensional microcavity with losses.

mirrors (DBR) act like planar mirror. The reflectivity and thereby the out-coupling losses dependence on the number of DBR layers and the change in the refractive index. The larger the refractive index changes, than less layers are necessary for a given reflectivity.

The electromagnetic wave is not totally reflected at the beginning of the DBRs, but will penetrate into the DBR. For the calculation of the optical modes in DBR microcavities it is important to include the penetration depth to obtain a correct mode volume. Figure 2.13 left shows the change of the refractive index (blue) and the electric field (orange). The shown cavity has a $3/2\,\lambda$ thickness which is also used in this work. A dipole should be placed in the antinode of the cavity electric field.

Since the DBRs are usually consist of quarter-wave layers they are reflective only for a limited band with. This is called the *stop- band*. Outside the stop-band no microcavity is formed and no resonance will appear.

In a microcavity the optical density for resonance frequencies are enhanced, while the density for other modes is suppressed: For a perfect resonator with no losses only delta-like modes, corresponding to standing waves, are allowed. The optical density of all other frequency will be zero. Optical losses κ out of the cavity results in broadening of the resonances. The allowed frequencies are broadened to Lorentz distributions. Figure 2.13 shows the optical modes for a one dimensional microcavity.

Microcavities are usually described by two parameters. The Finesse of cavity is given by the distance between resonance $\Delta\omega$ and their width $\delta\omega$:

$$F = \frac{\Delta\omega}{\delta\omega} \tag{2.1}$$

and describes the free optical space between two modes.

Most important for the coupling effects to cavity modes is the quality factor

$$Q = \frac{\delta\omega}{\omega_0}, \tag{2.2}$$

which is defined as the quotient of the resonant width $\delta\omega$ and the resonance frequency ω_0. The Q-factor is a measure of the rate at which optical energy decays from within the cavity. Consequently the photon number lifetime in the cavity is given by $\tau = Q/\omega_0$.

Strong Coupling

The photon in the cavity and the excited state of the dipole (in this work the exciton) can be considered as two coupled oscillators. If the total scattering rates κ of both the cavity photon and the exciton is less than the coupling rate γ a new regime of optical physics can be reached. In this *strong coupling* regime a new quasiparticle the *polariton* appears. The polariton is half-light, half-matter and has a wavefunction described by a superposition:

$$\Psi_{\mathrm{polariton}} = \frac{1}{\sqrt{2}} \left(\Psi_{\mathrm{photon}} \pm \Psi_{\mathrm{cavity}} \right). \tag{2.3}$$

The system oscillates between the photonic and the excitonic state with the Rabi frequency Ω, resulting in a splitting of the resonant luminescence lines into an upper and lower polariton brunch. The strong-coupling between a microcavity and QDs has been demonstrated 2004 by two groups independently [Rei04, Yos04].

For single photon emitters the strong coupling regime should be not entered for two reasons: First the single photon should exit the cavity to be used in quantum optic experiment. The strong coupling is characterized by the fact, that the photon will be rather absorbed by the QD than emitted. This is not suitable for high photon rates. Second, if the exciton get pumped while the polariton exists lasing may occur. The lasing characteristic from a single QD in a microcavity has been demonstrated recently [Nom10]. Section 2.2 describes why lasers cannot used as true single photon sources, since there is always a probability of two photons per pulse.

2.5.1 *Purcell Effect*

In the weak coupling regime, where the probability of reabsorption of the photon is less than the probability of escaping, the spontaneous emission rate can be enhanced [Pur46, Sol01]. This is described by the Purcell factor F_P which is given by:

$$F_P = \frac{\Gamma_{cav}}{\Gamma_{vac}} = \frac{\tau_{vac}}{\tau_{cav}}, \tag{2.4}$$

with Γ_{cav} the spontaneous emission rate within the cavity and Γ_{vac} in the vacuum field and τ_i the corresponding lifetime of the excited state.

The Purcell factor F_P for a given cavity can be derived from *Fermis golden rule* which describes the spontaneous emission rate from an initial state i to a final state f :

$$\Gamma_{i\to f} = \frac{2\pi}{\hbar^2} |\langle f|H|i\rangle|^2 \rho, \tag{2.5}$$

where H is the perturbing Hamiltonian and ρ is the density of the final state. A microcavity enhances the optical density of the final state (the generated photon) and hence increases the emission rate. By calculating the optical density of the resonance mode in a three-dimensional microcavity and comparing this with the vacuum field optical density the Purcell factor can be derived to:

$$F_P = \frac{\rho_{cav}}{\rho_{vac}} = \frac{3\lambda_0^3}{4\pi^2}\frac{Q}{V}, \tag{2.6}$$

where V is the effective mode volume of the cavity and λ_0 the resonance wavelength. Equation 2.6 is valid if the dipole is placed in the antinode of the cavity electric field, is spectrally in resonance with the cavity λ_0 and is directed perpendicular to the cavity.

For a high Purcell factor and hence a high photon rate the ratio Q/V has to be as large as possible. Practically an arbitury large ratio is difficult to achieve, since smaller cavities often have restriction in the maximum Q-factor. Furthermore the top mirror of the cavity should be partially transparent to couple the photons out of the cavity.

As a consequence the effective cavity mode should be as small as possible. For this purpose the oxide aperture for current constriction (see section 2.3.4) is helpful. AlO_x has a different refraction index then the AlGaAs. Calculations using the eigenmode technique predicts [Mö9] that the optical mode of the cavity is mostly confined in the remaining AlGaAs aperture. Thus the cavity mode is strong reduced.

2.5.2 *Out-Coupling Efficiency*

Beside the enhanced spontaneous emission rate the coupling to a microcavity also increases the number of photons, which leaves the cavity. A simple mirror below the QD layer would already double the number of photon leaving the device on top. The microcavity works even better:

The separation of the electron and hole wavefunction in the QD results in a dipole. Due to the small size of the QD of only a few nanometers this dipole small. Hence the QD will emit photon in all direction almost homogeneously. The top of the diode represents a GaAs-air transition with a change of the refraction index of about 3.5 to 1 for the near infrared. Consequently, all photon reaching the top surface with an angle larger than 16 ° will be reflected back. Integrating over the whole solid angle yield that, only about 3% of the photons emitted by the QD will exit the device on the top surface.

The microcavity enhances the optical density perpendicular to the mirrors, meaning in the growth direction. According to Fermis golden rule (eq. 2.5) the QD will emit photons preferable in this direction. Hence the angle of photons reaching the top of the diode will be reduced and the out-coupling efficiency increased.

The out-coupling can be controlled by the ratio of the reflectivity of the top and bottom DBR mirror.

3 EXPERIMENTAL

This chapter describes the experimental techniques, used in this work to study the non-classical light emission from a single QD. The first section 3.1 presents the main parts of the custom-built micro-luminescence setup. This setup enables to study the luminescence of single QDs under optical and electrical excitation with the required spatial and spectral resolution. A new type of detectors was used for the detection of single photons (section 3.2). The working principle and system characteristics of these superconducting single photon detectors are discussed in detail. The photon correlation measurement principle is described in section 3.3. Possible errors of this measurement are also discussed and how to account for them in the analysis of the data. Finally, section 3.4 describes the growth and processing steps of the samples used in this work.

3.1 SINGLE QD SPECTROSCOPY

To study the luminescence of a single or few self-organized QDs a system with a spatial resolution of less than 1 µm and a high spectral resolution (<100 pm) is necessary. Three techniques are commonly used for single QD spectroscopy: In the cathodoluminescence the sample is excited by a high energy electron beam of a scanning electron microscope (SEM) and the luminescence is collected by an elliptical mirror into a monochromator [Chr91]. This system has the advantage of a high spatial resolution combined with the imaging technique of the SEM. Unfortunately the required electron energy limits the possibility to change the excitation situation. The second technique is the scanning near field optical microscopy (SNOM), where a tapered fiber is used. The fiber has at the end a diameter of less than the wavelength and the evanescent light field excites the sample. This results in a spatial resolution better than the diffraction limit [Poh84]. The disadvantage of this technique is the low collection efficiency of the sample luminescence.

In this work the third approach for single QD spectroscopy, the micro-photoluminescence has been realized. Although the setup allows optical and electrical excitation in this work it will be refered as micro-PL. An overview of the micro-PL setup is shown in figure 3.1. The main components of the custom-built setup will be described in the following sections. The Hanbury-Brown Twiss (HBT) interferometer for the photon correlation measurements will be described later in section 3.3 on page 44

3.1.1 *Confocal Laser Scanning Microscope*

A central part of the micro-PL is the confocal laser scanning microscope (CLSM), which ensures the required spatial resolution and allows changing

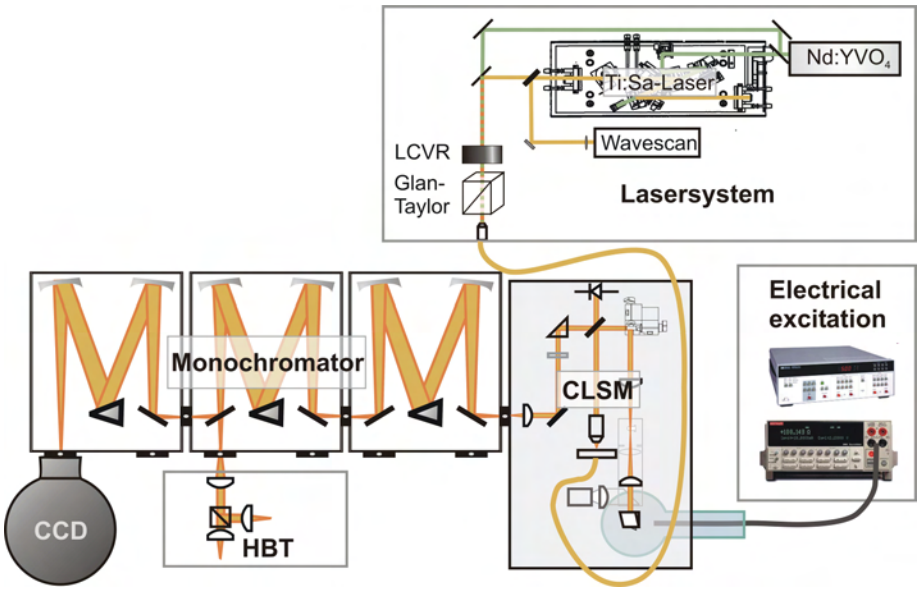

Figure 3.1: Main components of the micro luminescence setup

the detection spot on the sample surface. A detailed schema of the light path in the CLSM is shown in figure 3.2.

The excitation laser is directed to the CLSM via a single mode fiber. This ensures the same starting point of the light path, independent on the laser source and it adjustment. The fiber output is a good approximation to a point light source, hence the light can be parallized by a microscope objective with tenfold magnification. The excitation light is coupled into the system by a beam splitter. This can be either a dichromatic mirror, for green excitation, or a 95:5 beam splitter for resonant excitation and electroluminescence measurements. In both cases the transmitted light is detected by a Si-pin diode and the excitation intensity is recorded.

From the beam splitter to the sample the excitation and luminescence paths are exactly the same, with only opposite directions. This part allows the scanning of the excitation spot. Figure 3.3 shows the scanning principle in detail: The parallel light beam is redirected by a galvanometer mirror scanner (Cambridge Technology) in x- and y-direction. Two lenses make an image of the mirror center to the entrance of the microscope objective. The focus of the first lens is at the mirror and of the second on the objective, whereas their focuses in the center are at the same position. Thereby a parallel light beam always enters the objective with an angle controlled by the mirror scanner.

The microscope objective is an Olympus LMPlan IR 100x/0.8. For this objective the focus is on a plane (flat corrected) and the position depends on the angle of incidence (see figure 3.3b). The numerical aperture of NA = 0.8 yields into a spot diameter of about theoretically 0.6 µm, but due to disturbing by the window of the cryostat the spot size is about. 1.5 µm. Beside the spatial resolution, the working distance of the objective is 3.6 mm, enabling to collect the luminescence from the sample in the cryostat through the window. The lenses are anti reflex coated for the near infrared range

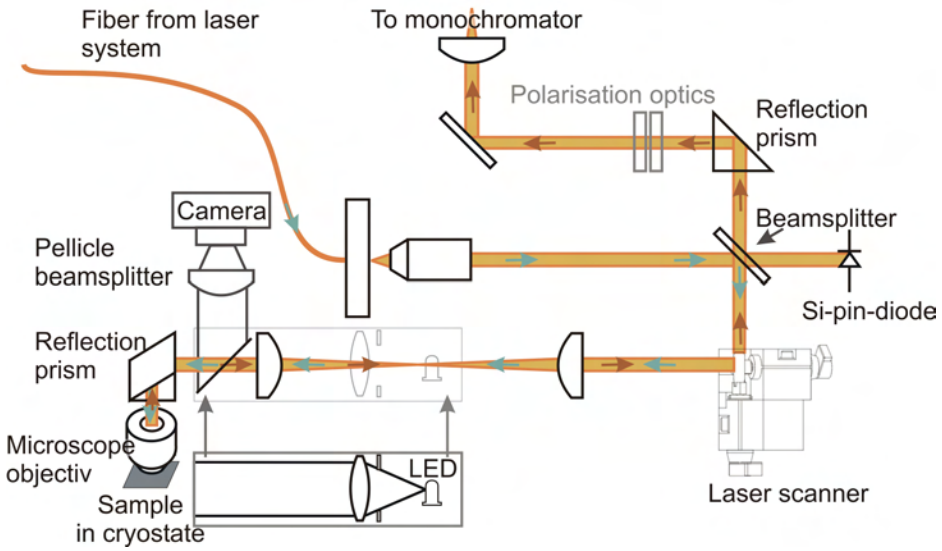

Figure 3.2: Optical path in the confocal laser scanning microscope. The path of the excitation light is marked with green arrows, and the sample luminescence with red arrows. The LED for illumination can be switched to the grey marked position.

(NIR), allowing high transmittance for the sample luminescence. The sample luminescence is collected by the same objective and directed the same way back to the beam splitter.

For polarization dependent measurements polarization optics can be placed in the beam path, after the reflection prism (which has less polarization effects, than a silver mirror). The polarization optics consists of a linear polarizer and $\lambda/2$ plate. The linear polarizer is rotated to the position of maximum transmittance of the monochromator and the rotation of the $\lambda/2$ plate defines the detected polarization direction. This removes the transmittance characteristic of the monochromator in dependence of the polarization. Although the mirror scanner and beam splitter influences the polarization, the suppression for orthogonal polarized lines is better than 80 %.

The spatial resolution of the setup is controlled by the size of the excitation spot, whereas the detection spot is much larger. This is good for photoluminescence measurements, where the luminescence is controlled by the size of the excitation spot. In CLSM systems the detection spot size is often controlled by a pin-hole in the focus of two lenses. This system should be placed somewhere in the parallel beam, for example at the position of the polarization optics and will introduce additional losses and requires accurate adjustment. In the setup presented here, the detection spot can be controlled by the monochromator slit in one direction and by reducing the binning in the detector in the other direction. This results in a detection spot size of about 3 µm in diameter.

The sample surface can be observed by a CCD camera and a pellicle beam splitter. The CCD camera is sensitive enough to observe a bright spot from the EL even from the luminescence of a single QD (for example see figure

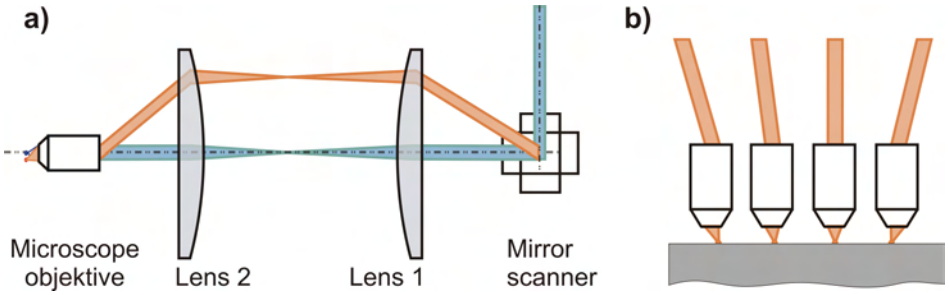

Figure 3.3: Scanning principle of the CLSM. a) By two lenses the light is directed to the microscope objective with changing angle, controlled by the mirror scanner . b) This results into a change of the position on the sample.

4.9). A white LED can be switched in the system for illuminating the sample surface. For higher luminescence intensity in the detection, the pellicle can be removed without any beam dislocation.

3.1.2 *Detection System*

A triple monochromator with 500 mm focal length in each stage ensures the spectral resolution of the setup. Each stage is equipped with three gratings which can be easily changed by the controlling program. This makes the system very flexible: The first two stages can be used in additive or subtractive mode, for high resolution or overview spectra. For the cross-correlation measurement in the second version of the HBT (see section 3.3.2 on page 45) the first two stages are used independently, but still high resolution spectra with the CCD are possible, simply by changing the mirrors in the monochromators. In the highest resolution mode, with all three stage with 1200 gr/mm grating the resolution at the CCD is about 12 pm FWHM at 950 nm. The spectral window on the CCD in this mode is only 6 nm, whereas in the subtractive mode it is 30 nm. A larger spectral window is very useful especially for mapping of the sample surface. Luminescence with larger spectral distance (for example from QDs of different sizes) can be studied within one scan and therefore better analyzed.

The light is detected by array detectors for spectral analysis or single photon counting detectors (see section 3.2) for correlation measurements. As array detector a Si-based CCD or an InGaAs-Array are used. The CCD consists of 100 lines of 1340 pixel, with a pixel dimension of 20 x 20 µm. Usually all 100 lines are binned together, but for increasing the spatial detection resolution, the binning can be reduced. The CCD is a liquid nitrogen cooled Roper Scientific camera (100BR) and optimized for the NIR, with a maximum detection efficiency of nominally 90 % at 800 nm. Due to the Si band gap the detection wavelength is limited to $\lambda \lesssim 1000$ nm. For longer wavelengths up to 1700 nm a nitrogen cooled InGaAs array (Roper Scientific 1024-1.7 LN) can be used. It consists of a line of 1024 pixel with a dimension of 25 x 500 µm. Due to the poor material quality this system has a less detection efficiency (up to 80% at 1300 nm) and much higher noise than the CCD. Almost all spectra in this work were recorded with the CCD.

3.1.3 *Excitation Sources*

The sample can be excited both optically and electrically. For electrical excitation of diode structures (see sample description in section 3.4) four simple cables and one coaxial cable are mounted into the cryostat. The coaxial cable and its connectors have a bandwidth of > 1.6 GHz, whereas the simple cables are used to test up to five diodes in one cooling cycle. For cw measurements a Keithley 2400 source meter was used and pulsed excitation was done with a 3 GHz HP 8142 pulse generator.

For optical excitation two laser systems were used. A frequency doubled Nd:YVO_4 laser, emitting at 532 nm, was used for excitation far above the band gap of GaAs, whereas the Ti:Sapphire laser can be tuned to excitation energies resonant to wetting layer or QD states. This system can also be used for single QD photoluminescence excitation spectroscopy (PLE). The intensity of both systems can be controlled by a liquid crystal variable retarder (LCVR) and a Glan-Taylor polarizer.

3.1.4 *Data Acquisition and Analysis*

The whole system is controlled by a self-written Labview program. The program has several modes for the different measurement types:

- Mapscan: Measures the spectrum on different positions on the sample. Thereby the exact position of a QD can be determined
- Step and Glue: Measures spectra at different center wavelengths of the monochromator and glues them together to one overview spectrum.
- PLE: Measures a series of spectra in dependence on the excitation energy. This photo luminescence excitation spectroscopy gives access to excited states in the QD.
- Spectral Jitter: Measures a series of spectra, to study the spectral diffusion, which is helpful for the identification of luminescence lines from the same QD
- Laserpower and Voltage scan: Measures a series of spectra under different optical/electrical excitation power. This allows to identify the exciton- and biexciton-type emission in PL and EL
- Polarization scan: Measures a series of spectra for different polarizer position, for example to study the FSS
- Frequency scan: Measures a series of spectra under different repetition rates. This is necessary to identify to highest possible repetition rate under pulsed electrical excitation

The last four modes result in a three dimensional data set, which can be analyzed by a self-written Labview program. This program easily removes disturbing signals from the absorption of high energy particles (myons).

To study the energetic shift or intensity behavior the luminescence can be analyzed by fitting routines.

For measurements of long duration a drift of the sample position can be corrected automatically: After a defined time, the system performs a mapscan and adjust the sample position back to the maximum of the luminescence intensity. This auto-adjust mechanism is a key element in long-term measurements such as for example photon correlation measurements.

3.2 SINGLE PHOTON DETECTION

The detection of single photons requires detectors with high quantum efficiency. In these detectors the small energy of a single photon should be sufficient to trigger a detection event. Additionally a very low noise equivalent power (NEP) is crucial. Usually these detectors amplify a detection event into a single voltage pulse, rather than a continuous signal. Therefore they cannot distinguish between a single or multi photon.

In this section two types of detectors which were used in this work are described in detail. Besides these both detectors photo multiplier tubes or multichannel plates (MCP) may be used as single photon detectors. But for the near infrared region they usually have too high dark count rates and therefore to high NEP.

3.2.1 *Avalanche Photodiodes*

Avalanche photodiodes (APDs) consist of a semiconductor pin-junction, with an intrinsic layer of a few ten to hundred nm. On these diodes a large reverse bias is applied well beyond the breakthrough voltage. An absorbed single photon generates an electron-hole pair in the intrinsic layer. Due to the high electric field both carriers are separated, accelerated and generate further electron-hole pairs. This process is called the avalanche breakdown and generates an easily detectable current. The current may even reach current densities, which will destroy the diode. Therefore the applied bias must be reduced after the detection event by a so called quenching circuit [Cov96] as fast as possible. The time, required to stop the current and to reapply the reverse bias defines the dead time of the detector.

A trade off has to be found between quantum efficiency and time resolution of an APD: The larger the intrinsic region is designed, the larger the quantum efficiency will be especially in the near infrared. At the same time the avalanche process can start in a larger region resulting in a decreased time resolution.

In this work two single photon counting module SPCM-AQRH-13 from Perkin-Elmer were used. Due to the silicon band gap of 1.12 eV these silicon APDs are limited to photons with a wavelength < 1100 nm. The modules are NIR optimized and have a quantum efficiency of 23 % at 950 nm with a time resolution of 400 ps [Elm02] The dark counts are 200 c/s, with a maximum counting rate of about 5 MHz and a dead time of 35 ns. During the avalanche break down in these modules the generated electron and holes

can recombine and emit photons with a broad spectrum. This is the reason for the so called cross talk (see section 3.3.3)

Almost all commercial available APDs are based on silicon. InGaAs-APDs have the capability to detect photons with wavelengths up to 1600 nm. Unfortunately the defect density in this material system is too high, resulting in a too high dark count rate. These APDs have to be operated in a gated mode, where the bias is applied only in a short time window of typically a few nanoseconds, followed by a dead time of some microseconds. For the detection of untriggered light sources these detectors are not suitable. The development of high-speed InGaAs-APD, with high quantum efficiency is still under investigation [Yua10].

3.2.2 *Superconducting Detectors*

A new method for detecting single photons is based on ultra thin superconducting nano stripes. This method has been proposed in 1996 [Kad96] and is still in research. Up to date only the company Scontel, a spin-off of the Moscow Pedagogic University, is selling these detectors commercially.

Operation Principle

On a 4 nm thin niobium nitrate (NbN) film 120 nm thick stripes are processed. These stripes are formed in a meander resulting in a 10 x 10 µm square detector with a filling factor of 60 %. The size of the detector is adapted to the near field of a standard telecom optical fiber. The detector is operated at 1.8 K, well below the critical temperature T_C of 10.1 K, with a current density close to the critical current density j_C. An absorbed photon generates a so called "hot-spot" of a few excited electrons within the thermalization time of 6.5 ps [Ili00]. The generation of the hot-spot is mainly caused by destroying Cooper-pairs, but the exact generation process is still under investigation. The superconducting energy gap is two or three orders of magnitude less than in semiconductors, hence the required photon energy is very low and photons with a wavelength of up to a few µm can be detected [Ver02]. The size of the hot-spot increases, while hot electrons diffuse out of it. The hot-spot is a non-superconducting region and the current is forced to flow around it (see figure 3.4a), leading to an increased current density in the resulting superconducting portion of the stripe. If the stripe is small enough the current around the hot-spot exceeds j_C and the superconduction across the whole stripe collapses. Shortly after this, the reduced current in the stripe allows regeneration of the superconducting state within only 30 ps [Gol01].

The smallest part of the stripe determines the maximum applicable current, hence in order to achieve a high detection efficiency the current has to be as close as possible to j_C on the whole length of the stripe. This requires stripe processing with an accuracy of <10 nm along the whole meander with a length of 500 µm.

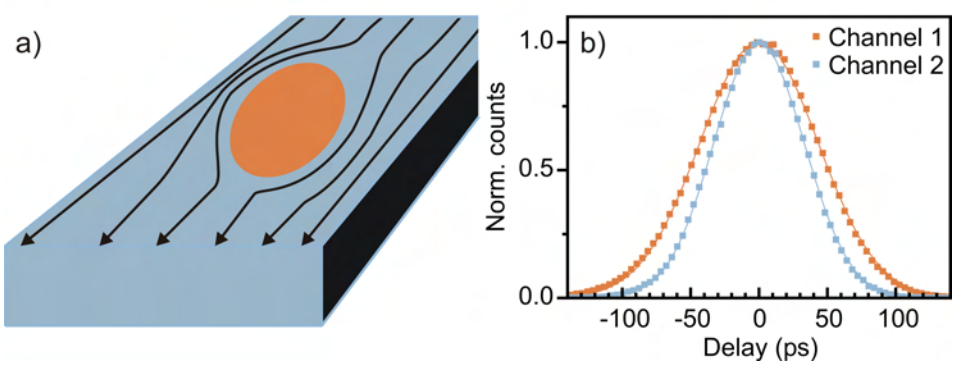

Figure 3.4: left: Principle of the superconducting single photon detector: An absorbed photon generates a hot-spot and the current in the remaining part increases the critical current. Right: Instrumental response function of both channels to a femto second laser pulse. The straight line indicates Gaussian fit with a FWHM of 100 and 78 ps for Channel 1 and Channel 2 respectively.

System Characteristics

Superconducting single photon detectors (SSPDs) are on the edge of the technology, therefore the used system has been tested intensely.

The detector system used in this work consists of two detectors and is mounted in a small cryostat tube, which can be inserted into 100l helium dewars. By reducing the pressure in the tube the helium temperature can be lowered down to 1.6 K, with a helium consumption of about 0.5l/hour. The photons are directed to the detector via a standard single mode optical fiber (SMF-28). The higher resistance of the SSPD during a detection event is amplified by a fast electronic into a 5 ns voltage pulse with an amplitude > 0.2 V.

The time resolution of the system was tested with a femtosecond Ti:Sapphire laser at 850 nm, a Si-APD with a time resolution of 40 ps and the PicoHarp 300 timing electronic. The Si-APD is optimized for high time resolution (30 ps) and has consequently low quantum efficiency. This is sufficient to measure the laser pulse but not good enough for single photon detection. Figure 3.4b (dashes) shows the measured instrument response function (IRF) of the two channels of the SSPD. A Gaussian fit (straight line) results in a FWHM of 100 and 78 ps for channel 1 and 2 respectively. Taking into account the time resolution of the Si-APD and the electronic the time resolution of the detector is 91 and 66 ps, which is more than 4 times faster than the single photon APD.

The quantum efficiency and the dark counts of the detector can be adjusted with the applied current. In figure 3.5 left the full symbols show the count rate of both channels in dependence on the current for a constant light signal. Only if the current is close enough to j_C the current outside the hot-spot exceeds j_C and a detection event occurs. Higher current allow even smaller hot-spots generated by the absorbed photon to push the current in the remaining superconducting part above j_C. Therefore the quantum efficiency increases with the current. With an increase of the current by 4 µA,

the count rate increases by three orders of magnitude and saturates at the maximum quantum efficiency.

The dark count rate (open symbols in fig. 3.5) increases with the current too, but much later than the signal counts. The increase of the dark counts can be separated in two parts: For higher current (> 20 µA for channel 1 and 21 µA for channel 2) the dark count rate increases exponentially and even exceeds the signal counts at 21.5 µA and 23.5 µA for channel 1 and 2 respectively. The dark counts in this current region are mainly generated by spontaneous phase-slip centers as described by the LAMH theory [Lan67, Qiu09] and by quantum fluctuation of the Cooper-pair density. The dark count rate R_{dark} in this current region can be written as: $R_{dark}(I) \propto R_0 e^{I/I_0}$ where the prefactor R_0 depends on the accuracy of device processing and temperature. The value of R_0 changes for more than 30 orders of magnitude for temperature close to T_C [Kit05]. Therefore it is crucial to reduce the helium temperature to 1.8 K for a detector system with low dark count rates.

For currents < 20 µA and 21.4 µA (for channel 1 and 2 respectively) the dark count rate does not follow the exponential drop and saturates to 5 counts/s. In this current region the dark counts are generated by thermal coupling to the detectors via the optical fiber. In order to reduce this coupling a 3 m long fiber, winded in the inner part of the cryogenic insert, is used. Beside the lower thermal conductance, the bending of the fiber makes it a spectral band filter and photons with long wavelength (> 2 µm) are blocked.

A good trade-off between signal and dark count rate for the detectors are 19.4 µA and 19.8 µA for channel 1 and 2, which are marked in figure 3.5. For this current the quantum efficiency of both channels were tested in the following way: The light of a tungsten lamp was spectrally filtered by a monochromator and coupled into a standard SMF fiber. The fiber was either connected to the detector or the output was focused on a Si-APD module, mentioned in section 3.2.1. The quantum efficiency of the Si-APD was taken from the data sheet [Elm02] and by comparing the count rates on the APD and the SSPD the quantum efficiency of the SSPDs was calculated. Therefore the coupling losses into the fiber can be neglected. Figure 3.5right shows the resulting quantum efficiency of both channels and the APD for comparison. From 900 to 1000 nm the quantum efficiency is almost stable at 23 % and 20 % for channel 1 respectively 2. For shorter wavelengths an increasing quantum efficiency of the SSPDs is expected [Ver02], but the optical fiber (see next part) reduces the photon flux to the detector for shorter wavelength.

Fiber Coupling

As mentioned above the light is directed to the SSPD by an optical fiber. The divergent beam of a standard SMF-28 fiber will not be larger than the detector size of 10 x 10 µm within a distance of less than 0.5 mm. This allows a system without any focusing elements in the helium cooled part. The SMF-28 fiber is single mode for the wavelength range of 1260-1620 nm, but even the multi mode field of shorter wavelengths will not be larger than the detector.

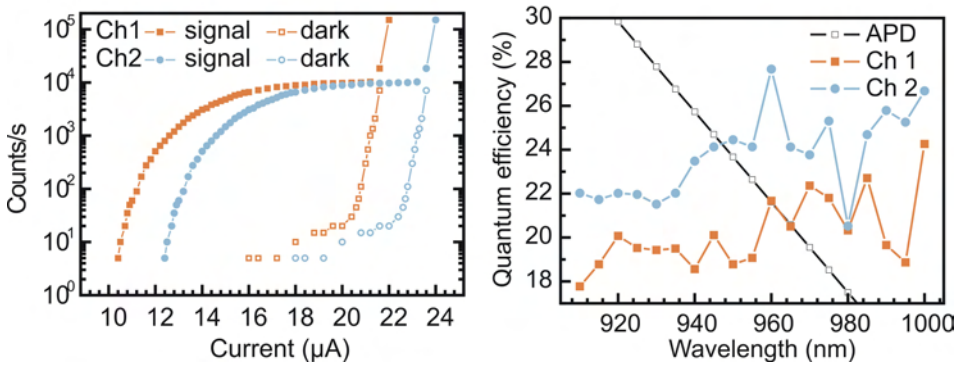

Figure 3.5: Characteristic of the used SSPD system. Left: Signal and count rate in dependence on the current. Right: measured quantum efficiency at 19.4 µA and 19.8 µA for channel 1 and 2 respectively for the wavelengths from 900 to 1000 nm. The quantum efficiency of the APD (open dots) was taken from the manufacture data sheet and used as reference.

The fiber is bend around the dipstick, which is inserted in the helium devar, to decrease the thermal coupling. The bended fiber also act as an optical filter for photon with wavelengths $\lambda > 1.8$ µm, which also reduces the dark count rate. The fiber is only specified for wavelengths between 1260-1620 nm and for other wavelengths some additional losses can occurre, resulting in a worse quantum efficiency of the detector system. Usually SSPD are used at 1.3 and 1.55 µm, but for this work the detector system was also optimized for wavelength of 900-1000 nm by a less bending of the fiber.

The SMF-28 has a core diameter of 8.2 µm with a NA = 0.14. For the coupling of the light into the fiber a standard microscope objective with 10x magnification and a NA = 0.25 is used. If the light on the objective entrance is a perfect parallel waveplane, this will result in a perfect in-coupling efficiency. In spite of beam disturbance in the micro-PL setup, especially in the monochromator, an in-coupling efficiency of up to 60 % has been achieved. To consider for chromatic aberration lens errors, the adjustment has been done with a laser at the same wavelength as the sample luminescence.

3.3 PHOTON-CORRELATION MEASUREMENT

The typical characteristic of a single photon source is the non-classical time distribution of the emitted photon, which can be described by the second order correlation function $g^{(2)}(t)$. This section describes the measurement principle for the $g^{(2)}(t)$ and how to calculate for possible errors of this measurement principle.

3.3.1 *Measurement Principle*

For the measurement of the second order correlation function $g^{(2)}(t)$ (see equation 2.1 on page 14) the temporal distribution of the photons has to be measured. Due to the limited time resolution and dead time of

available detectors the direct measurement of $g^{(2)}(t)$ for fast photon sources is impossible. The measurement can be approximated with an interferometer developed by Hanbury Brown and Twiss in 1956 to determine the angular radii of stars [Han56]. In the so-called Hanbury-Brown Twiss interferometer (HBT) the photons are directed on to a 50:50 beam splitter and detected by the detectors D1 and D2 in both arms (see figure 3.6 top). The time difference between a detection event on D1 and D2 is analyzed by a counting electronic and stored in a histogram with equal time channels. The histogram h(t) represents the number of events in dependence of the time delay. Because different detectors are used for the start and stop signal the problem of the detector dead time is eliminated.

The measurement of h(t) is a statistical process and therefore the noise is proportional to $\sqrt{h(t)}$. For a signal to noise ratio (SNR) of > 5 the number of coincidences per time channel has to be > 25.

The number of measured coincidences per second R_{coin} is given by the probability that after a detection event on D1 within the observed time window t_{wind} a detection event on D2 occurs. For an uncorrelated light source this is given by:

$$R_{coin} = R_{D1} R_{D2} t_{wind}. \tag{3.1}$$

If the correlation rate is higher, the detected light is somehow correlated, for example if the emission from an X and XX is collected.

From equation 3.1 it is obvious that the required measurement time for a given SNR is quadratically proportional to the detection rate. Highly efficient detectors, a setup with low losses and good adjustment are therefore crucial for the measurement of $g^{(2)}(t)$.

3.3.2 *Experimental Setup*

Optical Setup

The Hanbury-Brown Twiss interferometer has been realized in two different ways: In the first version (see figure 3.6 top) the output of the second stage of the triple monochromator is paralyzed and directed to a 50:50 non polarized beam splitter cube. Both outputs are focused either by lenses or microscope objectives to the APDs or SSPDs respectively. In this configuration the wavelength for both detectors is the same and the spectral resolution is 0.15 nm or 0.3 nm (for gratings with 1200 gr/mm and 600 gr/mm respectively). This setup has been used for most of the correlation measurements in this work. It can prove single photon emission from a single emission line.

In the second version (figure 3.6 bottom) the beam splitter is located in front of the monochromator. One arm is directed to the entrance of the first stage and the other to the second stage. The output of each stage is focused on detector D1 or D2, which thus can detect light of different wavelengths. Here the spectral resolution is reduced by a factor 2 to 0.3 nm and 0.6 nm.

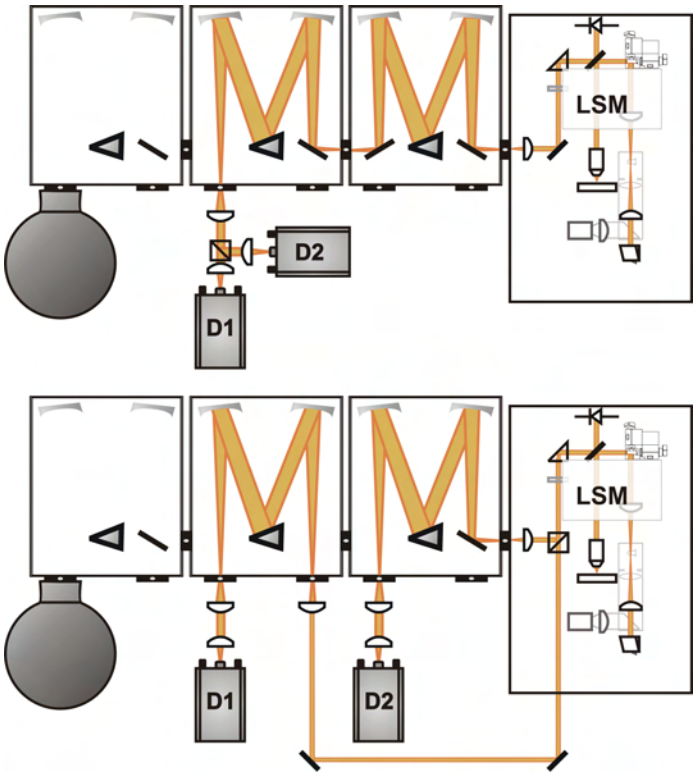

Figure 3.6: HBT setup for auto-correlation (top) and cross-correlation photon measurement.

This setup allows cross-correlation measurements, where one emission line gives the start pulse and another emission line the stop pulse. From this kind of photon correlation measurements the origin of both lines can be determined:

- If antibunching is visible, both lines originate from the same QD, but not from a single luminescence cascade as for example. XX→X
- If antibunching at zero and bunching for positive times is visible, the start emission line is biexcitonic whereas the stop emission line is excitonic. The same applies for vice verse.

The main disadvantage of the second configuration is the high complexity of the adjustment: As mentioned in section 3.1 the coupling into the monochromator defines the detection spot on the sample. This coupling has to be done twice and the detection spot for both monochromators should be the same. Due to the 3 m long path from the beam splitter to the second stage this coupling is very sensitive to instability of the whole optical setup.

Counting Electronic

The time difference between the start and stop pulse is analyzed by the PicoHarp 300 counting electronic from Picoquant. The PicoHarp 300 measures the time of a start and a stop pulse independently on an internal timescale. For each channel a table with the arrival time of a detection event is stored.

From this table the time difference and the histogram are calculated. This is in contrast to classical time-to-amplitude converters (TAC), which have a dead time of a few microseconds for resetting after a start pulse has been detected. Hence the electronic will not register every counting event of the detectors, resulting in a reduced correlation rate. Especially for high photon rates the measured coincidence rate with the PicoHarp 300 is in the range of the one obtained from equation 3.1, whereas the TAC has a much lower coincidence rate. For the measurement of negative times a delay of 60 ns, realized by a 12 m long cable, is add in front of the stop entrance.

The PicoHarp 300 has 65536 histogram channels with a minimum width of 4 ps, resulting in a time window of $t_{wind} = 262$ ns. As far as the time resolution of 4 ps is much higher than the time resolution of the detectors, 5 or 10 channels are binned after the measurement. This yields to a higher number of coincidences per channel and a better SNR of the measured correlation function.

3.3.3 *Possible Errors of Measurement*

High Photon Rate

The $g^{(2)}(t)$ function represents the probability, that a photon is emitted at the time t after another one. But in the measured histogram h(t) a coincidence at time t will be measured only when a photon is detected and no other photon has been detected before. Only if the observed time window is much smaller than the average time between two detection events, the histogram h(t) represents $g^{(2)}(t)$

The measured histogram is related to the $g^{(2)}(t)$ function via:

$$h(t) = (g^{(2)}(t)\, D)(1 - \int_0^t h(t')\, dt')\,, \tag{3.2}$$

where D is the detection probability of the setup.

The solution of this integral equation is given by :

$$\begin{aligned} h(t) &= (g^{(2)}(t)\, D)\, exp\,(-\int_0^t (g(t')\, D\, dt') && (3.3)\\ &\approx const.\, e^{-(R_D)t} \text{ (for large t)}, && (3.4) \end{aligned}$$

where R_D is the detection rate. According to 3.4 the measured histogram h(t) drops exponentially for long times, in contrast to the $g^{(2)}(t)$ function, which stays equal 1 for long times.

For all measurements presented in this work the detection rate R_D did not exceed 200.000 counts/s, resulting in an average time distance between two detection events of 5 µs, whereas the histograms are measured with a time window of up to 60 ns. This means the integral in 3.2 is almost zero

and the exponential drop is negligible. By normalizing h(t) the detection probability can be removed and h(t) represents $g^{(2)}(t)$.

Cross Talk

During the detection in an APD a photon may be emitted. In the first version of the HBT this photon can be reflected by the faces of the beam splitter cube to the other APD. The focusing lenses even increase this possibility. In such a case a photon will be detected with a fixed time difference $\triangle t$ to the first one and a bunching will be measured. In figure 6.2 on page 93 this bunching is visible for ± 7 ns. The cross talk can be reduced by the following actions:

- Add a band filter in front of one APD. The emitted photons are spectrally broad distributed and the major part will be absorbed.
- Reduce the numerical aperture in front of the APDs with an iris blend.
- Change the angle between both detectors from 90°

All three methods have been applied in this work. In the second version of the HBT, the crosstalk is eliminated, because both APDs are separated by two monochromators.

Dark Counts

As mentioned in section 3.2 every detector has a dark count rate R_{Dark} which leads to a difference between the measured h(t) and the $g^{(2)}(t)$ function of the studied photon source: A coincidence can be measured, when the start signal originates from a photon and the stop signal from a dark count (or vice verse). For one time channel the number of such coincidences during a measurement time t_{meas} is given by:

$$Coincidence_{dark} = R_{dark}(R_{D1} + R_{D2})t_{wind}t_{meas}/N_{channels}\,, \quad (3.5)$$

where $N_{channels}$ is the number of channels in the histogram. The dark counts lead to an increased h(t) value and therefore to a $g^{(2)}(0) > 0$ value even for a perfect single photon emitter. If necessary the dark counts can be removed by subtracting the result of equation 3.5 from all channels in the histogram before normalizing the histogram.

Limited Time Resolution

As mentioned in section 2.2 on page 14 the probability that a second photon will be emitted by the QD after the first is given by: $p(t) = \exp(-t\ r)$, for $t > 0$, where r is the emission rate of the QD. This results in a discontinuity at $t = 0$, but due to the limited time resolution of the detectors and the counting electronic it is impossible to measure this discontinuity exactly. The limited time resolution yields to an increased $g^{(2)}(0)$ value for a fast single photon

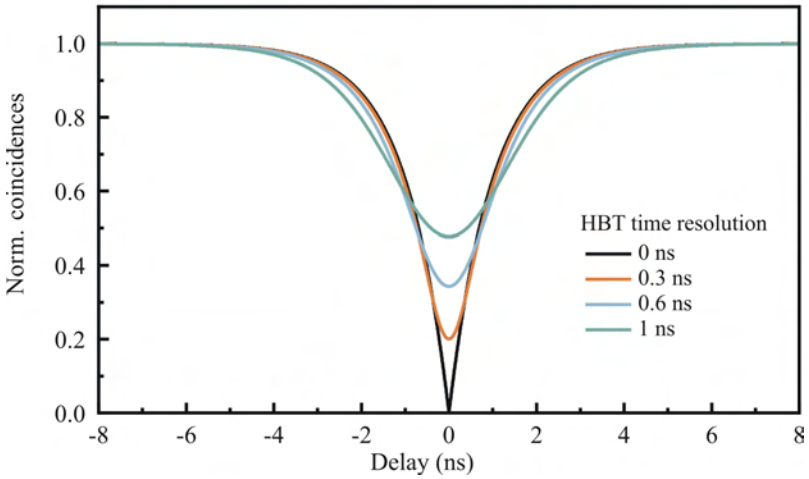

Figure 3.7: Simulation of the measured photon correlation function $g^{(2)}(t)$ in dependence on the time resolution of the Hanbury-Brown Twiss setup. The true $g^{(2)}(0)$ value was g_0=0 and the photon lifetime 1 ns. An increased time resolution leads to an increased measured $g^{(2)}(0)$ value.

source: Two photons with a small time distance may be detected as if they are at the same time.

Mathematically for $t>0$ and $w>0$ the measured histogram is given by p_{meas} convoluted with a Gaussian:

$$\begin{aligned} p_{meas}(t) &= p(t) \otimes \mathrm{Gaussian}(t) && (3.6)\\ &= \int_0^\infty e^{(-t'r)} \mathrm{Gaussian}(t-t')dt' && (3.7)\\ &= \frac{w^2}{2} e^{\frac{-2rt+w^2}{2\tau^2})} \left[1 - \mathrm{Erf}\left(\frac{1}{\sqrt{2}}(\frac{t}{w} - \frac{w}{r})\right)\right], && (3.8) \end{aligned}$$

where $\mathrm{Erf}()$ is the error function and $w>0$ the width of the Gaussian, representing the time resoltion.

3.3.4 *Analysis of $g^{(2)}$-Measurements*

In order to extract the real $g^{(2)}$-function from the measured histogram h(t) first a number (usually 10) of channels are binned and the histogram is normalized.

As far as negative and positive delay times are recorded the $g^{(2)}(t)$ for a two level system can be written as:

$$\begin{aligned} g^{(2)}(t) &= H(-t)g^{(2)}(-t) + H(t)g^{(2)}(t) && (3.9)\\ &= 1 - (H(-t)e^{t/\tau} + H(t)e^{-t/\tau}), && (3.10) \end{aligned}$$

where H(t) is the unit step function.

Taking into account the limited time resolution from equation 3.8 and possible background luminescence or a non-perfect single photon the measured histogram can be written as:

$$h(t) = 1 - \frac{1}{2}(1 - g_0)\left[e^{\frac{2rt+w^2}{2\tau^2}}\left(1 - \mathrm{Erf}\left(\frac{1}{\sqrt{2}}(\frac{-t}{w} - \frac{w}{r})\right)\right) + \ldots \right.$$
$$\left. \ldots + e^{\frac{-2rt+w^2}{2\tau^2}}\left(1 - \mathrm{Erf}\left(\frac{1}{\sqrt{2}}(\frac{t}{w} - \frac{w}{r})\right)\right)\right] \quad (3.11)$$

Here g_0 is the true $g^{(2)}(0)$ value deconvoluted from the time resolution but still including any possible background luminescence.

To illustrate the difference between h(t) and $g^{(2)}(t)$, figure 3.7 shows a simulation of the measured h(t) function based on equation 3.11 for different time resolution of the setup. The parameter for the real $g^{(2)}$-function was chosen as $g_0 = 0$ with an exciton lifetime $\tau = 1\,\mathrm{ns}$ or $r = 10\,\mathrm{s}^{-1}$. Only for a perfect time resolution of 0 ns (black line) the true $g^{(2)}$-function can be measured. Even with a time resolution of 30 % of the photon lifetime (0.3 ns, orange line), the dip is broadened and more important the $g^{(2)}(0)$ value is increased. For the HBT equipped with APDs (time resolution 0.6 ns blue line) the measured $g^{(2)}(0)$ value is limited to be > 0.34.

In order to obtain the true $g^{(2)}(0)$ value all measured correlation functions in this work were fitted with equation 3.8. But no background luminescence has been subtracted.

To analyze the correlation measurement under pulsed excitation equation 3.11 has to be multiplied with a train of pulses.

3.4 SAMPLE STRUCTURE

In this section the samples used in this work, will be described in detail. The first four sections describe different steps of development of a highly efficient single photon source: From a simple pin-diode, via a single QD LED with self-organized and site controlled QDs to a resonant cavity LED. In these sections not only the growth design, but also the major processing steps will be addressed. The last section describes the growth structure of QDs grown on 111 GaAs substrate. These structures are to study a new type of QDs and consist of a simple PL structure.

3.4.1 *A Poor Man's Single QD LED*

In this structure the QDs are embedded in pin diode and a single QD can be electrically pumped by applying a bias well below the flatband condition [Turo6]. The sample structure and the resulting band diagram for a bias U below the flat band condition, i.e. for $U < 1.5\,\mathrm{V}$, are schematically shown in the Figure 3.8.

The p-i-n diodes were grown by molecular beam epitaxy on a p^+ GaAs substrate, which forms the bottom electrical contact of the diode. The layer

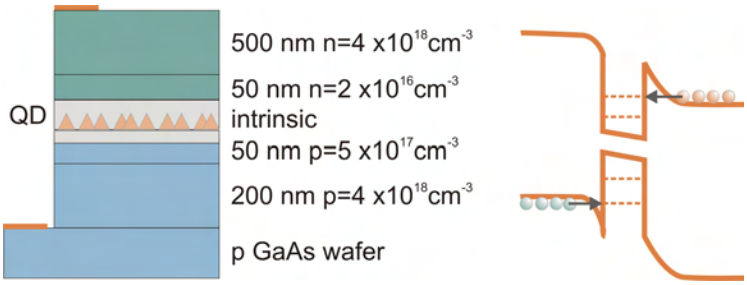

Figure 3.8: Schematic growth structure (left) for the simplest QD-LED device. Right: Resulting band diagram for an applied bias below the flatband condition.

structure in order of growth on the substrate is as follows: 200 nm and 50 nm p-doped GaAs layer with p = 4 $\times 10^{18}$ cm^{-3} and p = 5$\times 10^{-17}$ cm^{-3}, respectively; a 6 nm intrinsic GaAs spacer layer; a depositon of 1.8 monolayer (ML) of InAs, which gives rise to a wetting layer (WL) and QDs with a density of about 10^{10} cm^{-2}. The QD layer is covered by 16 nm of intrinsic GaAs followed by 50 nm n-doped GaAs (n = 2$\times 10^{16}$ cm^{-3}) and a 500 nm GaAs top layer with n = 4$\times 10^{18}$ cm^{-3}. The diodes are defined by wet-chemical etching and a ring-shaped gold electrode forms the top electrical contact and provides optical access. In this work large area devices with 200 µm diameter, containing $\approx 10^6$ QDs, have been investigated.

3.4.2 *Single QD Light Emitting Diodes*

The electrical pumping of a single QD is the aim of this sample series. For this aim a QD layer with low spatial density is embedded in a pin junction and the current is constricted by an AlO_X aperture. The schematic sample structure is shown in figure 3.9. The minimum stable oxide aperture diameter is around 1 µm and in order to pump only one single QD the spatial QD density has to be in the lower 10^8 cm^{-2} range.

Two different sample types have been studied, which are varying only in the QD layer: The NP127X series was grown by MOCVD and the low density was achieved by switching of the wafer rotation during the QD layer growth. In the Now168x series the QD layer was grown with an extremely low growth rate by MBE. The processing for both sample series was the same. In a third approach nominally one single QD was grown using a patterned substrate and the diodes were fabricated around this single QD.

MOCVD grown sample series NP127x

The spatial density of self-organized QDs strongly depends on the deposited amount of InAs. Above the critical thickness of 1.5 mono layers (ML) the spatial QD density increases by about one order of magnitude when nominally 0.2 ML more InAs is deposited [Leo94]. In MOCVD the typical growth rate is about 0.3 ML/s, hence in order to achieve low spatial QD density the growth time for the QD layer has to be controlled within less than a second. In a first attempt to achieve the required low QD density

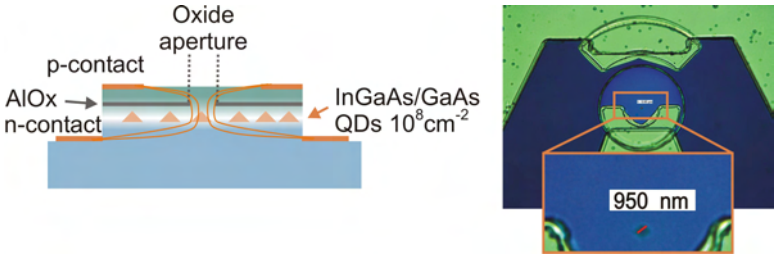

Figure 3.9: left: Schematic sample design for the single QD LED. The current is constricted by the oxide aperture. Right: Microscope image of the device from the sample Now1689. The p-top and n-back contacts are visible as green areas. The oxide aperture is visible in the center of the diode and has a diameter of 950 nm.

the wafer rotation has been switched of during the growth of the QD layer leading to an inhomogeneous deposition of InAs along the wafer. On a small part of the wafer ($\approx$10 mm^2) the QD density was sufficient low. The device processing was the same as described in the next section.

MBE grown sample series Now168x

The pin-structure consists of an undoped GaAs layer with a low density layer of InAs QDs, a 60 nm thick aperture layer of high aluminum content AlGaAs, and p- and n-type GaAs electrical contact layers. To reduce the influence of current spreading, the distance between the AlGaAs aperture layer and the InAs QDs layer is minimized to only 20 nm. The structures were grown by a Riber-32P MBE system on semi insulating (100) epi-ready GaAs substrates. The low density (~10^8 cm^{-2}) InAs QD layers were grown in the Stranski-Krastanow mode with deposition of 1.8 ML of InAs. The growth rate were kept at ~0.04 ML/s with an As/In ratio of 50. All layers were grown at T=580°C, except the QD layer which was grown at T=510°C.

Cylindrical mesas were processed by inductively coupled plasma reactive ion etching, using chlorine based recipes. The sub-micron size oxide current apertures were created by selective oxidation of the high aluminum content aperture AlGaAs layers. Tapered oxide current apertures were used to enhance the stability of the oxide structure and to improve the injection characteristics of the QD-LED. The oxidation was performed in a H_2O – N_2 environment at T = 420°C using optimum conditions as already developed for vertical cavity surface emitting laser (VCSEL) [Hai02]. After the selective oxidation, Si_3N_4 deposition was performed, followed by Au/Pt/Ti and Au/Au-Ge/Ni metallization to form p- and n-contacts, respectively.

In order to achieve devices with sub-micron apertures, arrays of 28 mesas with diameter from 20-50 µm were processed. The oxidation process was stopped after the moment the aperture in the smallest mesa was closed.

Site controlled QDs

In both samples described above the QDs were grown by self-organization in the Stranski Krastanow mode (see section 2.3.1) and only by chance a

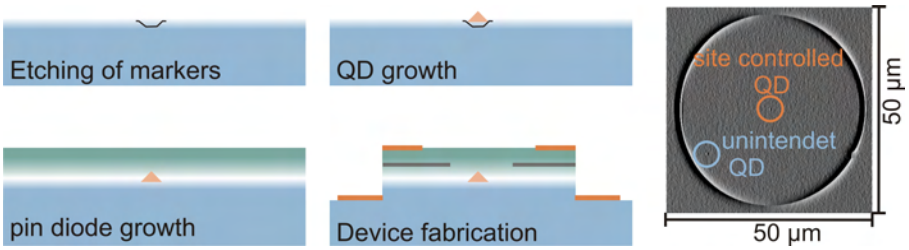

Figure 3.10: Left: Preparing the sample structures of the single QD-LED with site controlled QDs. Right: AFM image directly after the QD growth.

single QD is located beneath the oxide aperture. To bypass this random distribution samples with site-controlled QDs were grown.

The samples were grown in a MBE machine with an interruption for the markers: On top of an n-type substrate a 500 nm n-doped GaAs buffer layer was grown. The samples were patterned using e-beam lithography and wet chemical etching. The markers consist of 18-20 nm deep holes, which are acting as a seed for the QD growth [Atko8]. Besides the holes for the QDs, circles for the mesa processing were etched. Before the growth was continued, the sample surface was cleaned from the oxide layer. Different samples with nominally 1.2 -1.4 monolayers of InAs were grown at 500 °C and capped with 17 nm of GaAs. Afterwards the sample was annealed at 560 °C and another 20 nm undoped GaAs were grown. The samples were finished with the $Al_{0.9}Ga_{0.1}As$ layer for oxidation and a p-doped top contact. Figure 3.10 shows the different steps schematically.

The markers had the same pattern as the lithography mask and were still visible after the second growth step. Therefore they could be used to process diode structures, with the seed hole for the QDs in the center of the mesa. Figure 3.10 right shows an AFM image of the sample with uncapped QDs. Beside the site-controlled QD in the center of the circle only one unintended dot is visible in an area of 50 x 50 µm. The diode structure contains nominally only one QD, hence the oxide aperture must not constrict the current to a small area. Consequently, the oxidation process was stopped earlier, resulting in aperture diameters of about 10 µm.

3.4.3 *Resonant Cavity LEDs*

For increasing the out-coupling efficiency a resonant cavity light emitting diode (RCLED) has been realized. Figure 3.11 left shows a schematic diagram of the RCLED. This devices include a $3/2\lambda$ micro-cavity formed by 4/12 distributed bragg mirrors above respectively below the QD layer. The other parts of the device are similar to the one in the previous chapter: A layer of low density QDs ($\approx 4 \times 10^8\,cm^{-2}$), a pin junction for electrical pumping and an oxide aperture for current constriction. For these devices a special chip carrier (see figure 3.11right) has been developed. The chip carrier allows contacting up to five devices, while one of them can be contacted to a high bandwidth connector (SMC).

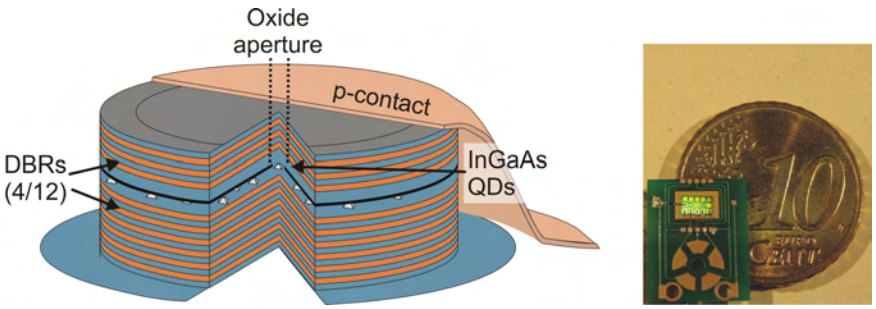

Figure 3.11: Left: Schematic diagram of the RCLED structure. Right: Array of 10 devices on specially designed chip carrier.

The device was grown by MBE on n-doped (100) GaAs substrates. After a n-doped buffer layer 12 pairs of a GaAs/$Al_{0.9}Ga_{0.1}As$ DBR mirrors were grown, followed by a n-doped 114 nm $Al_{0.2}Ga_{0.8}As$ barrier. The QD layer was grown on 23 nm undoped GaAs, with an InAs growth rate of 0.015ML/s and an In/As ratio of 1:50. After capping with 23 nm undoped GaAs another 102 nm thick $Al_{0.2}Ga_{0.8}As$ barrier was grown, followed by the tapered AlAs layer for oxidation. The micro-cavity was closed by 4 pairs of GaAs/$Al_{0.9}Ga_{0.1}As$ DBR mirrors.

In this sample series arrays of 10 devices with a diameter ranging from 34 to 43 µm has been processed with the same technique as for the single QD LED described in section 3.4.2.

3.4.4 *QDs Grown on (111) GaAs*

The samples were grown by molecular beam epitaxy on a GaAs (111) substrates having a miscut of 2° in the $[2\bar{1}\bar{1}]$ direction, using a Riber32P system. On a 500 nm buffer layer a 50 nm $Al_{0.6}Ga_{0.4}As$ layer followed by 65 nm GaAs were deposited at 580° C . The QDs were grown using the droplet technique [Chi90]: The substrate temperature was reduced to 510°C with closed As shutter. Nominally 1.5 ML of Ga was deposited to saturate the excess surface As atoms and ~2 ML of In was deposited without As flux, forming In droplets. The formation of InAs QDs took place under As flux with closed In shutter and the rotation of the sample was switched off. The QD layer was capped with 65 nm GaAs followed by a second $Al_{0.6}Ga_{0.4}As$ layer and a final 10 nm GaAs layer. The two AlGaAs layers prevent carrier diffusion from the QD layer to the bulk material. All layers are nominally undoped. Figure 3.12 shows a schematic diagram of the growth structure.

Atomic force images of uncapped QD layers show triangular shaped structures with a base length in the order of 100 nm, while QD-sized structures could not be observed in these measurements. In cross section transmission electron microscopy (TEM) on the sample the QD layer and a large number of screw dislocation starting from this layer was observed [Alb10b]. In plan view TEM also triangular shaped structures were visible. These structures are probably the top of the screw dislocation and not related to the QDs. The fail of any structure analysis can be assigned to

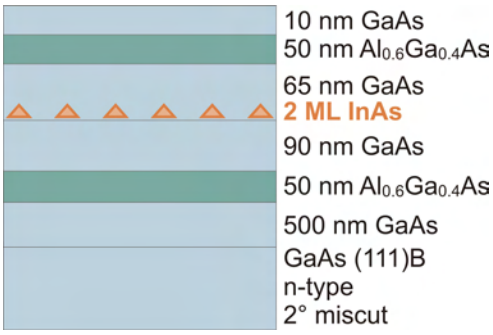

Figure 3.12: Growth structure for the QD on 111 GaAs. The AlGaAs layer are to prevent carrier diffusion and hence to increase the PL signal.

the growth process. The wafer rotation was switched off during the QD grow, resulting in an inhomogenous QD density along the wafer. Hence in micro-PL measurements (see chapter 6) only a very small part of the wafer shows QD luminescence.

Part III

RESULTS

4

SINGLE PHOTON SOURCES

This chapter describes three significant development steps towards a high efficient ultra-fast single photon source. The first section 4.1 reports, how a simple pin diode structure can be used to pump a single QD electrically, by applying a bias well below the flatband condition. Resonant tunneling of electrons and holes can be observed in this device by optical means.

In order to increase the maximum pump rate the current has to be constricted more effectively to pump only a single QD. This is realized by an AlO_x aperture above the QD layer. Two of such devices, grown by different techniques, will be described in section 4.2. The second device grown by MBE demonstrates devices with a record pure spectra and clear single photon emission.

Finally section 4.3 presents the realization of a resonant cavity LED. This device allows perfect single photon emission at pumping rates of up to 1 GHz. Since the optical response of this device is too fast for APDs new superconducting detectors have been used in photon correlation measurements. These measurements justify the analysis of the $g^{(2)}$-function presented in section 3.3.4.

4.1 A POOR MANS SINGLE PHOTON SOURCE

The first step in the development of a compact single photon device is to pump a QD electrically. This section describes the simplest device consisting of a pin diode with a diameter of 200 µm and without any intended current constriction. The detailed sample structure can be found in section 3.4.1. Although the device contains approximately 10^6 QDs, it is possible to observe electroluminescence from a single QD by reducing the applied bias well below the flatband condition. This section gives a detailed analysis of the microscopic origin of this effect, by presenting micro-electroluminescence measurements.

The first evidence that only a single QD is pumped can be found in macro EL measurements, where the luminescence from the entire diode is detected. The upper left panel of 4.1 shows a color-scale plot of the normalized EL intensity versus the applied bias and the photon energy (taken from [Bau10]) at 15 K. Upon decreasing bias the QD emission clearly narrows and two distinct EL features appear. They are labeled with A and B and indicated by dashed lines in figure 4.1. A and B both shift to lower energies with decreasing bias and their peak energies run parallel to the line $eU = h\nu$. The energy difference between the excitation energies eU, given by the applied bias and the peak energies of each feature is $E_A = 160$ meV and $E_B = 100$ meV, respectively. This indicates that electron-hole pairs electrically injected into different QDs relax by approximately the same energy difference prior to

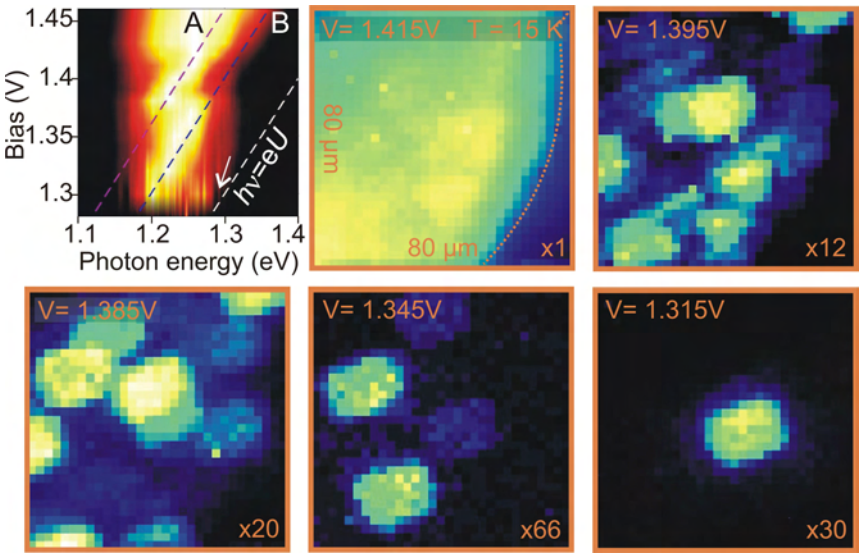

Figure 4.1: Upper left: Color scale image of the normalized macro EL intensity as a function of photon energy and bias. Others: Maps of the maximum surface EL intensity for a range of applied bias. For a given bias the EL spectrum is recorded for a grid of positions. The images show the maximum intensity of each spectrum as a function of the position on the diode. The number at the bottom right of each image denotes the factor by which the EL intensity is scaled compared to the first image.

the radiative recombination in the ground state. This also indicates, that the electric field at the QD position decreases parallel to the applied bias with a lever arm (see 2.3.4) of ≈1.

For a bias below 1.35 V the spectral homogeneous EL splits into a number of sharp luminescence lines. This splitting mainly follows the trend of line B. Finally at 1.28 V a single luminescence line remains.

4.1.1 *Spatial Fragmentation of the Luminescence*

The fragmentation of the EL spectrum into sharp lines is accompanied by a spatial fragmentation of the EL emission. To study this effect, micro EL measurements were performed.

Figure 4.1 shows the spatial distribution of the luminescence for a series of bias voltages. The color scale indicates the maximum intensity in a spectral range between 1.25 and 1.29 eV. For each image, a scale factor relates the maximum of the color scale to the maximum at U = 1.415 V. The edge of the diode is marked in the first picture by a dashed line. At U = 1.415 V the emission is essentially homogeneous across the whole diode. For a slightly lower bias (U = 1.395 V) the diode emission starts to break up into a series of bright spots dominating over a homogeneous background emission. At U = 1.385 V the background intensity weakens and several bright spots emerge at distinct positions with a uniform spot size given by the spatial detection resolution. Further lowering the bias to U = 1.345 V results in a decrease of the maximum intensities and the number of visible emission spots is

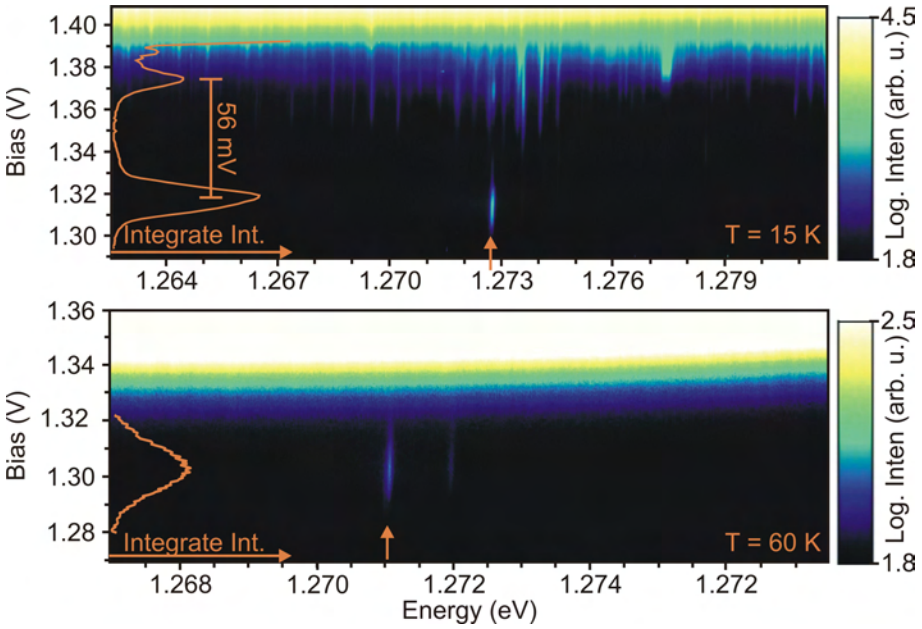

Figure 4.2: EL spectra in dependence of applied bias at 15 K (top) and 60 K (bottom). The intensity is logarithmic color scaled. The orange line indicates the integrated intensity of the luminescence peak that is marked by an arrow.

reduced to four. Finally at U = 1.315 V, only one bright spot is visible and the corresponding spectrum (see figure 4.3 left) consists of a single sharp emission line. Surprisingly the intensity of this emission line is even higher than for 1.345 V. No other EL lines could be observed at this bias, suggesting that this emission center originates from a single QD.

4.1.2 *Resonant Tunneling Excitation*

In order to analyze the pumping mechanism of this single QD, the EL was measured in dependence of the applied bias . In contrast to the upper left part in figure 4.1 in these measurements only the luminescence from the remaining bright spot at a bias of 1.315 V was detected, with a spatial resolution of about 20 µm.

Figure 4.2 top shows a series of EL spectra in a logarithmic color scale for different applied bias, measured at a temperature of 15 K. For a bias between 1.28 and 1.33 V a sharp emission line at an energy of 1.2727 is visible. This line has the same energy as the one which remains at the lowest voltage in the macro-EL measurements in figure 4.1. In the micro-EL measurements the single line is accompanied by a second sharp luminescence line at 1.2735 eV the same bias dependence and an 80 times lower intensity. No other EL is visible, even in a larger spectral range, which again suggests that only one QD is pumped in the entire diode. A single spectrum at a bias of 1.315 V is shown in figure 4.3a) in a semi logarithmic plot. The broadening of the single luminescence line is due to acoustic phonon scattering and is discussed in detail in chapter 5.

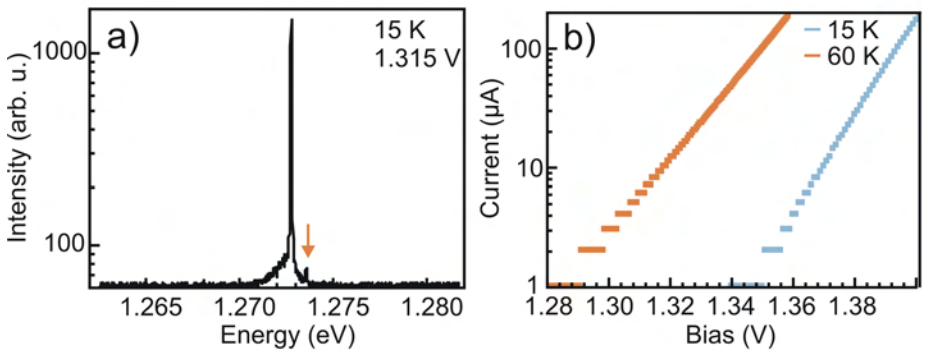

Figure 4.3: a) EL spectrum of a single QD at 1.315 V and 15 K, exhibiting one pronounced and one weak sharp luminescence line b.) IV curve of the diode for two different temperatures. For higher temperature the current starts to increases at lower bias. The steps are due to the limited current resolution of 1 µA.

The integrated intensity of the single EL line in dependence of the bias (orange line in figure 4.2) exhibits sharp peaks at voltages of U = 1.315 V and U = 1.371 V. These resonances are a clear manifestation of the voltage-tunable resonant tunneling excitation of a single QD detected by optical means. The resonant injection of carriers from the doped contact layers into discrete excited states of the QD is followed by energy relaxation of the carriers into the ground state and radiative recombination. As mentioned above the lever arm in this device is almost one and therefore the applied bias can directly be translated into energy. The two bias resonances are separated by $\approx$ 56 meV and have energy difference from the ground state energy (given by the luminescence energy) of 42 meV and 98 meV. Similar resonances were found in the EL of other QDs, though the number of observed resonances and their amplitudes can differ for different lines.

At large bias (U > 1.39 V) the strong growth of the EL intensity arises from an increasing contribution of the emission from the QD ensemble, as the flat band condition is approached.

The lower part of figure 4.2 shows the bias dependence of the EL at the same position on the diode at 60 K. Note the higher resolution of the energy and bias scale in comparison to the 15 K measurement. For bias below 1.32 V again only two sharp luminescence lines are visible. Here the intensity of the brighter line has dropped by a factor of 250, whereas the intensity of the second line stays almost constant, resulting in an intensity ratio of about 1:3.

The maximum of the bias resonance (orange line) is shifted to a lower voltage of 1.30 V and the QD ensemble luminescence begins to dominate already at 1.33 V. Consequently the second bias resonance of the single line is no longer visible. For higher temperatures the QD luminescence starts at lower bias and the single line cannot be observed.

The same behavior as from the QD ensemble luminescence is visible in the IV characteristics, measured on the entire diode, (figure 4.3b). In the semi logarithmic plot the current increases linearly with a slope of 41 and 31 for 15 K and 60 K respectively. Hence the current is still limited by the

built-in voltage of the pin-junction rather than by ohmic contacts and cables [Sze98]. The built-in voltage decreases with increasing temperature [Sze98], consequently the current starts at 15 K at higher bias than at 60 K. The QD ensemble luminescence strongly depends on current density and therefore starts at lower bias for higher temperatures.

Turning back to the resonant excitation of the single QD: In figure 4.2 the resonances exhibit a FWHM of 12 mV and 19 mV for 15 K and 60 K respectively. This is significantly larger than the width of the observed individual QD EL line (<150 µeV), suggesting that the resonant condition is broadened. The electrons and holes in the doped n- and p-type layers of the diode have an energy spread given by the respective Fermi energies. The width of the Fermi-distribution can be estimated by ≈4 kT, resulting in an energy variation of the charge carriers of about 5 meV and 20 meV for 15 K and 60 K respectively.

In conclusion a single QD is pumped by resonant tunneling of electrons and holes at low bias from the reservoir in the n- and p-type layers of the diode into excited states in the QD..

4.1.3 *Further Selecting Mechanism*

Though the number of active QDs is constrained by the conditions of resonant tunneling, this constraint is not sufficient to explain the pronounced spectral and spatial fragmentation of the EL emission in this simple LED. Existing theoretical models [Kie03] do not predict the degree of spectral or spatial fragmentation either. The high density and uniform distribution of QDs ensures that even at the lowest bias several dots could be active. Hence some QDs are probably coupled more strongly to the reservoirs than others. This assumption is supported by two other effects:

First, for different QDs different numbers of resonances were detected. Second the emission energy in figure 4.2 decreases for increasing bias. This can be attributed to the quantum-confined Stark effect in the QD (see section 2.3.4), because an increased bias results in a decreased electric field. Since several luminescence lines demonstrate different dependencies on the bias, the effective electric field in the QDs differ. Of particular interest is that the energies of the single EL lines remain constant for the second bias resonance between 1.36 V and 1.38 V, suggesting that the electric field at the position of this particular QD remains constant.

This behavior could be explained by preferential tunneling paths, which may arise from mesoscopic fluctuations of the n- and p-doped interfaces due to randomly placed doping atoms in or close to the intrinsic region, from crystal defects or from strain-related potential minimal associated with the QDs themselves. Such variations would not only explain the differences in the bias dependence of the Stark shifts among various QDs, but could also account for the spatial and spectral fragmentation of the EL spectra.

A similar effect has been studied previously in cathodoluminescence [Chr03]and micro-EL maps of the emission from the ridge-waveguide regions of InGaN quantum well based LEDs. Spatial inhomogeneities have

been observed due to non-uniform carrier injection caused by crystal degradation [Ros08].

In summary, this section demonstrates how the continuously broad band emission of a large quantum dot ensemble fragments into spatially strongly separated sharp emission lines from individual quantum dots. This effect can be explained in terms of the selective excitation of a small number of QDs within the ensemble due to the presence of preferential resonant tunneling paths for carriers. The bias dependent measurements demonstrate the concurrent resonant tunneling of separated electron and holes into the bounded exciton state in the QD. Unfortunately the pumping rate of charge carriers by resonant tunneling is very low. Hence the photon rate out of the device is too low for application of this single QD device. In order to increase the maximum pumping rate, the current has to be constricted to only one QD by other methods. They will be presented in the following section.

4.2 SINGLE QD LIGHT EMITTING DIODES

This section describes three different attempts of controlled electrical pumping of a single QD in a pin diode. In all devices the current is constricted by an AlO_x aperture located above the QD layer, as described in section 3.4.1 on page 50. In the first attempt the samples were grown by MOCVD and only a small number of devices demonstrate the luminescence from only a few or even a single QD. In the second attempt, grown by MBE, one device shows a spectrum with a record clarity of only one single luminescence line over a spectral range of more than 500 nm. Photon correlation measurements on this device prove single photon emission from an electrically pumped single QD.

In the third attempt in section 4.2.3 site-controlled QDs were embedded in the pin junction. The devices with a current aperture diameter of about 10 µm demonstrate electroluminescence from only a few QDs.

4.2.1 *First Attempt: MOCVD Grown Devices*

The first devices, containing an oxide aperture, were grown in MOCVD. The required low QD density of about $10^8 cm^{-2}$ was achieved on a very small part of the wafer, by switching of the wafer rotation during the QD growth. Unfortunately after the processing only two devices of this part shows diode-like IV curves and were studied in detail in micro-EL measurements at low temperatures.

In a first step the location of the electroluminescence was identified by taking pictures of the sample surface with a simple CCD camera under applied bias. The results indicate that the current constriction by the oxide aperture did not work as planned in this sample: At a current of 15 µA (for 3.8 V) two luminescence spots were visible. The left part of figure 4.4 shows the EL spectra of these positions at 15 K and their locations on the device are marked by a cross in the inset. Both positions exhibit a few sharp

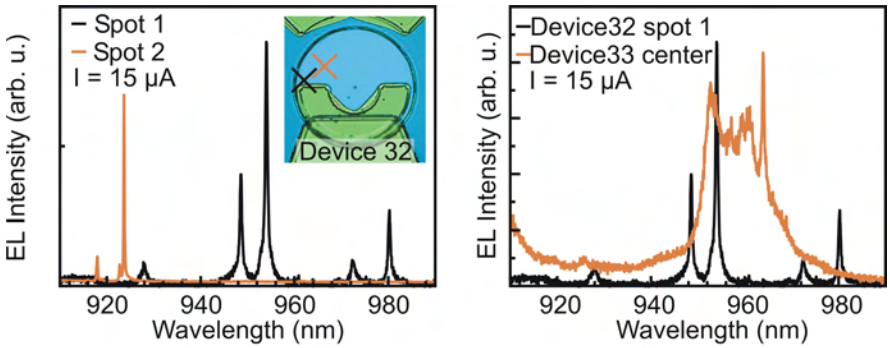

Figure 4.4: Left: EL of two different spots on the diode, marked in the inset by a cross. From the center no EL was observable. Right: Comparison of the EL from two devices with an oxide aperture diameter varying nominally by 1 µm.

luminescence lines, as expected from a single or a few QDs. Unfortunately both positions are not in the center of the device, were the aperture was expected. From the center no EL was visible at this current. This is in contrast to a second device (No. 33) where EL from the center was visible. Both devices are separated by only 200 µm on the wafer, thus the spatial QD density should be comparable. The right panel of figure 4.4 shows the EL spectra of both devices at the same current of 15 µA. The luminescence from the center of diode 33 is broad and comparable to the luminescence from a number of QDs rather than a single QD as for device 32.

Another observation indicates that some problems with the current constriction exist: The mesa of device 33 has a 1 µm smaller diameter than for device 32. Consequently the oxide aperture diameter of device 33 should be smaller than for 32. Hence in device 32 a smaller number of QDs should be pumped, which does not match to the EL results shown in the right panel of figure 4.4.

A third indicator is the current-voltage characteristic: The applied bias of 3.8 V is far above the flatband conditions of a GaAs pin-junction (section 2.3.4) and the current should be limited mainly by the contact and cables. Nevertheless the current is still increasing non-linearly. Hence a large part of the applied bias drops not in the GaAs-pin-junction but in some other parts of the devices.

The device characteristics can be explained by a complete oxidation of the AlGaAs layer, rather than the creation of a current aperture. The AlO_x is a barrier of 300 meV and 500 meV for the electrons and holes respectively. The oxide layer and thereby the barrier can be perforated either by dislocations in the grown layers or metal pollution during the oxidation process. Both would result in small localized current paths, similar to the situation described in the previous section 4.1. These current paths can be understood as "self-organized" current apertures.

In contrast to the devices in the previous section 4.1, no resonant tunneling effects were observed in bias dependent EL measurements. But the QDs

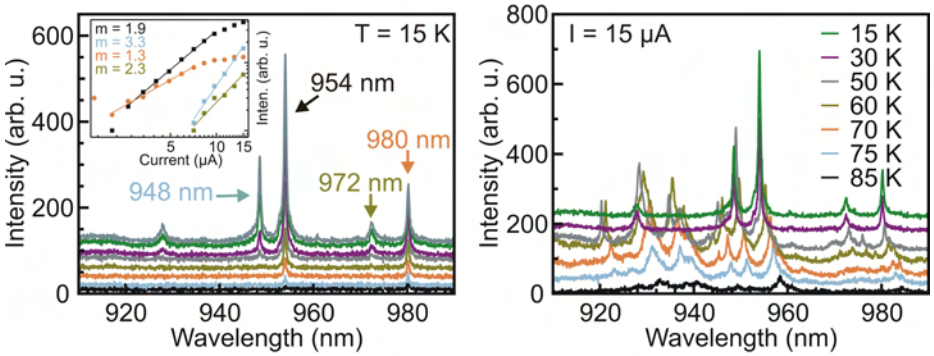

Figure 4.5: Left: Current dependence of the EL from 1-15 µA. The inset shows the integrated intensity of the luminescence in dependence on the current in a double logarithmic plot and the corresponding slope of a linear fit. Right: Temperature dependence of the EL at a fixed current of 15 µA. For clarity an offset was added for each spectrum in both panels.

could be pumped with a current sufficient to saturate the excitonic emission. Figure 4.5 shows a series of EL spectra from spot 1 for a current increasing from 1 µA to 15 µA, separated by an offset for clarity. For a current of 2 µA (2.7 V, blue line) only two weak emission lines at 954 and 980 nm are visible. With increasing current the QD is pumped with more charge carriers. Consequently the luminescence intensity increases and further emission lines appear. According to their energetic position and their appearance at higher current the lines at 948 and 972 nm can be assigned to biexciton recombination. The inset of figure 4.5 presents the integrated intensity of these four emission lines in dependence of the current in a logarithmic plot. For a current as high as 15 µA (3.8 V) only five sharp luminescence lines are visible, indicating that only two or three QDs are electrically pumped. The intensity of the emission line at 954 nm begins to saturate at this current. Hence the pumping rate of the charge carrier is in the order of the reciprocal exciton life time. These results confirm the concept to pump a single QD as strong as possible without pumping other QDs.

The plotted value for m in figure 4.5 represents the slope of an apparent linear fit to the intensity dependence. Surprisingly the slopes of both emission lines, which appear first for increasing bias, is higher than 1, as expected for the linear power dependence of the exciton emission [Gru97]. The slope of the possible biexciton emission is also larger than the expected value 2. This could be explained as following: With increasing current the number of charge carriers around the QDs increases non linearly. Some parts of the currents flows along other parts of the device and not through the QDs. According to the current dependence the QD emitting around 980 nm reaches a higher number of charge carriers than the other QD.

.

The right part of figure 4.5 shows a series of spectra for different temperatures at a pumping current of 15 µA. For better visibility an offset was added. For higher temperatures the emission shifts to longer wavelengths,

as expected from the Varshni-shift [Hei99a]. Starting at 50 K additional emission lines appear and the emission lines becomes broader, due to phonon scattering (chapter 5). However for temperatures up to 75 K the main luminescence line at 954 nm is spectrally well separated from other emission lines, making this device concept promising for a single photon emitter up to liquid nitrogen temperature.

Unfortunately after a few days of measurement the device showed no diode-like IV curve and no further EL measurements could be performed. One explanation for the broken device might be the following: During the oxidation process the lattice constant in the AlGaAs layer changes by 7 %, resulting in a large strain. The cooling of the sample from room temperature to 15 K introduces additional strain: The lattice constants from the different layers do not have the exact same temperature dependence. Furthermore a temperature gradient within the device structure may appear. To increase the endurance of further device generations the following samples were cooled down to 15 K slowly within 1.5 hours, rather than 10 minutes as would be possible for this kind of cryostat.

In conclusion the MOCVD grown sample, presented in this section, is the realization of a single electrically pumped QD with a current constriction by an AlO_x layer. Although the current aperture is probably "self-organized" the device demonstrates single QD luminescence even at higher pumping current, sufficient to saturate the excitonic emission. Sharp luminescence lines up to 75 K were observable, making this device concept a promising approach towards an efficient single photon source.

4.2.2 *Electrically Pumped Single Photon Sources*

The second generation of devices with an oxide current aperture was grown by MBE. Here the required low spatial QD density of about $10^8\,\mathrm{cm}^{-2}$ could be achieved over the entire 2 inch wafer. Consequently the device output was much higher.

Figure 4.6 demonstrates how efficiently the current is constricted by the oxide aperture to pump only one single QD, by comparing electroluminescence with photoluminescence spectra: Panel (a) of figure 4.6 shows a macro-photoluminescence spectrum at 10 K of the sample. The sample was excited with a frequency doubled Nd:YVO laser emitting at 532 nm and an excitation spot diameter of about 200 µm. Besides the very intense emission from the GaAs bulk material a broad emission from the QDs is visible around 925 nm. Hence a larger number of QDs are pumped and their sharp luminescence lines overlap to a broad emission.

The number of pumped QDs can be reduced with the custom built micro-photoluminescence set-up, having an excitation spot size of about 2 µm (panel (b) of figure 4.6). The broad QD emission around 925 nm decomposes into a few sharp lines. This is a typical spectrum from about 5 QDs, verifying the low spatial QD density. As in the macro-PL the luminescence from the GaAs bulk material and the wetting layer is dominant (for clarity only partly shown). For a single photon source this luminescence is very harmful. Even

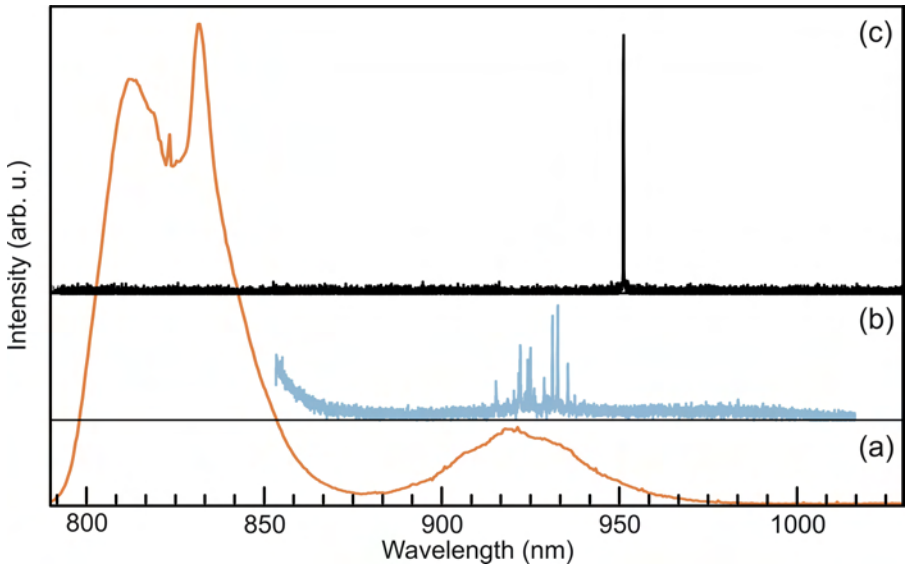

Figure 4.6: (a) Macro-photoluminescence with an excitation spot diameter of about 200 µm (b) Micro-photoluminescence with a laser spot size of 2 µm and (c) electroluminescence spectrum form a single QD at a current of 870 pA (1.65 V). All spectra are recorded at 10 K.

if only a single QD would be pumped, the GaAs luminescence must be completely suppressed to achieve single photon emission. Hence for an optical pumped single QD spectral filters with a high suppression ratio are required to get non-classical light emission.

Finally, figure 4.6c) shows the electroluminescence spectrum taken for a current of 870 pA at a bias voltage of 1.65 V. Only one single line is visible over a spectral range of 300 nm, even emission from the wetting layer or the GaAs bulk material is completely suppressed. Since no material in the device can generate luminescence at wavelengths < 790 nm this device demonstrates a record clean spectrum with only one single emission line over the entire sensitivity range of Si based detectors.

As the oxide aperture above the QD is transparent for near-infrared light, the absence of other light emission than from the exciton recombination clearly proofs the pumping of a single QD. Therefore, at an injection current of 870 pA, light is emitted due to funneling of a single hole and a single electron into a single quantum dot followed by subsequent radiative recombination. In this sense, the ultimate limit of a light emitting diode (LED) is realized. This is in contrast to previous single photon sources [Yua02, Ben05a], where many QDs are pumped and the emission from all QDs except one is blocked by a shadow mask.

For an assignment of the luminescence lines to the recombination of electron-hole states in the QD power- and polarization dependent measurements were performed. Figure 4.7 left shows seven spectra for increasing injection current. For clarity an offset is added. Up to a current of 1 nA (green line) only one single emission line is visible. The integrated intensity of this and a second luminescence line in dependence on the pumping power is plotted in the inset in logarithmic scales. An apparent linear fit results

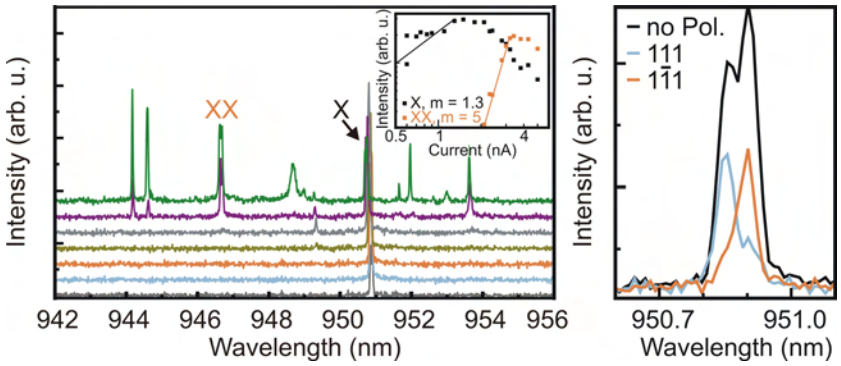

Figure 4.7: Left: Electroluminescence spectra at different current injection. For clarity, an offset is added to each spectrum. Right: High resolution spectrum of the exciton emission line at 0.9 nA. Polarization occurs along the [110] and [1$\bar{1}$0] crystal axes.

in a slope of 1.3, comparable (within the tolerance of error) to the expected value of 1 for excitonic emission.

Above a pumping current of 1 nA the exciton emission intensity saturates and two additional lines appear. The emission line at 947 nm exhibits very high power dependence, with a slope of 5. This line and the first at 951 nm demonstrate the same spectral jitter and therefore originate from the same QD [Töo].

For a further identification polarization dependent measurements with high spectral resolution were performed. The right panel of figure 4.7 shows the spectrum without polarizer (black line), which already demonstrates the doublet structure of the emission lines, consisting of two lines polarized in the [110] and [1$\bar{1}$0] direction of the crystal. This proves the recombination of an uncharged exciton and the resulting fine-structure splitting of 55 µeV is typical for InGaAs QDs at this emission wavelength [Seg05]. The emission line at 947 meV exhibits the opposite fine-structure splitting and hence originates from the uncharged biexciton recombination.

The third emission line between the exciton and biexciton emission (at 949 nm) is unpolarized and does not show any splitting. Therefore it can be assigned to the emission from a charged exciton [Edi07].

In this devices the injected current and thereby the intensity ratio of the exciton and biexciton can be adjusted at will. If for example the exciton and biexciton intensities become comparable, the ideal situation for the generation of cascaded photons is realized. The emission from uncharged dots in this device opens the way for the generation of entangled photon pairs on demand from a QD-LED by reducing the FSS to zero. This can be achieved for example by growing on (111) GaAs substrate (see chapter 6).

Another remarkable feature of this structure is the low current of 870 pA, sufficient to saturate the exciton emission intensity. This an improvement of two orders of magnitude as compared to the driving current in other QD based single photon sources [Yua02, Fio02, Zin04, Ben05b, Ell06]. When the exciton intensity saturates the generated photon rate is mainly limited by the exciton life time of about 1 ns [Tho01, Mic10, Feu08], since the capture time

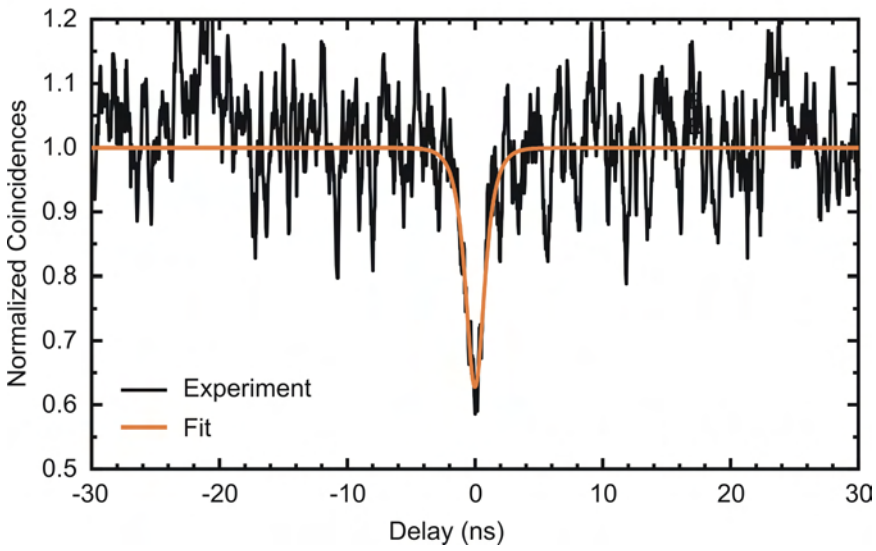

Figure 4.8: Photon correlation measurement under continuous wave current injection (0.9 nA, 1.65 V) at 10 K. No spectral filtering was used to isolate the luminescence from a single quantum dot. The orange line shows a fit function as described in the text.

of carriers is in the range of picoseconds. A current of 870 ps corresponds to ≈ 5 electrons/ns, resulting in an injection efficiency of about 20 %. This approximation is only valid if the electrons and holes relax into the exciton bright state. Since the electrons and holes from the contacts are not spin-controlled, the exciton dark state, having a lower energy (see section 2.3.3 on page 21) than the bright state, may also be filled. In this case the electron and hole can recombine only after a spin-flip or the QD will be filled to the biexciton level. Both results in a much lower photon rate of the exciton emission and thereby injection efficiency.

The extremely clean spectrum of the single QD-LED [Fig. 4.6(c)] allows to detect non-classical features of the emitted light without the need for additional spectral filtering.

The normalized photon correlation function under continuous-wave current injection of 0.9 nA is shown in figure 4.8. In contrast to previously reported single photon devices, for this measurement no spectral filtering on the way from the sample to the detectors was used. Only in order to avoid cross-talk between both detectors (see section 3.3.3) a band pass filter (FWHM=10 nm) with a central wavelength of 953 nm was placed in front of one detector. The measured photon correlation function shows a clear antibunching dip down to 0.6 at zero time delay. The orange line in figure 4.8 shows a fit, according to equation 3.11 as described in section 3.3.4 on page 49. Taking into account the limited time resolution (FWHM = 700 ps) the $g^{(2)}(0)$ value is 0.3, thus proving the non-classical light emission.

Considering the absent spectral filtering the antibunching dip is surprisingly low: First, it demonstrates that any disturbing luminescence integrated over the entire wavelength range from 500-1050 nm is much lower than from the sharp luminescence line from the QD. This again proofs the efficient

pumping of a single QD. Secondly, even emission from the same QD may increase the $g^{(2)}(0)$ value: Although the biexciton emission at this current is highly suppressed, the biexciton emission is *correlated* to the exciton emission. In cross-correlation measurements this results in an asymmetric photon correlation function (see section 3.3.2 on page 45). In measurements without spectral filtering the probability to detect a biexciton directly before or after (depending on which detector the biexciton is detected) the exciton is increased. Consequently the $g^{(2)}(0)$ value is increased. In fact simulations with rate equations [Aico5] predict a $g^{(2)}(0)=1$ for almost every pumping power, if the exciton and biexciton emission is detected without spectral selection [Kin10].

In summary, the reported measurements characterize this single QD LEDs with sub-micron-size aperture as highly efficient light sources that allow the controlled injection of a single electron and a single hole into a single quantum dot. Uncharged exciton and biexciton emission can be extracted in well-defined polarization modes. Photon statistics exhibit strong antibunching. Together with its high efficiency and unmatched spectral purity, this kind of structure is predestined for the generation of single-photon states as required for numerous applications in quantum communication.

4.2.3 *Site-controlled QDs*

In all devices mentioned above the QDs were grown by self-organization in the Stranski-Krastanov mode. Consequently the positions of the QDs are uncontrolled and only by chance a QD will be located perfectly in the center of the oxide aperture. Usually the QD spatial density is high enough to ensure that at least one QD will be pumped for increasing pumping current. Nevertheless to increase the device efficiency the position of the QDs should be controlled. This section describes the first attempt to pump a single site-controlled QD electrically in a pin-diode structure.

In order to prove the presence of site-controlled QDs the following measurement techniques were applied: First the spatial distribution of the electroluminescence was checked by taking pictures of the sample under applied bias and without illuminating lights. Due to the high sensitivity of the CCD camera, the luminescence even of a single QD is visible. The camera has no spectral filtering, hence to study the spectra of the detected bright spots, spatially resolved micro-EL measurements (mapscans) were performed. In a third step on spots, demonstrating luminescence at wavelengths $\geqslant$915 nm (as expected for QDs), excitation power and polarization dependent measurements were performed to assign the luminescence to the recombination of specific electronic states.

Figure 4.9 shows the electroluminescence spectra and microscope images of one device measured at 15 K. The bottom part of figure 4.9 shows one EL spectrum over a wide spectral range of 780 to 1050 nm for a bias of 2.25 V with a current of 20 µA. As for the devices in the previous section, no luminescence from the GaAs bulk material is visible, indicating the high

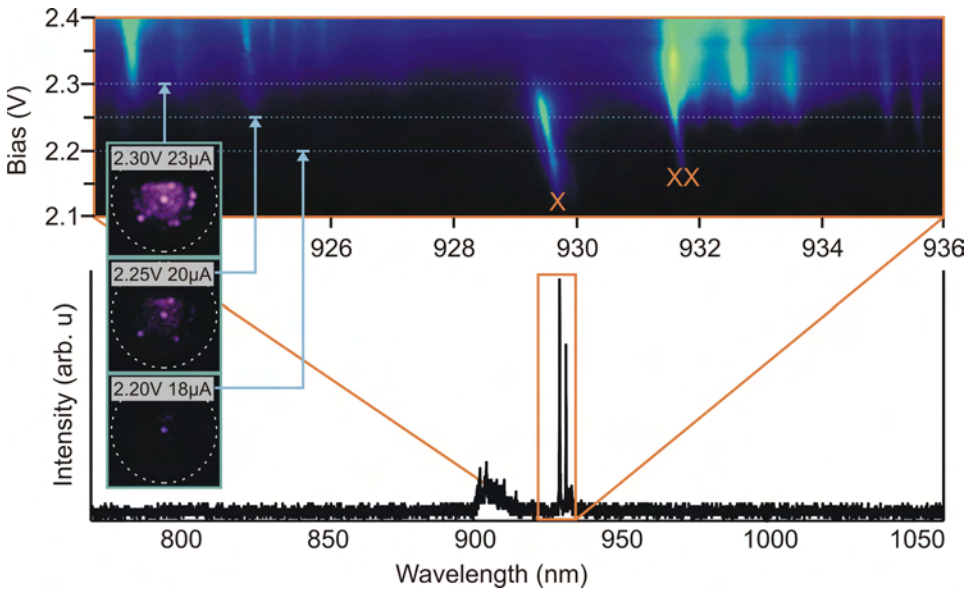

Figure 4.9: Bottom: EL-spectra for 2.25 V and 20 µA on a large spectral range. Top: Excitation power dependent spectra of the sharp luminescence line around 930 nm in a logarithmic color scale. The insets show a microscope image of the sample surface for three different biases.

injection efficiency into the QDs. Two sharp luminescence lines are visible around 930 nm, beside a broad luminescence around 910 nm. The middle picture in the inset shows the corresponding image of the sample surface. Four luminescence spots (including one in the center) are clearly visible, with an almost homogeneous background.

Note the large oxide aperture with a diameter of about 10 µm in contrast to the sub-micron aperture in the previous section. Here a large oxide aperture was used for two reasons: First to prove the absence of other QDs beside the site-controlled one in the center and secondly to account for a slight maladjustment between the site-controlled markers and the etched mesa position during the device processing.

Spatially resolved micro-EL measurements (not shown) demonstrate that the two spots in the center and at the lower left have luminescence wavelength around 930 nm, whereas the other spots exhibits luminescence at shorter wavelengths around 910 nm. The two sharp luminescence lines in figure 4.9 bottom originate from the center spot. The position on the device and the longer wavelength indicate that the sharp luminescence lines originate from the site-controlled QD, whereas the broad luminescence originates from unintended QDs, quantum dashes or rough quantum wells. The etched hole for the site-controlled QD was positioned in the center of the diode and should have accumulated the InAs during the QD growth. This should result in a larger size of the site-controlled QD in comparison to unintended QDs. Consequently the luminescence of the site-controlled QD could be expected at longer wavelengths than for the unintended QDs.

Unfortunately in the images of the sample surface (inset of figure 4.9) for all bias $\geqslant$2.25 V more than one luminescence spot is visible. Beside the spots

a homogeneous background luminescence can be observed. For a bias of 2.3 V the background luminescence fills almost the entire oxide aperture with a diameter of about 10 µm. Outside the oxide aperture a number of luminescence spots are visible, indicating "self-organized" current apertures as described in section 4.2.1. These images suggest that more QDs than the single site-controlled one were grown on the diode area.

Next, the origin of the sharp luminescence line outside the center of the diode is analyzed. The top part of figure 4.9 shows the EL spectra in dependence of the applied power in a logarithmic color scale. For a bias $\leqslant$2.2 V only one line is visible. The intensity of this line saturates at about 2.25 V and decreases as the bias is increased. Due to the larger oxide aperture the current, necessary to saturate the exciton emission, is 20 µA and hence three orders of magnitude higher than the few nA needed for the sub-micron aperture devices. Parallel to the intensity saturation a second line appears at two nanometer longer wavelength (ΔE = 2.8 meV). The luminescence shifts to higher energies for increasing bias, as expected by the Quantum confined Stark effect (see section 2.3.4). In polarization dependent measurements (not shown) these two lines exhibit an opposite energy shift, resulting in a FSS of 16$\pm$5 µeV. Hence the luminescence lines can be assigned to the recombination of the uncharged exciton and biexciton.

A second device from the same wafer demonstrated sharp luminescence lines around λ= 970 nm with intensities much higher than those from the device presented above. Figure 4.10 left shows the EL spectra at 2.06 V and 0.52 µA measured at 15 K. The emission wavelength of this QD is much longer, indicating a larger QD and hence a more efficient InAs deposition during the growth. The inset of figure 4.10 shows the spatially resolved micro-EL measurements for a spectral range from 960-974 nm at the same bias. Only one luminescence spot is visible, which is unfortunately not located in the center of the diode. For wavelengths between 910-940 nm more than five spots are visible. The high intensity of the luminescence allows performing photon correlation measurements, which are shown in figure 4.10 right. A clear antibunching dip is visible with a $g^{(2)}(0)$ value of 0.5. A simulation taking into account the limited time resolution of the APD-based HBT according to equation 3.11 (orange line) results in a true $g^{(2)}(0)$ = 0.3, proving the single photon emission from this device.

Unfortunately the luminescence intensity from these devices with site-controlled QDs was significantly lower than from devices with self-organized QDs (section 4.2.2). The patterning of the substrate before the QD growth should act as a nucleation point for the site controlled QDs [Atk08]. This forced nucleation results in QDs, containing more defects than self-organized QDs. These defects leads to non-radiative recombination channels and the luminescence is usually broader [Kir06] and less intense [Che09, Alb10a] than from self-organized QDs.

Another remarkable result in this study of devices containing site-controlled QDs is that the results obtained in micro-EL and -PL measurements are comparable and both techniques show almost the same spectra. This is not obvious for the following reason: The QDs are embedded in the middle of a

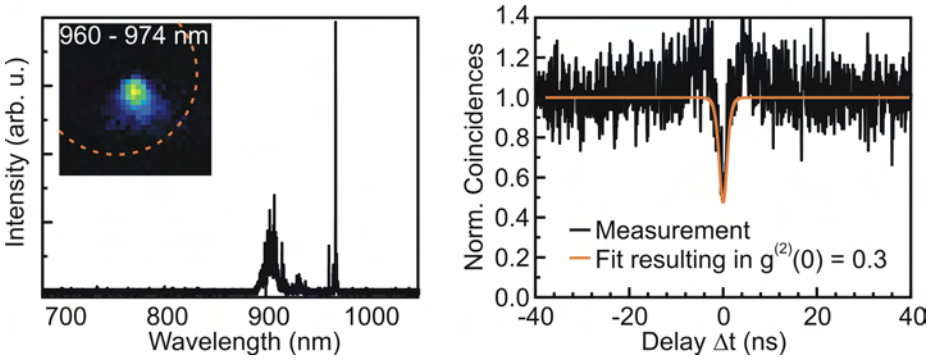

Figure 4.10: Left: EL overview spectrum at a current of 0.52 µA and 2.05 V. Two sharp luminescence lines are visible at 970 nm. The inset shows the spatial position of the luminescence in a spectral range of 960-974 nm on the diode (orange dashed line). Right: Second order correlation measurement of the luminescence line at 970 nm, proving single photon emission.

pin junction, consequently in PL measurements the built-in electric field of about 100 kV/cm will disjoin the generated electron-hole pairs. Hence even at low temperatures only a very small number of charge carriers may be confined. Therefore the luminescence of a single QD in a mesa with 30 µm diameter may be too low to be detectable.

In conclusion this section described the first realization of a single photon emitter based on site-controlled QD although the results demonstrate only partly success in the control of the QD growth positions. All devices demonstrate some other QD luminescence beside the expected single site-controlled QD. The two devices presented here show two different deviations: In the first device (figure 4.9) a QD emitting at longer wavelength is visible at the center beside other QDs, were at least one of them emits at the same wavelength. In the second device (figure 4.10) the most promising QD is not located in the center of the device. Nevertheless both devices shows that the spatial QD density is drastically in this approach- Both devices demonstrate EL from single QDs without strong current constriction. The photon correlation measurement in figure 4.10 is the first demonstration of non-classical light emission from a sample with site-controlled QDs under electrical pumping.

4.3 A RESONANT CAVITY LED

All single photon emitter devices in the previous sections were not optimized regarding their photon out-coupling efficiency . This can be done by resonant coupling of the generated photons to a micro-cavity (see section 2.5 on page 31) thus giving the photons a preferred emission direction. Due to the Purcell effect the spontaneous emission rate will also be enhanced. Both effects are very helpful for the realization of a single photon source with a large out-coupling efficiency and a high repetition rate.

This section describes an electrically driven single photon source with high out-coupling efficiency and a repetition rate up to 1 GHz. The device

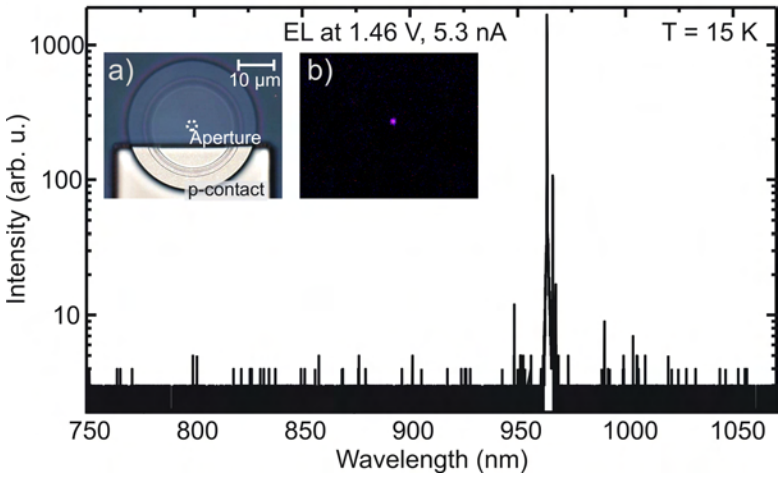

Figure 4.11: EL overview spectrum in a semi-logarithmic scale. The single line is about 3 orders of magnitude more intense than any other luminescence. The inset shows a microscope image of the device a.) with additional illumination and b.) under electrical pumping with 5.3 nA

consists of a QD layer embedded between 4/12 DBR mirrors on top and bottom respectively. The so formed micro-cavity has a quality factor of Q= 130 with a center wavelength of 960 nm. A pin junction allows electrical pumping. A detailed description of the device processing can be found in section 3.4.3. In the following this device will referred to as Resonant Cavity Light Emitting Diode (RCLED). With this device a record pure spectrum and an ideal single photon characteristic with a $g^{(2)}(0) = 0$ value were achieved. The optical response of the device to a 1 GHz electrical signal is faster than the time resolution of NIR-optimized APDs and demonstrates an enhanced spontaneous emission rate.

4.3.1 *Spectral Characteristic*

The inset a.) of figure 4.11 shows a top view microscope image of a processed device. Due to the top DBR the oxide aperture is not visible and marked with a circle. In the inset b) the device is pumped with a current of 5.3 nA at 1.46 V. Only one single luminescence spot from the center of the device is visible, indicating the efficient current constriction by the oxide aperture.

Figure 4.11 shows the electroluminescence at 15 K over a spectral range of 400 nm in a semi-logarithmic plot. The spectrum was measured under pulsed excitation as will be described in section 4.3.2, but is the same as for a cw excitation at 1.46 V with a current of 5.3 nA. Two dominant sharp luminescence lines are visible around 965 nm, where all further sources of luminescence over the entire range are at least three orders of magnitude less intense. No recombination in the GaAs bulk or the wetting layer is observed. This record signal to noise ratio (SNR) of the device demonstrates the efficient electrical carrier injection into a single QD. The intensity of the single QD luminescence line is 20 times higher than in the single QD LED without cavity presented in section 4.2.2 under comparable pump situation.

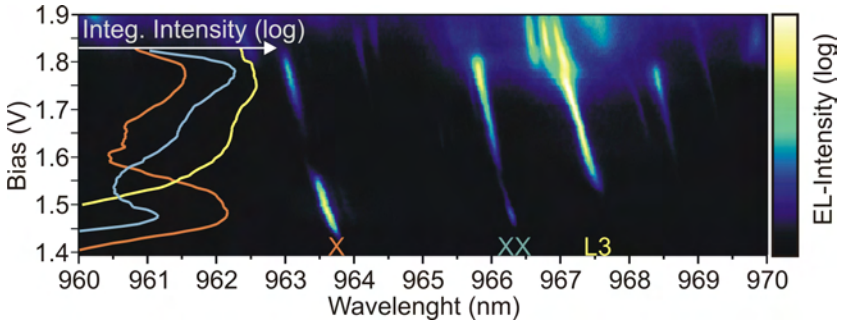

Figure 4.12: Color scale encoded electroluminescence of the RCLED in dependence on the bias taken at 15 K. The lines at the left border show the integrated intensity of the X, XX and L3 luminescence for the corresponding bias. At 1.46 V a clear resonance is visible.

The increased intensity is mainly induced by the preferred emission direction of the generated photons due to coupling to the micro-cavity . Theoretical calculations on this device predict a Purcel factor of up to 3 [Mö9] . Hence the out-coupling efficiency is increased at least by factor of 7 by the micro-cavity.

The spectral characteristics of the electroluminescence had been studied in detail by polarization and power dependent measurements. Figure 4.12 shows a color scale encoded series of spectra for increasing bias with high spectral resolution. Three dominant luminescence lines are visible and their integrated intensities for the corresponding bias are shown on the left side of figure 4.12. In polarization dependent measurements (figure 4.13 left) both luminescence lines at lower wavelength demonstrate an opposite energy shift, with a fine-structure splitting of 40 μeV. From cross-correlation measurements (see figure 4.15) these luminescence lines can be assigned to the recombination of the uncharged exciton (X) and biexciton (XX). The observation of uncharged X and XX recombination demonstrates the equal injection of electron and holes into the QD and is prerequisite for the realization of an electrically pumped entangled photon source.

A third line (L3) shows no polarization dependence, but a clear antibunching in cross-correlation measurements with the XX luminescence. Hence this line can be assigned to the recombination of a charged exciton or biexciton in the same QD.

The integrated intensities of the X and XX luminescence lines (blue and orange line in the left side of figure 4.12) show two resonances, similar to the resonant tunneling injection presented in section 4.1. Up to a bias of 1.46 V the intensity of both lines increases and drops back for increasing bias. In a double logarithmic plot over the current the corresponding slope of the intensity increase is 4.4 and 9 for the X and XX respectively. Although these values are much higher than the expected values 1 and 2, they reproduce the much higher pumping intensity required for the XX emission. In this first resonance the X intensity is always higher than the XX, hence the pumping rate is not high enough to saturate the X luminescence. Nevertheless the maximum X intensity at 1.46 V was used for the intensity comparison with previous devices without cavity.

A calculation of the band diagram of the RCLED using finite element to solve the Poisson equation [Win99] supports the tunneling theory. At a bias of 1.46 V for both electron and holes a triangular barrier of about 30 nm width and 160 meV height remains. This barrier has to be either overcome by thermal energy or tunneling. A temperature of 15 K corresponds to an average thermal energy of about 1.2 meV and is hence not sufficient to overcome the barrier.

For bias > 1.55 V all three luminescence lines increase, while the X intensity is always the lowest. This can be explained by the dark state of the exciton: The injected electrons and holes are not spin controlled and as mentioned in section 2.3.3 the dark state of the exciton has a lower energy than the bright states. Hence at low temperatures the electron and holes may occupy the exciton dark state and cannot recombine. In this case the biexciton state can be filled even at a low pumping rate. The charged state of the L3 luminescence has no dark state and is therefore more intense than the X luminescence. In fact at higher temperature the ratio of the X and XX luminescence changes. With higher temperature the probability to occupy the exciton bright state rather than the dark state increases due to the increased thermal energy.

In fact for a temperature of 80 K the bias resonances of the exciton and biexciton intensity vanishes (see figure 4.16 on page 82 left). At 80 K the maximum exciton intensity is two times lower than from the biexciton. This corresponds to the expected intensity ratio: The luminescence intensity I_{lum} is given by

$$I_{lum} = p_{state}/\tau_{state}, \tag{4.1}$$

where p_{state} is the occupation and τ_{state} the life time of the corresponding state. Since the biexciton has two possible emission channels its life time is approximately half the exciton life time. Consequently the maximum biexciton luminescence intensity should be twice the maximum exciton intensity for a simple three level system without dark state blocking.

A detailed study of the charge carrier injection process and the dark state blocking in dependence on the temperature has to in addressed to future work.

All three luminescence lines in figure 4.12 demonstrate a blue shift for increasing bias, which is induced by a reduced quantum-confined Stark effect. Beside the blue shift, the X and XX luminescence lines show a splitting in two or even three lines, separated by a few tens of µeV. The right panel of figure 4.13 shows a high resolution spectrum of the X luminescence. These lines merge together for increasing intensity. For higher bias above 1.78 V the L3 line splits up in two luminescence lines. The origin of this line filamentation is still not clear. It cannot be induced by the fine-structure splitting, since the lines are not polarized and the splitting for both the X and XX line decreases for increasing current. It also cannot be induced by additional charge carrier injected into the QD. The resulting coulomb energy is in the order of a few meV and much too high. One explanation may be a change in the intermixing states. The electronic states in the QDs

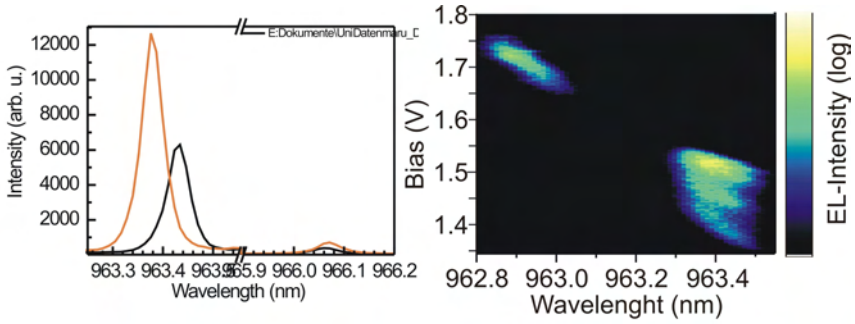

Figure 4.13: Left: Polarization dependent measurements on the X and XX line, demonstrating a FSS of 40 µeV. Right: The starting luminescence of the X line from fig. 4.12 in high resolution. For low bias the exciton emission segments into three lines.

do not consist of pure spin states of the electrons and holes. For example the triplet state of the hot trion are intermixing, and due to the correlation the energy levels differ from pure states [Edio7, Waro9]. A change in the pumping current may lead to a change in the intermixing ratio. For a better understand of the line filamentation further measurements and theoretical modeling are necessary.

4.3.2 *A Single Photon Source Driven at 1 GHz*

Single photon sources operating at high repetition rates are required to achieve high transmission rates in quantum key distribution systems. The RCLED presented in this work is capable of single photon emission at pumping rates of up to 1 GHz.

The DBR mirrors of the micro-cavity increase the serial resistance R and the capacity C of the RCLED in comparison to the single QD LEDs presented in section 4.2. This may reduce the maximal pumping rate into the device, since the bandwidth is given by $f = \frac{1}{2\Pi RC}$. In fact for a pulse, in terms of bias, equal to the cw excitation (low voltage V_{low}=0 V and high voltage V_{high}= 1.5 V) the highest pumping rate, for which EL was observable was about 200 MHz. Above this frequency the pulse shape was so deformed in the cables, the chip mount and the RCLED that the resulting bias at the pin junction was too low to pump charge carriers into the QDs. By a systematic variation of V_{low} and V_{high} for different frequencies the maximum repetition rate was studied. The RCLED could be pumped with a repetition rate of 1 GHz and a pulse width of 350 ps by increasing V_{low} and V_{high} to 0.7 V and 3.44 V respectively. The corresponding EL spectrum is shown in figure 4.11 and is the same as for a cw excitation with 1.46 V, corresponding to the first resonance of the X intensity.

The photon correlation measurement of the X luminescence driven at the above mentioned pulsed excitation is shown in figure 4.14 bottom. For this measurement the APD based HBT with a time resolution of 600 ps was used. A clear antibunching dip with $g^{(2)}(0)$ =0.25 proves the single photon emission at this excitation. The enhanced values at ±7 ns are due to the cross

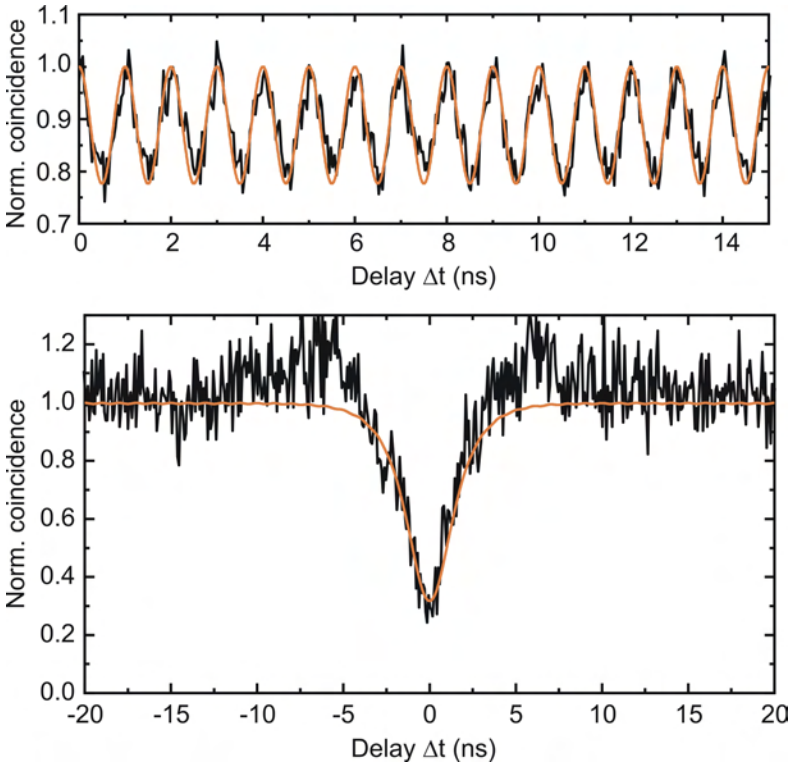

Figure 4.14: Top: The optical response of the RCLED to an electrical 1 GHz signal with a pulse width of 350 ps and simulation of a pulse train with 400 ps width (orange line). Bottom: Correlation measurement at 1 GHz demonstrates clear anti-bunching. The orange line is a simulation of a pulsed perfect single-photon device ($g^{(2)}(0) = 0$) with 1 GHz repetition rate, taking into account the limited time resolution of 0.6 ns of the setup.

talk of the APDs (see 3.3.3). The measured $g^{(2)}$function in figure 4.14 looks as expected for cw rather than pulsed excitation which will be explained in the following.

To analyze the $g^{(2)}(\Delta t)$-function a simulation according to equation 3.11 is shown as orange line. In this simulation a time resolution of 0.6 ns and a perfect single photon source with $g^{(2)}(0) = 0$ and a repetition rate of 1 GHz has been assumed. The antibunching dip of the simulation agrees excellently with the measured data, proving that no background emission disturbs the single photon characteristic of the RCLED. Due to the limited time resolution, the pulses having a width of 0.6 ns overlap and only a small variation of the $g^{(2)}$value between 1 and 0.996 is visible. This variation cannot be observed in the measurement (black line) due to the noise. Hence the perfect agreement between simulation and measurement proves the perfect single photon characteristic of the RCLED.

In order to prove the pulsed emission from the RCLED the time resolution has to be improved. Therefore the trigger signal of the pulse generator was used as start signal and one APD as stop signal for time-correlated measurements. The measured optical response to the 1 GHz excitation (fig. 4.14, top) agrees very well with a theoretical simulation of a pulse train

with a FWHM of 400 ps (orange line). The temporal resolution of the APDs is 350 ps, thus presently still limiting the measured optical response. The exciton lifetime without cavity is in the order of 1 ns [Thoo1, Mico3, Feuo8]. Hence the short optical response of the RCLED demonstrates an appreciable reduction of the exciton lifetime by at least a factor of two, due to the Purcell effect .

Commercial available APDs have time resolution which is too slow to measure the pulsed single photon emission. The combination of both measurements in figure 4.14 demonstrates the perfect single photon emission from the RCLED driven at a repetition rate of 1 GHz.

4.3.3 *Photon Correlation with Enhanced Time Resolution*

To study the photon characteristics of the fast RCLED in more detail superconducting single photon detectors (SSPD) were used. These detectors have a six times better time resolution than the APD (see section 3.2.2), which allows an improved measurement of the $g^{(2)}$function and the exciton life time.

Figure 4.15 compares the $g^{(2)}(\Delta t)$ function under cw bias of 1.495 V (8 nA) measured on the X luminescence, using APDs (black line) and SSPDs (orange line). For the SSPDs the antibunching dip is much narrower and drops to a smaller $g^{(2)}(0)$ value, than in the APD based measurement. This comparison of two HBTs with different time resolution legitimates the $g^{(2)}$-function analysis, presented in section 3.3.4 on page 49: As well as for the time-constant as for a correct $g^{(2)}(0)$ value the time resolution of the system has to be taken into account.

As mentioned in section 2.3.3 the biexciton-exciton decay cascade can be used for a source of entangled photons. To measure the decay time in this cascade cross-correlation measurements were performed. Therefore the second version of the HBT (see section 3.3.2) has been used and the monochromators in front of the start and stop detector were moved to different wavelengths. Here the start detector is only reached by photons from biexciton recombination (966.2 nm) and the stop detector by those of the exciton recombination (963.6 nm).

The corresponding $g^{(2)}_{cross}$ measurement at a bias of 1.72 V is shown in figure 4.15 right. Note the semi logarithmic scale necessary to show all details of the measurement across three orders of magnitude and which is untypical for plotting the $g^{(2)}$ function. A pronounced peak at 0.3 ns indicates the enhanced probability, that after a biexciton an exciton is detected. A measured coincidence for $\Delta t \neq 0.3$ ns means that two photons, which do not originate from a direct X-XX cascade have been detected. Hence in figure 4.15 right the coincidences with $\Delta t \neq 0.3$ ns are reduced and the absolute number of coincidences is small. Nevertheless the $g^{(2)}(0)$ value drops to 0.07, proving that both emission lines originate from the same QD. The decay of the bunching dip at $\Delta t = 0.3$ ns to higher delay times is limited by the exciton life time [Moro1]. The orange line in figure 4.15 shows an exponential fit

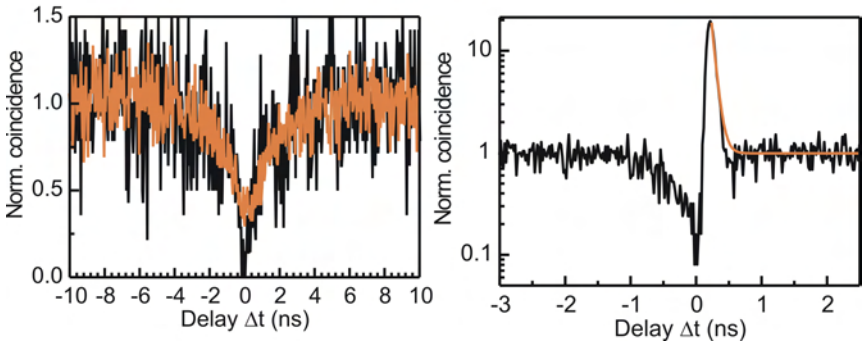

Figure 4.15: Left: Comparison of the photon correlation measured with APDs (orange line) and SSPDs (black) on the XX emission line. Right: Cross-correlation measurement on the X (start) and XX emission. The X life time can be derived from fast decay of the correlation peak to longer time. An exponential fit (orange line) yields an X life time of less than 80 ps.

of the decay, yielding in an exciton life time of less than 70 ps. This again proves the reduced exciton life time in the RCLED due to the Purcell effect.

The FWHM of the bunching dip is only 140 ps and equal the time resolution of the SSPDs (see section 3.2.2). Previous measurements of the X-XX cascade used APDs and results in an exciton life time comparable to values obtained from time resolved PL measurements [Moro1]. The here presented first measurement with such a high time resolution may be also a key to a recently proposed new scheme for the generation of entangled photon pairs by time reordering (see section 2.3.3 and [Reio8a, Avro8]). The measurement presented in figure 4.15 suggests that the X luminescence appears directly after the XX recombination. Hence no time reordering might be necessary.

In fact the techniques presented here provide a more accurate measurement of the exciton lifetime than obtained in time resolved photoluminescence measurements. Here the biexciton emission triggers the start signal and therefore the QD is in the prepared exciton state. In contrast to this in PL measurements the optical response to a short laser pulse is measured. Here the charge carrier has to be generated and to relax to the lowest level in the QD, before the exciton can recombine. Consequently the exciton lifetime will be overestimated due to these processes. The new SSPD based setup and the single photon device with low QD density allow for the first time to compare the life time measured by cross-correlation and time resolved PL.

4.3.4 *Single Photon Emission at 80 K*

The efficient pumping of only a single QD and the increased out-coupling efficiency of the RCLED allows increasing the temperature to 80 K preserving the non-classical light emission.

With increasing temperature it is more challenging to achieve single photon emission from a QD for two reasons: First the luminescence becomes more spectrally distributed. As described in chapter 5 acoustic phonon scattering leads to a broader spectrum of the single QD luminescence. In

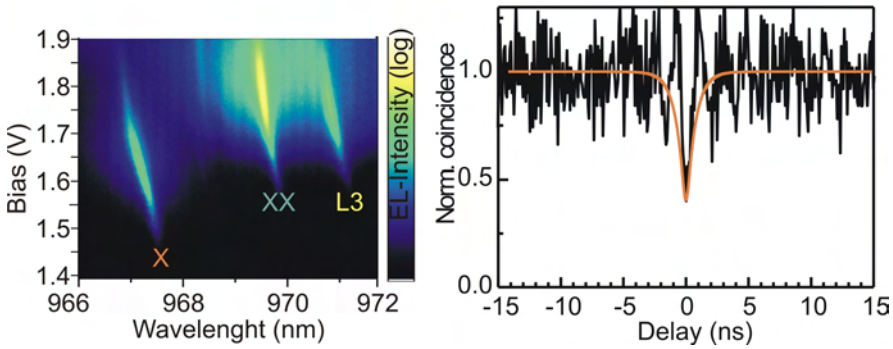

Figure 4.16: Left: EL at 80 K for different applied bias in a logarithmic color scale. The resonant tunneling excitation has disappeared. Right: Photon correlation measurement of the biexciton luminescence demonstrating the single photon characteristic at 80 K. The orange line is a simulation taking into account the time resolution of 150 ps and resulting in a $g^{(2)}(0) = 0.3$

contrast to low temperature measurements two luminescence lines with a spectral distance of only a few nms will overlap at higher temperatures. This may lead to an increased $g^{(2)}(0)$ value [Seb02]. Secondly the charge carriers have a higher thermal energy and the activation of charge carriers in the QDs may not be sufficient to confine the charge carriers. Hence the luminescence intensity drops with increasing temperature. Also the higher thermal energy increases the current path and resonant tunneling into the QDs, as presented in section 4.1, will no longer reduce the number of pumped QDs.

Figure 4.16 shows the electroluminescence of the RCLED at 80 K in dependence of the applied bias. The intensity is color encoded in a logarithmic scale. In comparison to the measurement at 15 K shown in figure 4.12 three main differences are visible. First, the intensity resonance at 1.46 V disappears and the biexciton luminescence becomes dominant after the saturation of the exciton luminescence. Secondly for all bias the biexciton luminescence is more intense than from the L3 line. Hence the dark state blocking seems to be reduced. Third, all three luminescence lines have a broad spectral distribution due to phonon scattering. Nevertheless no other luminescence lines are visible for the same bias range as in the 15 K even at a larger spectral range than presented in figure 4.16 left.

The high out-coupling efficiency of the RCLED allows measurements of the photon correlation at up to 80 K. The $g^{(2)}$function measured on the biexciton luminescence at 1.78 V with the SSPD based HBT is shown in the right panel of figure 4.16. Although the XX and L3 emission partly overlap a clear antibunching down to 0.4 is visible. The orange line is a simulation according to equation 3.11 with a time resolution of 0.15 ns and a decay time of 0.7 ns. The resulting $g^{(2)}(0)$ value of 0.3 proves single photon emission at 80 K.

The single photon characteristic of the RCLED at 80 K is of high interest for commercial applications. This temperature is above the temperature of

liquid nitrogen (77 K) allowing easier and cheaper cooling of single photon devices.

4.4 SUMMARY

This chapter reports the characterization of three different types of devices, representing milestones towards an efficient, easy to handle single photon emitter based on QDs: Beginning from a "poor-mans" single QD LED, without any current constriction, to single photon sources, where the current is constricted by an AlO_x aperture to a single QD. In this kind of device MOCVD and MBE grown self-organized QDs and site-controlled QDs were studied. In the final single photon device the out-coupling efficiency and pumping rate was increased by coupling the single QD to a micro-cavity.

The first section shows how to pump a single QD electrically simply by reducing the applied bias well below flatband condition. The observed concurrent resonant tunneling of electron and holes is of fundamental interest. Here the interaction of independent electron and holes with the exciton state bound in the QD is studied. A similar effect has been observed in more sophisticated devices such as the RCLEDs of section 4.3.

Single-QD LEDs, which include an appropriately placed and sized sub-micron oxide aperture close to a low density InAs QDs layer, allow injecting a single hole and a single electron into a single QD with high efficiency. In this sense a single-QD LED as presented in section 4.2 is the ultimate limit of an LED. Excitonic emission from QDs allows the extraction of single photons with a well-defined polarization state.

Finally, inserting the QD in a resonant cavity LED (section 4.3) increases the out-coupling efficiency by a factor of 20 and driving it at repetition rates of 1 GHz yields in a $g^{(2)}(0) = 0$. The optical response of this device is too fast for APDs, and a new type of detectors based on superconducting strips has to be introduced. By comparing $g^{(2)}$measurements with APDs and superconducting detectors, the analysis of the photon correlation function as presented in section 3.3.4 has been justified. Due to its spectral purity the RCLED demonstrates single photon emission up to a temperature of 80 K. A comparable high temperature for an electrically driven QD based single photon emitter has been achieved so far only for InP QDs [Reio8b]. These QDs emit photons in the visible range, which is not suitable for fiber transmission.

If the fine-structure splitting is tuned to zero by QD growth on (111) planes as described in chapter 6, entangled photon pair emission from an electrically pumped device is feasible. Together with the extreme spectral purity such a LED has the potential for an efficient ready-to-go single/entangled photon source for future applications in optical quantum information processing.

5 PHONON COUPLING

Besides non-classical light emission presented in Chapter 4 single QDs also provide the probability of studying the coupling between matter and electronic states. This chapter reports a comprehensive study of both exciton-acoustic- and optical-phonon interaction in a highly efficient single photon source, based on an electrically driven single InGaAs/GaAs QD. In the first part acoustic scattering will be discussed and the second part describes optical phonon scattering.

Electron-phonon coupling strongly influences the luminescence line shape, dephasing and coherence of the emitted photons and thereby the most important characteristics of a non-classical light source. By comparing experimental data with calculated spectra a quantitative understanding of the line shape and the dominating phonon modes was achieved. The analysis shows the impact of small variations in the electron and hole wavefunction on the phonon coupling. No localized phonons were observed and the line shape of the optical phonon replica can be explained by the limited life time of the phonons and their dispersion.

In the frame of this work first evidence of acoustic phonon scattering arose from the investigation of the single QD LED presented in section 4.2.2, whereas the LO-phonon scattering was studied first on the "poor-mans" single photon device in section 4.1. The intensity of phonon scattered light can be about four orders of magnitude less than from the direct recombination process. Hence the key for a detailed study of the phonon scattering was the high photon out-coupling efficiency of the RCLED, presented in section 4.3. All measurements presented in this chapter were done at the RCLED. The theoretical modeling in this chapter was done by Matthias-Rene Dachner from the theory department of the Technische Universität Berlin.

5.1 ACOUSTIC PHONON COUPLING

In order to obtain spectra with a sufficient large dynamic range in intensity series of spectra with 10 s integration time each were summed up. This technique also allows easily identifying and removing of signals resulting from the absorption of myons.

Figure 5.1 shows the sum of 300 spectra at a bias of 1.41 V and a current of 5 nA of the exciton emission line for each given temperature. In a semi-logarithmic plot a clear broadening of the emission is visible. The features at -7, -5 and -3.5 meV from the dominating zero phonon line (ZPL) can be attributed to the recombination of other complexes in the QD or to weak luminescence from other QDs. These features vary from device to device and therefore are not related to phonon scattering. The temperature dependence of the exciton peak position has been removed from fig 5.1a by plotting the

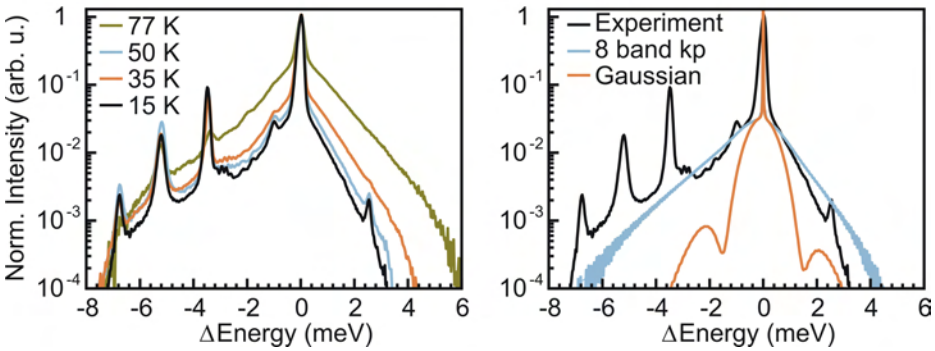

Figure 5.1: Semi logarithmic plot of the EL intensity of a single QD. a.) With increasing temperature the line broadening increases due to stronger acoustic phonon interaction. b.) Comparison of the measured line shape at 15 K with two calculated spectra, using alternatively a simple Gaussian or a realistic 8 band $k \cdot p$ wave function.

spectra on a relative energy scale and the intensity scale was normalized. In these measurements the line width of the ZPL is limited by the spectral resolution of the setup.

At low temperatures (15 and 35 K), the broad sidebands of the ZPL are asymmetric due to spontaneous phonon emission, with a larger intensity at the lower energy side. For increasing temperatures (50 and 77 K) the broadening increases and becomes symmetric. Such properties of the sidebands are typical for acoustic phonon scattering: By emission or absorption of a phonon the energy of the emitted photon will be reduced respectively increased by the phonon energy. At lower temperatures, the phonon density n_{ph} is low and therefore, due to spontaneous processes, phonon-emission ($\sim (n_{ph}+1)$) of an (acoustic) phonon has a higher probability than the absorption ($\sim n_{ph}$). Hence, the resulting spectrum is asymmetric. With increasing temperature the phonon density increases ($n_{ph} \gg 1$) and the probabilities for emission and absorption become equal, resulting in a symmetric spectrum.

For the theoretical description of the luminescence spectrum including acoustic phonon scattering the exactly solvable independent Boson model [Kru02, Zim02, Fö3] was applied: This model describes the lowest optically active quantum dot transition as a two level system coupled to phonons by band diagonal interaction. For the numerical evaluation, well known GaAs bulk material parameters for the phonon dispersion and the deformation coupling [Lan87, Dac10] were used. Therefore, the line shape of the calculated spectra depends only on the electron-phonon coupling matrix elements determined essentially by the wave functions of the electrons and holes in the QD. To gain insight into the microscopic interaction and its sensitivity to the character of the electronic wave functions, two types of wave function were compared: Gaussian wave functions (i.e. the ground state of a harmonic oscillator) and wave functions calculated for a realistic QD using 8 band $k \cdot p$ theory [Sch07], respectively. Figure 5.1b shows the measured spectrum at 15 K in comparison to the theoretical line shape for

both wave function types. For a Gaussian wave function, often used in theoretical studies, the phonon scattering is strongly underestimated for any energy. In contrast to this, $k \cdot p$ wave functions reproduce the measured spectra very well. The large difference between the two calculated spectra demonstrates clearly the importance of realistic wave functions already for a qualitatively correct description of electron-phonon scattering. Another important result of the modeling of the measured spectra is the fact that they are perfectly reproduced by using GaAs bulk phonon parameters only.

5.2 OPTICAL PHONONS

In order to study scattering processes of optical phonons experimentally series of 1450 spectra of the LO-phonon replica were summed up, resulting in a 5 times longer integration time than for the acoustic phonon. Figure 5.2a compares two spectra of the same QD under the same bias condition: The black dashed line shows the exciton emission line around 1.3035 eV. For the second spectrum the energy scale (on the top of fig 5.2a) is shifted by 36.5 meV compared to the bottom scale. Three pronounced peaks are visible in this spectrum and each of them has a "counterpart" in the black spectrum. For other QDs we also found a "counterpart" separated by around -36 meV for almost every intense luminescence line.

These corresponding lines are attributed to the recombination of an exciton accompanied by the emission of a LO phonon. For different QDs the phonon energy varies between -35.7 and -36.6 meV with no systematic trend as compared to the ZPL energy. These energies are comparable to the LO phonon energy of strain-free GaAs bulk material of 36.59 meV [Lan87]. The variation of the phonon energy can be explained by differences in the strain of the GaAs material induced by size and composition of the actual QD [Hei96]. At the energy of the InAs LO phonon replica (30.3 meV), no luminescence is observed. In agreement with the results for acoustic phonon scattering. Consequently the electron and holes in the QDs interact predominantly with phonons from the surrounding GaAs. No emission caused by localized InAs-like phonons in the QD is observed.

Also of interest is the coupling strength of the exciton-LO phonon interaction. The coupling strength is usually described by the Huang-Rhys factor, given by the intensity ratio of the ZPL I_{ZPL} and the n-th phonon replica I_n (at zero Temperature) by: $I_n/I_{ZPL} = S^n e^{-S}/n!$ [Hua50, May03]. In figure 5.2 the intensity is normalized with respect to the ZPL. Both emission lines are located outside the cavity resonance in the stop band, so their intensities can be compared. The intensity of the LO phonon replica is about four orders of magnitude lower than the ZPL intensity, resulting in a Huang-Rhys factor $S \approx 10^{-4}$.

This is about two orders of magnitude smaller than reported in previous measurements of an ensemble of QDs (0.01-0.02) [Hei99b] and still one order of magnitude less than calculated for GaAs bulk phonons (0.008) [Nom92]. Hence the coupling of excitons to LO phonons in this electrically pumped single QD is reduced.

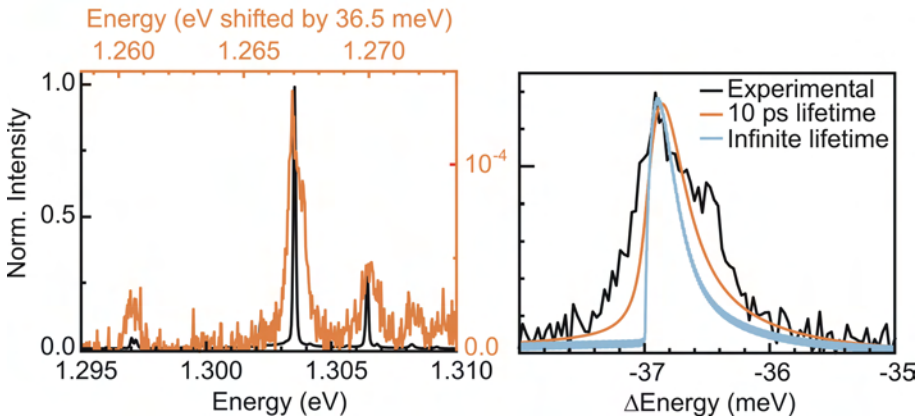

Figure 5.2: Optical phonon replica of a single QD. a.) The black line shows three ZPL lines each of them having a replica, separated by 36.5 meV (orange spectra, top energy scale) b.) Comparison of the LO line shape between experimentally measured (black) and calculated spectra with (orange) or without (blue) taking into account a finite lifetime of the phonon of 10 ps. A finite life time of the phonon provides a better description of the broad line shape of the LO phonon replica.

One reason for the previously overestimated phonon coupling may be the excitation: We drive our device with an applied bias close to the flat band condition, therefore the electrons and holes are close to the valence and conductance band edge. In contrast to this in PL measurements the electron-hole pairs are generated with energies larger than the band gap and they relax with phonon generation to the band edge. This phonon bath may increase the phonon coupling during the recombination process.

The line shape of the phonon replicas enables to access the coupling mechanism between the exciton and the LO phonon: The recombination of an electron-hole pair in a QD has a discrete energy and the line-width of the ZPL is only limited by the lifetime of the exciton to a few µeV [Bor01]. Therefore, any broadening of the luminescence upon generation of a LO phonon is due to the intrinsic phonon properties or coupling of the phonons to other modes. Figure 5.2 shows the LO phonon replica at larger spectral resolution. The resulting full width of half maximum of 700 µeV is well above the spectral resolution and about hundred times larger than for the ZPL. Hence, LO phonons of varying energies are generated during the recombination processes in the same single QD. Also, the line shape is again slightly asymmetric showing a faster decay on the low energy side than on the high energy side.

For a quantitative understanding of this coupling mechanism the experimental results are compared with a model (figure 5.2), where LO phonon assisted luminescence spectra are calculated using the independent boson model and approximating the real optical phonon dispersion by a cosine. For the coupling matrix elements, again Gaussian wave functions and 8 band k·p wave functions are compared. In contrast to the acoustic phonon coupling the influence of different wave function is less pronounced. In figure 2 can be seen that the LO phonon part of the spectral density shows a

much faster decay, than the acoustic phonon part. Hence the LO phonon replica for Gaussian and 8 band k·p wave functions differ only slightly. For a complete description of the LO phonon scattering process we also included a finite life time of 10 ps [Rud06, Bha94] of the LO phonons. The resulting LO replica in figure 5.2b reproduces the measured line shape very well, whereas a line shape with neglected phonon life time is too narrow.

5.3 SUMMARY

In conclusion acoustic and optical phonon scattering were studied on the most fundamental level, where a single photon and a phonon are generated by the recombination of a single exciton in a single electrically driven InGaAs/GaAs QD. By comparing experimental and calculated spectra it can be concluded that (i) GaAs bulk material phonon modes represent the dominant broadening mechanism and (ii) localized InAs-like phonons are not observed (iii) a large LO-replica broadening of $\approx$ 700 µeV is induced by interaction with large wave number phonons, having a finite life time (iv) $k \cdot p$ wave functions for the description of the excitons are of essence (v) the independent boson model using this wave functions provides the proper wave vector dependence for a quantitative understanding of the experimental results.

6 QDS WITH REDUCED FSS

This chapter presents micro PL studies on self-organized InGaAs QDs on (111) GaAs substrates with low spatial density and δ−function like luminescence lines. Due to their symmetrical electric field the fine-structure splitting should be zero and these QDs are promising candidates for sources of entangled photon pairs (see section 2.3.3) [Scho8]. Beside their shape the electronic structure of QDs grown on (111) GaAs is predicted to differ substantially from that of (001) QDs [Scho9]. Consequently "novel" emission patterns of the luminescence lines are expected.

In a first step the spatial distribution of these QDs were analyzed by measuring spectra at different position of the sample. Photon correlation measurements prove the origin of the luminescence from single QDs. In a second step the luminescence is systematically analyzed by finding recurring luminescence line patterns in power-dependent measurements as characteristic fingerprints. Finally the identification of the luminescence lines enables the investigation of FSS in polarization-dependent measurements. The sample structure is described in details in section 3.4.4

6.1 QD LUMINESCENCE

Since the wafer rotation was switched off during growth, the luminescence of the samples varies significantly on different areas of the wafers. Some parts emit spectral broad luminescence, having little in common with typical QD luminescence, whereas a small area showed spatially well separated luminescence centers, with spectral sharp luminescence lines. Figure 6.1 displays the spatial distribution of the luminescence in a spectral range from 1.295 to 1.315 eV. The color scale gives the value of the maximum intensity in this spectral range. On an area of 40 x 40 μm^2 several luminescence centers are visible. The spectra of four of them are plotted with identical intensity scales around the frame. Sharp luminescence lines which are typical for the discrete energy levels of QDs are visible. The line width of most of them is limited by the spectral resolution of our setup and the intensity is comparable to the luminescence from a single QD grown on (001) substrate. The distance between two QDs can exceed a few µm and the spatial QD density is significantly less than 10^9 cm^{-2}. Thus single-QD spectroscopy without additional spatial selection is possible.

To prove the presence of single QD in photoluminescence two kinds of measurement techniques can be utilized: First to demonstrate the non-classical light emission in photon correlation measurements and second to demonstrate sharp absorption lines in photoluminescence excitation spectroscopy (PLE). Both techniques were used in this work and will be presented in the following.

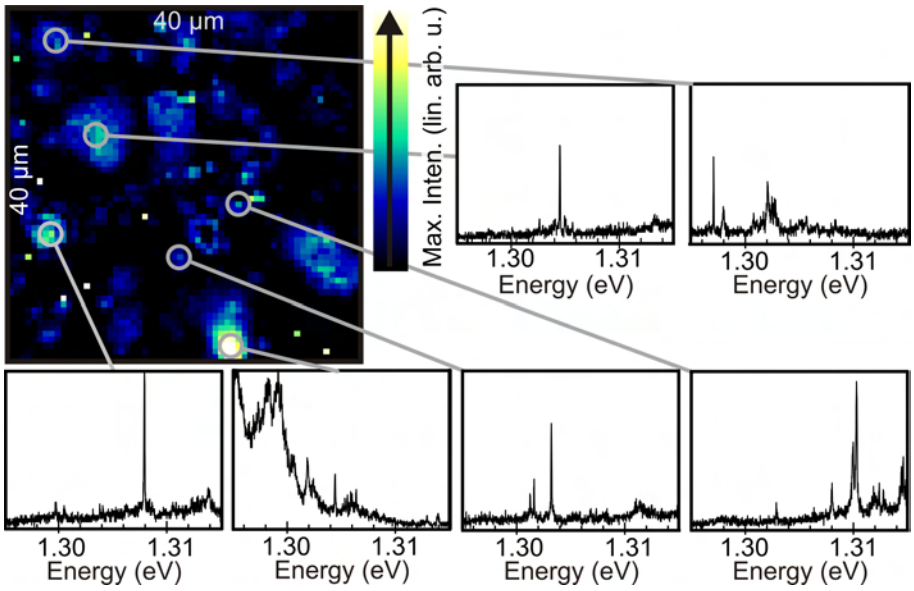

Figure 6.1: The color scale indicates the value of the maximum intensity between 1.295 and 1.315 eV. Local spectra are plotted for 4 positions with the same scaling of the intensity. b.)Second-order correlation measurement (black) and simulation (orange) resulting in a $g^{(2)}(0)$ value of 0.1.

Photon correlation measurements of the $g^{(2)}(\triangle t)$ function were performed with the HBT setup equipped with the APDs. Figure 6.2a.) shows the normalized $g^{(2)}(\triangle t)$ function of one single luminescence line. The increase $g^{(2)}$ at ± 5 ns is due to the so-called cross-talk (see section 3.3.3). The measured value of $g^{(2)}(0) = 0.3$ is mainly limited by the time resolution of the HBT. A simulation (orange line, using equation 3.11), taking in to account the time resolution of the setup, leads to $g^{(2)}(0) = 0.1$. Hence the emission of single photons and thereby the existence of QDs is proven.

First micro photoluminescence excitation measurements are shown in figure 6.2b.). This spectroscopy technique tests the absorption in higher excited states and virtual phonon states [Hei98]. In figure 6.2b.) shows PLE spectra measured on two sharp luminescence lines, for which the recombination energy is given as label. Both spectra demonstrate sharp lines, indicating the presence of sharp absorptions, which is typical for single QDs [Sie09]. Due to the quantization of electronic states in the QDs (see section 2.3.2) only for discrete energies a photon can be absorbed. This is in contrast to quantum wells or bulk material which have a continuous density of states, and therefore a continuous absorption characteristic.

The presence of single QDs with sufficient low spatial density and high luminescence intensity is a mayor step. In previous attempts to grow InAs QDs on (111) GaAs substrates tetrahedral shaped recesses were used [Sug95]. This leads to the formation of rather large dots with an homogeneous line width of a few meV. Another attempt to grow QDs on (111) substrates [Tsa98] resulted in a high density of very small QDs with a small localization energy, which are electronically close to quantum wells.

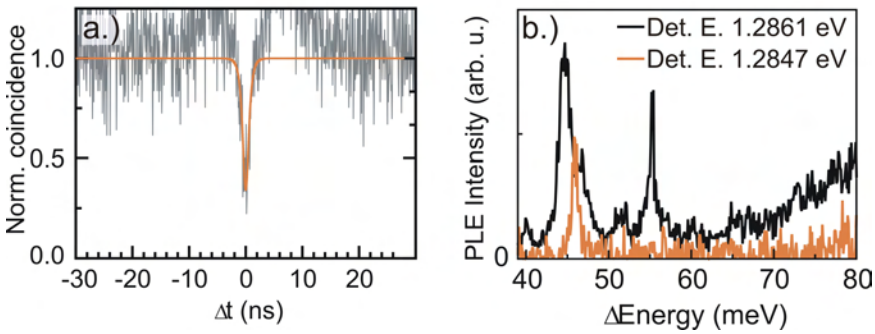

Figure 6.2: a.) Photon correlation measurements, proving single photon emission. b.) Photoluminescence excitation spectroscopy on two luminescence, which energies are given in the label. For both detection energie sharp absorption lines, corresponding to discrete excited states, are clearly visible.

6.2 IDENTIFICATION OF LUMINESCENCE LINES

After proving the origin of the luminescence lines to be from single QDs, the next step is the identification of these luminescence lines. In a first step the luminescence lines from the recombination of a single electron-hole pair should be identified. As far as a QD can be charged, luminescence from charged trions is expected, beside the recombination of neutral excitons.

The upper part of figure 6.3 shows the excitation power dependence of several photo-luminescence lines, originating from a single QD in the following referred to as QD1. With increasing laser power three luminescence lines appear simultaneously: One intense line at 1.306 eV (in the following labeled as line A) and two lines at 1.308 eV separated by 300 µeV (lines B and C). The intensity ratio of these lines is 4:1:2 (A:B:C) and their intensity depends almost linear on the excitation power. When the luminescence of these three lines saturates (at ≈100 nW excitation power) several other lines appear and upon further increase of excitation power the lines A, B and C fade. This behavior is typical for excitonic emission from a single QD [Rodo5]. Therefore the lines A, B and C originate from the recombination of single excitonic complexes from a single InAs QD grown on (111) GaAs substrate. The bottom part of figure 6.1 shows the photo-luminescence of a second QD2. As for QD1 three luminescence lines start first and sature before other luminescence becomes dominant. These three lines show the similar pattern as from the first QD: Two close lines (B and C) and one brighter single line at 4 meV higher energy. Four more QDs demonstrate this pattern of three lines with almost the same energetic distance and intensity ratio, exhibiting the same power dependence. In the following all lines from this typical fingerprint of excitonic recombination will be labeled with A, B and C.

For higher excitation intensity the recombination of biexcitonic complexes is expected. Indeed, in both power dependent PL measurements of figure 6.3 several other lines appear when the intensities of the lines A, B and C decrease (at ≈100 nW laser power). This behavior is typical for exci-

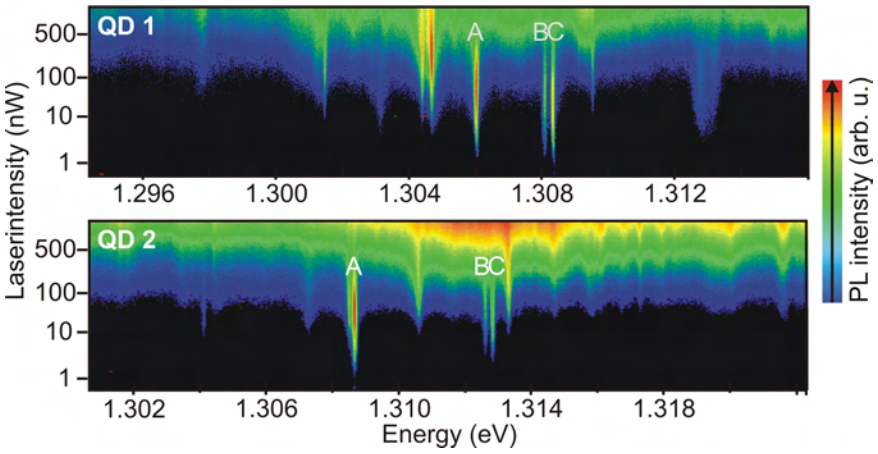

Figure 6.3: Excitation power dependence of the photoluminescence from two QDs. The luminescence lines from single excitonic complexes are denoted by A, B and C.

tonic and biexcitonic emission from a single QD: With increasing excitation power the filling rate of the QDs is higher than the recombination rate of an electron-hole pair. The mean occupation of the QD is larger than just one electron-hole pair and the luminescence from the excitonic complexes decreases, whereas the luminescence from biexcitonic complexes becomes dominant. Unfortunately due to charge carrier diffusion a higher excitation power also leads to a larger excitation spot diameter and more QDs may be pumped. The biexcitonic emission sometimes can be identified by the same spectral jitter of luminescence lines appearing at low and high excitation intensity[Töo]. Due to the absence of any spectral jitter in these samples, this identification method could not be applied. In contrast to the typical excitonic fingerprint, no pattern was found for the luminescence lines at higher excitation power. Hence the identification of the biexcitonic recombination stay open for future works.

6.3 FINE-STRUCTURE SPLITTING MEASUREMENT

The crucial parameter for the generation of entangled photon pairs is the FSS of the bright exciton state. In general, several excitonic complexes can be observed in the luminescence of a single QD: The uncharged exciton (X) consisting of a single electron-hole pair, the negative/positive trion (two electrons/holes with a single hole/electron, X+, X-) or even multiply charged excitons (X++, X–,...) [War97]. For non-zero FSS the bright exciton emission line will split into a linearly polarized doublet as will one of the emission lines of the X++ [Edio7]. Therefore the FSS can be measured in the luminescence of the uncharged and of the double charged exciton.

In order to determine a possible FSS for QDs grown on (111) GaAs substrate polarization dependent measurements were performed on lines A, B and C. Figure 6.4 shows the result in two different way for QD1 and QD2. In the upper part the intensity is color encoded and spectra for different polarizer positions are plotted. From these spectra the center positions

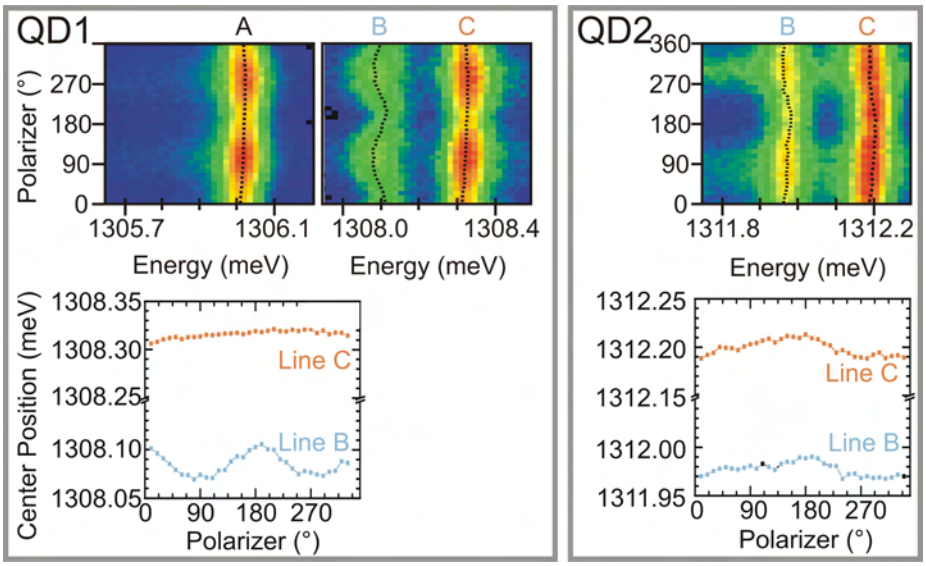

Figure 6.4: Polarization dependent measurements on QD1 (left) and QD2 (right). The center position positions (lower parts) were obtain by Gaussian fits. QD1 allows to identify the FSS on line B, whereas QD2 shows no FSS.

were obtained by fitting with a Gaussian. The resulting center positions in dependence of the polarization are plotted in the lower part of figure 6.4.

The intensities of lines A and C are clearly polarization dependent. For an angle of 90° the intensity is 1.5 times larger than that for 180°, while the energetic position does not change. On the other hand for QD1 line B shows almost the same intensity for all polarizations, but the energetic position (lower part in figure 6.4) shifts. A clear energetic change of about 40 µeV with a periodicity of 180° is clearly visible, whereas line C shows no systematic energetic shift. Therefore the luminescence of line B gives access to the FSS and originate either from the X or X++. Line A and C are probably from single charged trions. Spectroscopy on single QDs grown on (111) GaAs substrate is a new field and a complete assignment of the observed luminescence lines to transitions from well identified few-particle states has to addressed in future works.

Since line B can be used as an indicator for the FSS, now for other QDs with the same fingerprint the value of FSS can be measured. For QD2 the polarization dependence of the lines B and C is shown in the right part of figure 6.4 as a color plot and the corresponding energetic positions. Here line B exhibits only a very small energetic shift on the order of the determination limit of the setup (10 µeV). In contrast to QD1 the spectral shift is not periodically and not reproducible. The FSS of QD1 was the largest we found and on five other QDs (not shown) it is ranging from 30 µeV down or below the determination limit.

The non-zero FSS can be attributed to two effects mainly: The QDs were grown on a (111) substrate with a miscut of 2°. This may lead to the growth of elongated QDs along the steps on the (111) surface. Second, even the growth of GaAs bulk material on this substrate orientation is challenging. The samples exhibit a high density of dislocations, which may influence

the built-in piezo electric field and cause strain in one preferential direction. This may result in an asymmetric confinement potential, similar to that of QDs on (001) substrate. By optimizing the growth process theses effects can be eliminated.

6.4 SUMMARY

In this chapter the luminescence of single self-organized InGaAs QDs on (111) GaAs substrates was studied for the first time. The QDs have a very low spatial density and exhibit spectra with sharp and intense lines. The luminescence of the QDs demonstrates clear antibunching with an $g^{(2)}(0) < 0.3$ which proves single photon emission. On the basis of excitation power-dependent measurements on a number of QDs a typical luminescence fingerprint of QDs grown on (111) GaAs was identified. One of these lines allows the measurement of the FSS. The observed FSS ranges from 40 µeV down to the determination limit of our setup (10 µeV). This is a significant reduced value in comparison to QDs grown on (001) GaAs [Bay02, Seg05, Ste05] and therefore an important step towards the easy-to-process realization of entangled photon sources.

Spectroscopy on single QDs grown on (111) GaAs substrate is a new field and a complete assignment of the observed luminescence lines to transitions steming from well identified few-particle states requires further investigation. This work gives a proof of concept for micro-photoluminescence excitation (PLE) spectroscopy [War09] on this new kind of QDs. Detailed studies with these technique as well as the identification of the uncharged exciton and biexciton emission line have to be addressed in future work.

7 CONCLUSION AND OUTLOOK

In the work at hand self-organized InGaAs/GaAs quantum dots were investigated for their application as single photon sources. For this purpose a new micro-photoluminescence and electroluminescence setup was built. This setup provides the required spatial and spectral resolution to study the luminescence of a single QD and was the key for device characterization as well as for more fundamental studies such as the phonon-exciton interaction or the influence of the growth plane.

The single photon sources in this work have a record purity spectrum and are driven with a repetition rate up to 1 GHz. They represent a milestone towards a compact and easy-to-handle device. The study of the acoustic and optical phonon coupling to electronic states in the QDs on the most fundamental level provides an insight into the exciton-matter interaction. Finally a new kind of QDs grown on (111) GaAs open new possibilities for the generation of entangled photon pairs. In the following these main results of the work are summarized.

7.1 SUMMARY

The new custom-built micro photoluminescence and electroluminescence setup meets all demands for the characterization of single quantum dots as single photon source. The confocal laser scanning microscope ensures a spatial resolution in the order of 1 μm^2 and a positioning of the excitation and detection spot with an accuracy of better than 0.1 µm. The spectral resolution of 10 µeV, required to study the fine-structure splitting, was realized by a triple monochromator. The photon statistic can be measured with a Hanbury-Brown Twiss setup as well as in auto- as in cross-correlation. To study the ultrafast photon emission from the RCLED the typically used APDs were replaced by new superconducting single photon detectors.

The whole setup is computer controlled and can auto-adjust the signal for long-term measurements. This system with its fully automated measurements and unique high spatial, spectral and time resolution was the key for the following new measurements on single QDs.

Three types of single photon sources with increasing complexity where characterized in this work and each of them represents a milestone towards the application of single photon sources based on semiconductor quantum dots.

The **first** and simplest device is called the "poor man's single photon source" and presented in section 4.1. Here in a simple pin diode structure without any current constriction a single QD can be pumped electrically by applying a bias well below the flatband conditions. In spectrally resolved electroluminescence measurements a spatial segmentation of the lumines-

cence in dependence on the bias was observed. This result indicates the presence of preferential microscopic injection paths, resulting in a current constriction down to a single QD.

Bias dependent measurements shows two peaks of the EL intensity. This is the first observation of concurrent resonant tunneling of independent charge carriers into a QD by optical means: The holes and electrons reach the QD from the top and back contact respectively, hence they are completely uncoupled. Nevertheless, the measurements demonstrate that both couple simultaneously to the bounded exciton states in the QD. With increasing temperature the energy distribution of the charge carrier becomes broader and the resonant tunneling effects washes out to classical over band injection. The resonant tunneling excitation has been affirmed in measurements on the third type of device called RCLED.

The **second** type of devices is the single QD-LED presented in section 4.2, in which the current is controlled constricted by a sub-micron AlO_x aperture. This device represents the ultimate limit of a LED, where a single electron and hole are funneled to a single QD and recombine under the emission of a single photon. This device design allows increasing the pumping current beyond the saturation of the exciton luminescence without pumping other disturbing QDs. Hence the single photon rate of this device is limited only by the charge carrier relaxation time into the exciton bright state and the exciton life time. The efficient current constriction results in a record purity of the EL spectrum: Over a spectral range of 500 nm, covering the whole sensitivity range of Si-based detectors, only the luminescence from a single QD is observed. No GaAs bulk or wetting layer luminescence is detected. This is in contrast to previous QD based single photon emitters, were large areas are pumped and the luminescence from a single QD is selected by shadow masks. Consequently sharp luminescence lines from a single electrically pumped QD has been observed for temperatures of up to 75 K.

As required for the generation of entangled photon pairs, uncharged exciton and biexciton luminescence can be obtained from this device. The uncharged exciton emission proves the equal injection of electron and holes into the QD in the realized device design. The fine-structure splitting of 55 µeV is typical for this kind of QDs grown on (001) GaAs and preventing the entanglement yet.

The spectral purity of this device opens the way for easy and cheap application. Photon correlation measurements without spectral filtering results in a $g^{(2)}(0)$ value of 0.3 and clearly proves single photon emission. This is the first demonstration of non-classical light emission from QDs without the need of any external selection mechanism.

In another attempt to pump a single QD in a pin junction site-controlled QDs were used. In these devices the QD nucleation was controlled by nanoholes and an oxide aperture diameter of about 10 µm is sufficient to observe the luminescence from a single or only a few QDs. A clear antibunching of the emitted photon is proven in correlation measurements.

Although the site-controlled QDs were not definitely identified, these devices endorse the concept to control the position of single QDs in a pin junction.

In the **third** and most sophisticated type of devices the QD couples to a microcavity and is electrically pumped in a pin junction with a sub-micron oxide aperture. These resonant cavity light emitting diodes (RCLED) combine the advantage of the above mentioned ultimate LED with quantum cavity effects. The characterization of this highly efficient and ultra-fast single photon device is presented in section 4.3.

The coupling of the electronic states in the QDs to the optical modes of the cavity results in two fruitful effects. First, the exciton lifetime is reduced and second the photons have a preferred emission direction. Together they result in a twenty times enhanced photon rate from the RCLED in comparison to the previous single QD LED.

Although the additional DBR mirrors increase the serial resistance and consequently decrease the electrical band width, it was possible to pump the RCLED at frequency of 1 GHz with a pulse width of 350 ps. To compensate the losses and the pulse deforming in the cables and the RCLED the pulse high and low voltage has been carefully adjusted.

The optical response of the RCLED to the 1 GHz electrical signal agrees excellently with a train of 400 ps width pulses, which is close to the time resolution of the APD. Comparison of this pulse width with the typical exciton life time of 1 ns, yields a Purcell factor of about 2.5.

In pulsed photon correlation measurements the RCLED is too fast for commercial available APDs. The pulsed emission and the $g^{(2)}(0)$ value are both limited by the time resolution of the APD rather than the RCLED. A simulation of the $g^{(2)}$function taking into account the time resolution reveals the perfect single photon emission of the RCLED at a repetition rate of 1 GHz.

To study the fast photon emission new superconducting single photon detectors were implemented. A comparison of APD and superconducting detector based correlation measurements justifies the employed analysis of the $g^{(2)}$ function and proves the influence of the time resolution on the $g^{(2)}(0)$ value. Cross-correlation measurements on the exciton-biexciton cascade indicate that the exciton recombines immediately after the biexciton emission. This result is in contrast to previous assumption and measurements about the biexciton-exciton cascade: The exciton emission is expected to occur within the lifetime after the biexciton emission. The cross-correlation measurements in section 4.3.3 demonstrate bunched photon emission from the exciton within the time resolution of 130 ps of the setup. No decay of the exciton emission is visible. The bunched emission of exciton and biexciton would make time-reordering for entangled photon pairs unnecessary.

The pure spectrum of the RCLED allows increasing the operating temperature to 80 K, well above the liquid nitrogen temperature, still preserving the non-classical light characteristic. The high operating temperature makes the RCLED a promising candidate for widespread application. In fact the RCLED has been handed over to two other groups performing quantum cryptography and quantum optic experiments.

Beside the device characterization two more fundamental results were obtained in the study of single selforganized quantum dots.

Chapter 5 reports on the interaction of the QD with its solid state surrounding, which strongly influences the crucial parameters of the non-classical light emitter. Acoustic and optical phonon scattering was studied on the most fundamental level, where a single electron and hole recombine under the emission of a single photon and phonon. Due to its pure spectrum and the high out-coupling efficiency the RCLED is an ideal candidate to investigate phonon assisted luminescence, having an approximately four orders of magnitude less intensity than the zero phonon line.

Coupling of acoustic and optical phonons to excitons in single InGaAs/-GaAs quantum dots has been investigated in details experimentally and theoretically as a function of temperature. Surprisingly only GaAs bulk-type LO phonons were detected in experiments. A quantitatively correct theoretical description of the optical phonon replica is obtained by including a limited lifetime of the phonons and the dispersion of the LO phonon energy. Thus, a long discussion about the LO-phonon line shape of a single InGaAs/GaAs QD has been clarified.

Similarly a numerically correct description of the acoustic phonon wings is again based on GaAs bulk material parameters for the phonon dispersion and deformation coupling. In addition the line shape of the calculated spectra agrees with experiment only, when realistic wave functions e.g. based on 8-band-k·p-theory are used for the electron-phonon coupling matrix elements. Gaussian wave functions describing the ground state of a harmonic oscillator fail in describing high energy tails. Thus fundamental insight of importance for correct prediction of properties of non classical light sources based on semiconductor nano-structures is obtained.

Chapter 6 demonstrates that self organized InGaAs quantum dots grown on GaAs (111) substrate using droplet epitaxy have great potential for the generation of entangled photon pairs. The quantum dots show spectrally sharp luminescence lines and low spatial density. A second order correlation value of $g^2(0) = 0.3$ proves single photon emission. Since the piezoelectric field in QDs grown on (111) GaAs differs from the one of the (001) in a first step the luminescence lines had to be identified. By comparing the power dependence of the luminescence from a number of QDs a typical luminescence fingerprint was identified. One of the three luminescence lines allows the measurement of the fine-structure splitting. In polarization dependent micro photoluminescence studies a fine-structure splitting varying $\leqslant 40$ µeV down to the spectral resolution of the setup was observed. This is a pronounced reduction compared to QDs grown on (001) GaAs and makes this new kind of QD a promising candidate towards the realization of a compact source of entangled photon pairs based on semiconductor technology.

7.2 OUTLOOK

The efficient single photon source presented in this work and the new custom-built setup pave the way for a number of continuative measurements.

In this section first possible measurements and main challenges regarding single photon sources are listed. Then more fundamental experiments will be proposed.

The influence of the cavity should be investigated in more detail. Therefore, the following measurement should be performed:

- RCLEDs with increasing Q-factor should be studied. Which cavity dip width ensures the best tradeoff between device yields versus coupling strength? A higher Q-factor result in a stronger coupling but the wavelength of the QD is restricted to a smaller band and hence in a smaller number of devices the QD will be in resonance and located directly under the current aperture.

- The Purcell factor can be measured directly. Therefore, the exciton lifetime of a QD in and off resonance the cavity should be compared in pulsed EL and PL measurements. For a second comparison the top DBR mirrors could be removed to destroy the cavity.

- The ultra-fast exciton emission in the measured cross-correlation measurement is still unclear. The measurements indicate a reduced exciton life time of 70 ps. This would yield in a Purcell-factor of about 14, which is much higher than expected from calculations [Mö9, Sol01]. Possibly the picture of the X-XX cascade [Mor01] is not valid. The results presented in this work imply that the X and XX are emitted synchronously rather than one after another. Hence, the biexciton state recombines directly into the empty state und emission of two photons. This is of most interest for the suggested generation of entangled photons by time reordering [Rei08a, Avr08, Tro08]. The measurement should be repeated on a number of QDs and on the charged XX-X cascade [War09, Poe10].

- The exciton lifetime can be measured in two ways on one and the same QD: Usually it is measured in time resolved single photon counting as the response to a short laser pulse. The new HBT with high time resolution allows to measure the exciton lifetime in a cross-correlation photon measurement [Mor01]. Here, the biexciton emission triggers the start channel, hence the QD is in the exciton state. The difference between both measurements gives information about the time required to generate electrons and holes and their relaxation time to the lowest QD level. The relaxation time should differ for changing excitation energy. How does the measured exciton lifetime changes with the laser excitation energy?

- The modeling of the electromagnetic field in the RCLED should be continued. What is the best number of top/bottom DBR mirror pairs for maximum out-coupling efficiency?

For the further development of single photon sources based on self-organized QDs the following questions are of high interest:

- The out-coupling efficiency of generated photons out of the device into the detection system is the main obstacle yet. Beside the above mentioned improved cavity two other potential techniques may be used: Solid immersion lenses can be attached directly on top of the device [Sero8]. This will decrease the total reflection on the GaAs-air transition and decrease the angle of the existing light beam. Second, a direct fiber coupling may be used. If the fiber core is in close contact with the device surface, the photons will couple directly into the fiber and no GaAs-air transition will occur.

- The operating temperature of the single photon device should be increased to room temperature or at least to about 100 K, which is the minimum temperature provided by Peltier-cooling. GaN/AlN QDs demonstrate single photon emission up to 200 K [Kako6], but the growth of complex RCLED structures in this material system is very challenging. Room temperature luminescence from a single electrically driven QD has been demonstrated in the CdSe/ZnSSe system [Ario8], but no single photon emission was demonstrated yet. Both systems emit at green wavelength, which is not suitable for long distance fiber transmission. For As-based systems a dot-in-a-well structure with AlGaAs barriers may increase the confinement potential and, hence, the operating temperature.

- For long distance transmission in commercial fibers the emission wavelength of the single photon device should be shifted to the first absorption minimum at 1300 nm. This could be achieved by growing larger QDs or dot-in-a-well structures [Allo5]. Unfortunately, the quantum efficiency of single photon detectors at this wavelength is at least four times lower than in silicon based detectors for wavelength < 1000 nm. Therefore it is questionable that future quantum key distribution systems will work at wavelength larger than 1000 nm. The larger losses in the fiber can be easily compensated by the higher detection efficiency.

- The device output per wafer may be enhanced with site-controlled QDs. Unfortunately; these QDs often exhibit poor optical quality [Cheo9, Alb10a]. Probably the better way will be a more accurate control of the oxide aperture size and the use of self-organized QDs. If oxide aperture diameters with less than 0.8 µm can be fabricated reproducible the spatial density of self-organized QDs will be sufficient for a high device output. As has been demonstrated in this work it is possible to pump QDs which are not located directly beneath the aperture by increasing the pump current. Hence, usually it is not an issue to pump a QD at all, but to pump only a single one.

- The device design should be optimized for higher band width. The current device design was mainly motivated by an easy processing and high device output . The future device design should contain coplanar waveguides for injection of short current pulses.

The newly built setup with its unique spectral and time resolution paves the way to a number of more fundamental experiments:

- The influence of the exciton dark state should be investigated in detail. Therefore the intensity ratio of the X and XX in dependence on the temperature can be studied. With increased temperature the exciton switches faster between bright and dark state, hence the exciton luminescence should become more intense in comparison to the biexciton emission, if the dark state blocking exists. The ratio of the exciton/-biexciton emission rates also have large influence on the generation of entangled photons by time-reordering [Tro08].

- To overcome a possible dark-state blocking the injection of spin controlled electrons and holes could be helpful. This can be realized for example using a ZnMgS layer [Lö6] for Fe Schottky contacts [Lio5].

- The carrier injection into the QDs in a pin diode is still not clear. For lower pump current the exciton luminescence splits into three luminescence lines separated by only a few µeV. The origin of this splitting may be spin flips, but is still unclear.

The presented results for the new kind of QDs grown on (111) GaAs are only an initiation. In this work the first samples of these QDs were used. Further improvement in the growth may help to answer the following questions:

- The complete assignment of the luminescence lines to electronic complexes is still open. Does the luminescence line with a fine-structure splitting originate from an uncharged exciton X or the double charged exciton X^{++}?

- Micro-photoluminescence excitation spectroscopy on single QDs will give access to higher excited states. Thereby the difference of the piezoelectric field between QDs grown on (001) and (111) GaAs can be studied.

- For the generation of entangled photons biexcitonic complexes have to be identified. In the first samples their luminescence was overlapped by a background luminescence. New samples and sample preparation with shadow masks or micro pillars should reduce the background luminescence.

- The realization of electrically pumped devices is completely open. The oxidation process of AlGaAs will be different on this substrate orientation and has to be investigated.

Part IV

APPENDIX

BIBLIOGRAPHY

[Aic05] T. Aichele, *Detection and generation of Non-classical light states from single quantum emitters*, Dissertation, Humboldt University Berlin (2005). (Cited on page 71.)

[Ako06] N. Akopian, N. Lindner, E. Poem, Y. Berlatzky, J. Avron, D. Gershoni, B. Gerardot, and P. Petroff, *Entangled Photon Pairs from Semiconductor Quantum Dots*, Physical Review Letters **96** (13), 130501 (2006). (Cited on pages 6, 23, and 24.)

[Alb10a] F. Albert, S. Stobbe, C. Schneider, T. Heindel, S. Reitzenstein, S. Höfling, P. Lodahl, L. Worschech, and A. Forchel, *Quantum efficiency and oscillator strength of site-controlled InAs quantum dots*, Applied Physics Letters **96** (15), 151102 (2010). (Cited on pages 17, 73, and 102.)

[Alb10b] D. Albrecht, *TEM an GaAs Nanostrukturen*, Diploma, TU-Berlin (2010). (Cited on page 54.)

[All05] B. Alloing, C. Zinoni, V. Zwiller, L. H. Li, C. Monat, M. Gobet, G. Buchs, A. Fiore, E. Pelucchi, and E. Kapon, *Growth and characterization of single quantum dots emitting at 1300 nm*, Applied Physics Letters **86** (10), 101908 (2005). (Cited on page 102.)

[Ari08] R. Arians, A. Gust, T. Kummell, C. Kruse, S. Zaitsev, G. Bacher, and D. Hommel, *Electrically driven single quantum dot emitter operating at room temperature*, Applied Physics Letters **93** (17), 173506 (2008). (Cited on page 102.)

[Atk08] P. Atkinson, S. Kiravittaya, M. Benyoucef, A. Rastelli, and O. G. Schmidt, *Site-controlled growth and luminescence of InAs quantum dots using in situ Ga-assisted deoxidation of patterned substrates*, Applied Physics Letters **93** (10), 101903 (2008). (Cited on pages 17, 53, and 73.)

[Avr08] J. E. Avron, G. Bisker, D. Gershoni, N. H. Lindner, E. A. Meirom, and R. J. Warburton, *Entanglement on Demand through Time Reordering*, Physical Review Letters **100** (12), 120501 (2008). (Cited on pages 23, 81, and 101.)

[Bas92] T. Basché, W. Moerner, M. Orrit, and H. Talon, *Photon antibunching in the fluorescence of a single dye molecule trapped in a solid*, Physical Review Letters **69** (10), 1516 (1992). (Cited on page 4.)

[Bau10] A. Baumgartner, E. Stock, A. Patane, L. Eaves, and D. Bimberg, *Spatial imaging of resonant electrical injection of carriers into individual quantum dots*, submitted (2010). (Cited on page 59.)

[Bay02] M. Bayer, G. Ortner, O. Stern, A. Kuther, A. A. Gorbunov, A. Forchel, P. Hawrylak, S. Fafard, K. Hinzer, T. L. Reinecke, S. N. Walck, J. P. Reithmaier, F. Klopf, and F. Schafer, *Fine structure of neutral and charged excitons in self-assembled In(Ga)As/(Al)GaAs quantum dots*, Physical Review B **65** (19), 195315 (2002). (Cited on pages 6, 20, 21, 24, and 96.)

[Ben84] C. H. Bennet and G. Brassard, *Quantum cryptography: Public key distribution and coin tossing BT*, in *IEEE International Conference on Computers, Systems, and Signal Processing*, Bangalore, India (1984). (Cited on pages 3 and 11.)

[Ben00] O. Benson, C. Santori, M. Pelton, and Y. Yamamoto, *Regulatedand entangled photons from a single quantum dot*, Physical Review Letters **84** (11), 2513 (2000). (Cited on pages 4, 6, 22, and 23.)

[Ben05a] A. J. Bennett, D. C. Unitt, P. Atkinson, D. A. Ritchie, and A. J. Shields, *High performance single photon sources from photolithographically defined pillar microcavities*, Optics Express **13** (1), 50 (2005). (Cited on page 68.)

[Ben05b] A. J. Bennett, D. C. Unitt, P. See, A. J. Shields, P. Atkinson, K. Cooper, and D. A. Ritchie, *Electrical control of the uncertainty in the time of single photon emission events*, Phys. Rev. B **72** (3), 33316 (2005). (Cited on pages 5 and 69.)

[Bes03] G. Bester, S. Nair, and A. Zunger, *Pseudopotential calculation of the excitonic fine structure of million-atom self-assembled In1-xGaxAs/GaAs quantum dots*, Physical Review B **67** (16), 3 (2003). (Cited on page 24.)

[Bha94] A. R. Bhatt, K. W. Kim, and M. A. Stroscio, *Theoretical calculation of longitudinal-optical-phonon lifetime in GaAs*, Journal of Applied Physics **76** (6), 3905 (1994). (Cited on page 89.)

[Bim99] D. Bimberg, M. Grundmann, and N. N. Ledentsov, *Quantum Dot Heterostructures*, Wiley (1999), ISBN 0471973882. (Cited on page 3.)

[Bim08] D. Bimberg, *Semiconductor nanostructures*, Springer, Berlin; London (2008), ISBN 9783540778981 3540778985. (Cited on page 4.)

[Bim09] D. Bimberg, E. Stock, A. Lochmann, A. Schliwa, J. Tofflinger, W. Unrau, M. Munnix, S. Rodt, V. Haisler, A. Toropov, A. Bakarov, and A. Kalagin, *Quantum Dots for Single- and Entangled-Photon Emitters*, IEEE Photonics Journal **1** (1), 58 (2009). (Cited on pages 5 and 6.)

[Bor01] P. Borri, W. Langbein, S. Schneider, U. Woggon, R. Sellin, D. Ouyang, and D. Bimberg, *Ultralong Dephasing Time in InGaAs Quantum Dots*, Physical Review Letters **87** (15), 1 (2001). (Cited on page 88.)

[Braoo] M. Brasken, M. Lindberg, D. Sundholm, and J. Olsen, *Full configuration interaction calculations of electron-hole correlation effects in strain-induced quantum dots*, Physical Review B **61** (11), 7652 (2000). (Cited on page 25.)

[Bre99] J. Brendel, N. Gisin, W. Tittel, and H. Zbinden, *Pulsed Energy-Time Entangled Twin-Photon Source for Quantum Communication*, Physical Review Letters **82** (12), 2594 (1999). (Cited on page 4.)

[Bri98] H.-J. Briegel, W. Dür, J. Cirac, and P. Zoller, *Quantum Repeaters: The Role of Imperfect Local Operations in Quantum Communication*, Physical Review Letters **81** (26), 5932 (1998). (Cited on pages 3 and 14.)

[Car10] A. Carmele, M. Richter, W. W. Chow, and A. Knorr, *Antibunching of Thermal Radiation by a Room-Temperature Phonon Bath: A Numerically Solvable Model for a Strongly Interacting Light-Matter-Reservoir System*, Physical Review Letters **104** (15), 156801 (2010). (Cited on pages 5 and 6.)

[Cer72] F. Cerdeira, C. Buchenauer, F. Pollak, and M. Cardona, *Stress-Induced Shifts of First-Order Raman Frequencies of Diamond- and Zinc-Blende-Type Semiconductors*, Physical Review B **5** (2), 580 (1972). (Cited on page 31.)

[Che09] C.-C. Cheng, K. Meneou, and K. Y. Cheng, *High optical quality InAs site-controlled quantum dots grown on soft photocurable nanoimprint lithography patterned GaAs substrates*, Applied Physics Letters **95** (17), 173103 (2009). (Cited on pages 73 and 102.)

[Chi90] T. Chikyow and N. Koguchi, *MBE growth method for pyramid-shaped GaAs micro crystals on ZnSe (001) surface using Ga droplets*, Jap. J. Appl. Phys. **29** (11), L2093 (1990). (Cited on page 54.)

[Chr91] J. Christen, *Scanning cathodoluminescence microscopy: A unique approach to atomic-scale characterization of heterointerfaces and imaging of semiconductor inhomogeneities*, Journal of Vacuum Science & Technology B: Microelectronics and Nanometer Structures **9** (4), 2358 (1991). (Cited on page 35.)

[Chr03] J. Christen, T. Riemann, F. Bertram, D. Rudloff, P. Fischer, a. Kaschner, U. Haboeck, a. Hoffmann, and C. Thomsen, *Optical micro-characterization of group-III-nitrides: correlation of structural, electronic and optical properties*, Phys. stat. sol. (c) **1815** (6), 1795 (2003). (Cited on page 63.)

[Cov96] S. Cova, M. Ghioni, A. Lacaita, C. Samori, and F. Zappa, *Avalanche photodiodes and quenching circuits for single-photon detection*, Applied Optics **35** (12), 1956 (1996). (Cited on page 40.)

[Dö99] W. Dür, H.-J. Briegel, J. Cirac, and P. Zoller, *Quantum repeaters based on entanglement purification*, Physical Review A **59** (1), 169 (1999). (Cited on pages 3 and 14.)

[Dac10] M. Dachner, E. Malic, M. Richter, A. Carmele, J. Kabuss, A. Wilms, J. E. Kim, G. Hartmann, J. Wolters, U. Bandelow, and A. Knorr, *Theory of carrier and photon dynamics in quantum dot light emitters*, Physica Status Solidi (B) **247** (4), 809 (2010). (Cited on page 86.)

[Die87] F. Diedrich and H. Walther, *Nonclassical radiation of a single stored ion*, Physical Review Letters **58** (3), 203 (1987). (Cited on page 4.)

[Die88] F. Diedrich, J. Krause, G. Rempe, M. Scully, and H. Walther, *Laser experiments with single atoms as a test of basic physics*, IEEE Journal of Quantum Electronics **24** (7), 1314 (1988). (Cited on page 4.)

[Edi07] M. Ediger, G. Bester, B. D. Gerardot, A. Badolato, P. M. Petroff, K. Karrai, A. Zunger, and R. J. Warburton, *Fine Structure of Negatively and Positively Charged Excitons in Semiconductor Quantum Dots: Electron-Hole Asymmetry*, Physical Review Letters **98** (3), 36808 (2007). (Cited on pages 69, 78, and 94.)

[Eke91] A. K. Ekert, *Quantum cryptography based on Bells theorem*, Physical Review Letters **67** (6), 661 (1991). (Cited on page 13.)

[Ell06] D. J. P. Ellis, A. J. Bennett, A. J. Shields, P. Atkinson, and D. A. Ritchie, *Electrically addressing a single self-assembled quantum dot*, Applied Physics Letters **88** (13), 133509 (2006). (Cited on page 69.)

[Elm02] P. Elmer, *SPCM-AQRH Single Photon Counting Module*, Manual (2002). (Cited on pages 40 and 43.)

[Fö03] J. Förstner, C. Weber, J. Danckwerts, and A. Knorr, *Phonon-Assisted Damping of Rabi Oscillations in Semiconductor Quantum Dots*, Physical Review Letters **91** (12), 127401 (2003). (Cited on pages 5 and 86.)

[Feu08] M. Feucker, R. Seguin, S. Rodt, A. Hoffmann, and D. Bimberg, *Decay dynamics of neutral and charged excitonic complexes in single InAs/GaAs quantum dots*, Applied Physics Letters **92** (6), 63116 (2008). (Cited on pages 69 and 80.)

[Fio02] A. Fiore, J. X. Chen, and M. Ilegems, *Scaling quantum-dot light-emitting diodes to submicrometer sizes*, Applied Physics Letters **81** (10), 1756 (2002). (Cited on page 69.)

[Fry00a] P. W. Fry, I. E. Itskevich, D. J. Mowbray, M. S. Skolnick, J. J. Finley, J. A. Barker, E. P. O. Reilly, L. R. Wilson, I. A. Larkin, P. A. Maksym, M. Hopkinson, M. Al-Khafaji, J. P. R. David, A. G. Cullis, G. Hill, and J. C. Clark, *Inverted Electron-Hole Alignment in InAs-GaAs Self-Assembled Quantum Dots*, Physical Review Letters **84** (4), 733 (2000). (Cited on page 27.)

[Fryoob] P. W. Fry, I. E. Itskevich, S. R. Parnell, J. J. Finley, L. R. Wilson, K. L. Schumacher, D. J. Mowbray, M. S. Skolnick, A. G. Cullis, M. Hopkinson, J. C. Clark, and G. Hill, *Photocurrent spectroscopy of InAs/GaAs self-assembled quantum dots*, Physical Review B **62** (24), 784 (2000). (Cited on page 27.)

[Gilo7] A. Gilchrist, K. J. Resch, and A. G. White, *Quantum information: source of triggered entangled photon pairs?*, Nature **445** (7124), E4 (2007). (Cited on page 23.)

[Giso2] N. Gisin, G. Ribordy, W. Tittel, and H. Zbinden, *Quantum cryptography*, Reviews of Modern Physics **74** (1), 145 (2002). (Cited on pages 3, 5, and 11.)

[Gla63] R. Glauber, *The Quantum Theory of Optical Coherence*, Physical Review **130** (6), 2529 (1963). (Cited on page 14.)

[Gobo4] C. Gobby, Z. L. Yuan, and A. J. Shields, *Unconditionally secure quantum key distribution over 50 km of standard telecom fibre*, Electronic Letters **40** (25), 1603 (2004). (Cited on page 13.)

[Golo1] G. N. Goltsman, O. Okunev, G. Chulkova, A. Lipatov, A. Semenov, K. Smirnov, B. Voronov, A. Dzardanov, C. Williams, and R. Sobolewski, *Picosecond superconducting single-photon optical detector*, Applied Physics Letters **79** (6), 705 (2001). (Cited on page 41.)

[Gru95] M. Grundmann, O. Stier, and D. Bimberg, *InAs/GaAs pyramidal quantum dots: Strain distribution, optical phonons, and electronic structure*, Physical Review B **52** (16), 11969 (1995). (Cited on pages 23 and 31.)

[Gru97] M. Grundmann and D. Bimberg, *Theory of random population for quantum dots*, Physical Review B **55** (15), 9740 (1997). (Cited on page 66.)

[Hö4] A. Högele, S. Seidl, M. Kroner, K. Karrai, R. Warburton, B. Gerardot, and P. Petroff, *Voltage-Controlled Optics of a Quantum Dot*, Physical Review Letters **93** (21) (2004). (Cited on pages 6 and 24.)

[Hafo7] R. Hafenbrak, S. M. Ulrich, P. Michler, L. Wang, A. Rastelli, and O. G. Schmidt, *Triggered polarization-entangled photon pairs from a single quantum dot up to 30 K*, New Journal of Physics Phys. **9** (9), 315 (2007). (Cited on page 6.)

[Haio2] V. A. Haisler, F. Hopfer, R. L. Sellin, A. Lochmann, K. Fleischer, N. Esser, W. Richter, N. N. Ledentsov, D. Bimberg, C. Möller, and N. Grote, *Micro-Raman studies of vertical-cavity surface-emitting lasers with Al[sub x]O[sub y]/GaAs distributed Bragg reflectors*, Applied Physics Letters **81** (14), 2544 (2002). (Cited on pages 27 and 52.)

[Han56] R. Hanbury Brown and R. Q. Twiss, *A Test of a New Type of Stellar Interferometer on Sirius*, Nature **178** (4541), 1046 (1956). (Cited on page 45.)

[Hei96] R. Heitz, M. Grundmann, N. N. Ledentsov, L. Eckey, M. Veit, D. Bimberg, V. M. Ustinov, A. Y. Egorov, A. E. Zhukov, P. S. Kopev, and Z. I. Alferov, *Multiphonon-relaxation processes in self-organized InAs/GaAs quantum dots*, Applied Physics Letters **68** (3), 361 (1996). (Cited on page 87.)

[Hei98] R. Heitz, A. Kalburge, Q. Xie, M. Grundmann, P. Chen, A. Hoffmann, A. Madhukar, and D. Bimberg, *Excited states and energy relaxation in stacked InAs/GaAs quantum dots*, Physical Review B **57** (15), 9050 (1998). (Cited on page 92.)

[Hei99a] R. Heitz, I. Mukhametzhanov, A. Madhukar, A. Hoffmann, and D. Bimberg, *Temperature dependent optical properties of self-organized InAs/GaAs quantum dots*, Journal of Electronic Materials **28** (5), 520 (1999). (Cited on page 67.)

[Hei99b] R. Heitz, I. Mukhametzhanov, O. Stier, A. Madhukar, and D. Bimberg, *Enhanced Polar Exciton-LO-Phonon Interaction in Quantum Dots*, Physical Review Letters **83** (22), 4654 (1999). (Cited on pages 5, 30, 31, and 87.)

[Her96] M. A. Herman and H. Sitter, *Molecular Beam Epitaxy: Fundamentals and Current Status (Springer Series in Materials Science , Vol 7)*, Springer-Verlag (1996), ISBN 0387605940. (Cited on page 16.)

[Hoh07] U. Hohenester, G. Pfanner, and M. Seliger, *Phonon-Assisted Decoherence in the Production of Polarization-Entangled Photons in a Single Semiconductor Quantum Dot*, Physical Review Letters **99** (4), 1 (2007). (Cited on page 5.)

[Hou06] J. A. W. V. Houwelingen, N. Brunner, A. Beveratos, H. Zbinden, and N. Gisin, *Quantum Teleportation with a Three-Bell-State Analyzer*, Physical Review Letters **130502**, 1 (2006). (Cited on page 14.)

[Hua50] K. Huang and A. Rhys, *Theory of Light Absorption and Non-Radiative Transitions in F-Centres*, Proceedings of the Royal Society A: Mathematical, Physical and Engineering Sciences **204** (1078), 406 (1950). (Cited on pages 30 and 87.)

[Iba08] H. Ibach and H. Lüth, *Festkörperphysik: Einführung in die Grundlagen (Springer-Lehrbuch) (German Edition)*, Springer (2008), ISBN 354085794X. (Cited on page 27.)

[Ili00] K. S. Ilin, M. Lindgren, M. Currie, A. D. Semenov, G. N. Goltsman, R. Sobolewski, S. I. Cherednichenko, and E. M. Gershenzon, *Picosecond hot-electron energy relaxation in NbN superconducting photodetectors*, Applied Physics Letters **76** (19), 2752 (2000). (Cited on page 41.)

[Ish00] T. Ishikawa, T. Nishimura, S. Kohmoto, and K, *Site-controlled InAs single quantum-dot structures on GaAs surfaces patterned by in situ*

electron-beam lithography, Applied Physics Letters **76** (2), 167 (2000). (Cited on page 17.)

[Kad96] A. M. Kadin and M. W. Johnson, *Nonequilibrium photon-induced hotspot: A new mechanism for photodetection in ultrathin metallic films*, Applied Physics Letters **69** (25), 3938 (1996). (Cited on page 41.)

[Kako6] S. Kako, C. Santori, K. Hoshino, S. Götzinger, Y. Yamamoto, and Y. Arakawa, *A gallium nitride single-photon source operating at 200 K.*, Nature materials **5** (11), 887 (2006). (Cited on page 102.)

[Kavo8] A. Kavokin, J. J. Baumberg, G. Malpuech, and F. P. Laussy, *Microcavities (Series on Semiconductor Science and Technology)*, Oxford University Press, USA (2008), ISBN 0199228949. (Cited on page 31.)

[Kieo3] G. Kieszlilich, A. Wacker, E. Schöll, S. A. Vitusevich, A. E. Belyaev, S. V. Danylyuk, A. Förster, N. Klein, and M. Henini, *Nonlinear charging effect of quantum dots in a p-i-n diode*, Physical Review B **68** (12), 125331 (2003). (Cited on page 63.)

[Kim77] H. Kimble, M. Dagenais, and L. Mandel, *Photon Antibunching in Resonance Fluorescence*, Physical Review Letters **39** (11), 691 (1977). (Cited on pages 4 and 5.)

[Kim99] J. Kim, O. Benson, H. Kan, and Y. Yamamoto, *A single-photon turnstile device*, Nature **397**, 500 (1999). (Cited on pages 4 and 20.)

[Kin10] C. Kindel, *The Multi-Excitonic Model of Single QDs*, Private communication (2010). (Cited on page 71.)

[Kiro6] S. Kiravittaya, A. Rastelli, and O. G. Schmidt, *Photoluminescence from seeded three-dimensional InAs/GaAs quantum-dot crystals*, Applied Physics Letters **88** (4), 43112 (2006). (Cited on page 73.)

[Kito5] J. Kitaygorsky, J. Zhang, A. Verevkin, A. Sergeev, A. Korneev, V. Matvienko, P. Kouminov, K. Smirnov, B. Voronov, G. Gol'tsman, and R. Sobolewski, *Origin of dark counts in nanostructured NbN single-photon detectors*, IEEE Transactions on Applied Superconductivity **15** (2), 545 (2005). (Cited on page 43.)

[Kle10] T. Kleinjung, K. Aoki, J. Franke, A. Lenstra, E. Thomé, J. Bos, P. Gaudry, A. Kruppa, P. Montgomery, D. Osvik, and Others, *Factorization of a 768-bit RSA modulus*, pp. 333–350, Springer Berlin Heidelberg (2010), ISBN 978-3-642-14622-0. (Cited on page 3.)

[Kowo5] K. Kowalik, O. Krebs, A. Lemaitre, S. Laurent, P. Senellart, P. Voisin, and J. A. Gaj, *Influence of an in-plane electric field on exciton fine structure in InAs-GaAs self-assembled quantum dots*, Applied Physics Letters **86** (4), 41907 (2005). (Cited on pages 6 and 24.)

[Kruo2] B. Krummheuer, V. M. Axt, and T. Kuhn, *Theory of pure dephasing and the resulting absorption line shape in semiconductor quantum dots*, Physical Review B **65** (19), 195313 (2002). (Cited on pages 5 and 86.)

[Kuroo] C. Kurtsiefer, S. Mayer, P. Zarda, and H. Weinfurter, *Stable Solid-State Source of Single Photons*, Physical Review Letters **85** (2), 290 (2000). (Cited on page 4.)

[Lö5] A. Löffler, J. P. Reithmaier, G. Sek, C. Hofmann, S. Reitzenstein, M. Kamp, and A. Forchel, *Semiconductor quantum dot microcavity pillars with high-quality factors and enlarged dot dimensions*, Applied Physics Letters **86** (11), 111105 (2005). (Cited on page 5.)

[Lö6] W. Löffler, D. Tröndle, J. Fallert, H. Kalt, D. Litvinov, D. Gerthsen, J. Lupaca-Schomber, T. Passow, B. Daniel, J. Kvietkova, M. Grün, C. Klingshirn, and M. Hetterich, *Electrical spin injection from ZnMnSe into InGaAs quantum wells and quantum dots*, Applied Physics Letters **88** (6), 062105 (2006). (Cited on page 103.)

[Lan67] J. Langer and V. Ambegaokar, *Intrinsic Resistive Transition in Narrow Superconducting Channels*, Physical Review **164** (2), 498 (1967). (Cited on page 43.)

[Lan87] Landolt and Börnstein, *Semiconductors: Intrinsic Properties of Group IV Elements and II-V, II-VI and I-VII Compounds*, volume III/22a, Springer, Berlin (1987). (Cited on pages 19, 30, 86, and 87.)

[Lano4] W. Langbein, P. Borri, U. Woggon, V. Stavarache, D. Reuter, and A. Wieck, *Control of fine-structure splitting and biexciton binding in InxGa1-xAs quantum dots by annealing*, Physical Review B **69** (16), 1 (2004). (Cited on pages 6 and 24.)

[Lauo8] F. Laussy, E. del Valle, and C. Tejedor, *Strong Coupling of Quantum Dots in Microcavities*, Physical Review Letters **101** (8), 1 (2008). (Cited on page 5.)

[Leo94] D. Leonard, K. Pond, and P. M. Petroff, *Critical layer thickness for self-assembled InAs islands on GaAs*, Physical Review B **50** (16), 11687 (1994). (Cited on pages 17 and 51.)

[Leooo] K. Leosson, J. Jensen, J. Hvam, and W. Langbein, *Linewidth Statistics of Single InGaAs Quantum Dot Photoluminescence Lines*, Phys. stat. sol. (b) **221** (1), 49 (2000). (Cited on page 18.)

[Lio5] C. H. Li, G. Kioseoglou, O. M. J. vant Erve, M. E. Ware, D. Gammon, R. M. Stroud, B. T. Jonker, R. Mallory, M. Yasar, and A. Petrou, *Electrical spin pumping of quantum dots at room temperature*, Applied Physics Letters **86** (13), 132503 (2005). (Cited on page 103.)

[Lino6] N. H. Lindner, J. Avron, N. Akopian, and D. Gershoni, *A comment on "A semiconductor source of entangled photons "*, arXiv:quant-ph/0601200v1 (1), 6 (2006). (Cited on page 23.)

[Lob98] C. Lobo and R. Leon, *InGaAs island shapes and adatom migration behavior on (100), (110), (111), and (311) GaAs surfaces*, J. Applied Physics **83** (8), 4168 (1998). (Cited on page 24.)

[Loco9] A. Lochmann, E. Stock, J. A. Tofflinger, W. Unrau, A. Toropov, A. Bakarov, V. Haisler, and D. Bimberg, *Electrically pumped, microcavity based single photon source driven at 1 GHz*, Electronic Letters **45** (11), 566 (2009). (Cited on page 5.)

[Lou05] B. Lounis and M. Orrit, *Single-photon sources*, Reports on Progress in Physics **68** (5), 1129 (2005). (Cited on page 4.)

[Mö9] M. C. Münnix, A. Lochmann, D. Bimberg, and V. A. Haisler, *Modeling Highly Efficient RCLED-Type Quantum-Dot-Based Single Photon Emitters*, IEEE Journal of Quantum Electronics **45** (9), 1084 (2009). (Cited on pages 34, 76, and 101.)

[Mar01] J. Marquez, L. Geelhaar, and K. Jacobi, *Atomically resolved structure of InAs quantum dots*, Applied Physics Letters **78** (16), 2309 (2001). (Cited on page 17.)

[Mar07] A. Marent, M. Geller, A. Schliwa, D. Feise, K. Pötschke, D. Bimberg, N. Akccay, and N. Öncan, *10 years extrapolated hole storage time in GaSb/AlAs quantum dots*, Applied Physics Letters **91** (24), 242109 (2007). (Cited on page 16.)

[May03] V. May and O. Kühn, *Charge and Energy Transfer Dynamics in Molecular Systems*, Wiley-VCH Verlag GmbH, Weinheim, Germany (2003), ISBN 9783527602575. (Cited on page 87.)

[Meh07] M. Mehta, D. Reuter, A. Melnikov, A. D. Wieck, and A. Remhof, *Focused ion beam implantation induced site-selective growth of InAs quantum dots*, Applied Physics Letters **91** (12), 123108 (2007). (Cited on page 17.)

[Mic00a] P. Michler, a. Imamoglu, M. Mason, P. Carson, G. Strouse, and S. Buratto, *Quantum correlation among photons from a single quantum dot at room temperature*, Nature **406** (6799), 968 (2000). (Cited on page 4.)

[Mic00b] P. Michler, A. Kiraz, C. Becher, W. V. Schoenfeld, P. M. Petroff, L. Zhang, E. Hu, and A. Imamoglu, *A quantum dot single-photon turnstile device.*, Science **290** (5500), 2282 (2000). (Cited on pages 4, 5, and 20.)

[Mic03] P. Michler, *Single Quantum Dots*, Springer Verlag, Berlin Heidelberg (2003). (Cited on page 80.)

[Mic10] P. Michler, *Single Quantum Dots: Fundamentals, Applications and New Concepts (Topics in Applied Physics)*, Springer (2010), ISBN 3642057314. (Cited on pages 5 and 69.)

[Mil85] D. Miller, D. Chemla, T. Damen, A. Gossard, W. Wiegmann, T. Wood, and C. Burrus, *Electric field dependence of optical absorption near the band gap of quantum-well structures*, Physical Review B **32** (2), 1043 (1985). (Cited on page 27.)

[Mino1] A. Minnaert, A. Silov, W. van Der Vleuten, J. Haverkort, and J. Wolter, *Fröhlich interaction in InAs/GaAs self-assembled quantum dots*, Physical Review B **63** (7), 1 (2001). (Cited on page 30.)

[Moro1] E. Moreau, I. Robert, L. Manin, V. Thierry-Mieg, Eacute, J. M. Rard, and I. Abram, *Quantum Cascade of Photons in Semiconductor Quantum Dots*, Physical Review Letters **87** (18), 183601 (2001). (Cited on pages 80, 81, and 101.)

[Mulo6] E. A. Muljarov and R. Zimmermann, *Comment on "Dephasing Times in Quantum Dots due to Elastic LO Phonon-Carrier Collisions"*, Physical Review Letters **96** (1), 19701 (2006). (Cited on page 6.)

[Mulo7] E. A. Muljarov and R. Zimmermann, *Exciton Dephasing in Quantum Dots due to LO-Phonon Coupling: An Exactly Solvable Model*, Physical Review Letters **98** (18), 187401 (2007). (Cited on page 6.)

[Nom92] S. Nomura and T. Kobayashi, *Exciton-LO-phonon couplings in spherical semiconductor microcrystallites*, Physical Review B **45** (3), 1305 (1992). (Cited on pages 31 and 87.)

[Nom10] M. Nomura, N. Kumagai, S. Iwamoto, Y. Ota, and Y. Arakawa, *Laser oscillation in a strongly coupled single-quantum-dot nanocavity system*, Nature Physics **6** (4), 279 (2010). (Cited on page 33.)

[Ou88] Z. Y. Ou and L. Mandel, *Violation of Bell's Inequality and Classical Probability in a Two-Photon Correlation Experiment*, Physical Review Letters **61** (1), 50 (1988). (Cited on page 4.)

[Pee09] M. Peev, C. Pacher, R. Alleaume, C. Barreiro, J. Bouda, W. Boxleitner, T. Debuisschert, E. Diamanti, M. Dianati, J. F. Dynes, S. Fasel, S. Fossier, M. Fürst, J.-D. Gautier, O. Gay, N. Gisin, P. Grangier, A. Happe, Y. Hasani, M. Hentschel, H. Hübel, G. Humer, T. Länger, M. Legre, R. Lieger, J. Lodewyck, T. Lorünser, N. Lütkenhaus, A. Marhold, T. Matyus, O. Maurhart, L. Monat, S. Nauerth, J.-B. Page, A. Poppe, E. Querasser, G. Ribordy, S. Robyr, L. Salvail, A. W. Sharpe, A. J. Shields, D. Stucki, M. Suda, C. Tamas, T. Themel, R. T. Thew, Y. Thoma, A. Treiber, P. Trinkler, R. Tualle-Brouri, F. Vannel, N. Walenta, H. Weier, H. Weinfurter, I. Wimberger, Z. L. Yuan, H. Zbinden, and A. Zeilinger, *The SECOQC quantum key distribution network in Vienna*, New Journal of Physics **11** (7), 075001 (2009). (Cited on page 3.)

[Pelo2] M. Pelton, C. Santori, J. Vuckovic, B. Zhang, G. S. Solomon, J. Plant, and Y. Yamamoto, *Efficient Source of Single Photons: A Single Quantum Dot in a Micropost Microcavity*, Physical Review Letters **89** (23), 1 (2002). (Cited on page 5.)

[Poe10] E. Poem, Y. Kodriano, C. Tradonsky, B. D. Gerardot, P. M. Petroff, and D. Gershoni, *Radiative cascades from charged semiconductor quantum dots*, Physical Review B **81** (8), 85306 (2010). (Cited on page 101.)

[Poh84] D. W. Pohl, W. Denk, and M. Lanz, *Optical stethoscopy: Image recording with resolution λ/20*, Applied Physics Letters **44** (7), 651 (1984). (Cited on page 35.)

[Pov04] M. Povolotskyi, A. D. Carlo, and S. Birner, *Electronic and optical properties of [N11] grown nanostructures*, Phys. stat. sol. (c) **1** (6), 1511 (2004). (Cited on page 6.)

[Pur46] E. Purcell, H. Torrey, and R. Pound, *Resonance Absorption by Nuclear Magnetic Moments in a Solid*, Physical Review **69** (1-2), 37 (1946). (Cited on pages 5 and 33.)

[Qiu09] C. Qiu and T. Qian, *Numerical study of the phase slips in ultrathin doubly connected superconducting cylinders*, Physical Review B **79** (5), 1 (2009). (Cited on page 43.)

[Rei04] J. P. Reithmaier, G. Sek, A. Löffler, C. Hofmann, S. Kuhn, S. Reitzenstein, L. V. Keldysh, V. D. Kulakovskii, T. L. Reinecke, and A. Forchel, *Strong coupling in a single quantum dot-semiconductor microcavity system.*, Nature **432** (7014), 197 (2004). (Cited on pages 5 and 33.)

[Rei08a] M. E. Reimer, J. Lefebvre, J. Lapointe, P. J. Poole, and G. C. Aers, *Voltage Induced Hidden Symmetry and Photon Entanglement Generation in a Single, Site-Selected Quantum Dot*, arXiv:0706.1075 pp. 1–4 (2008). (Cited on pages 23, 81, and 101.)

[Rei08b] M. Reischle, G. J. Beirne, R. Rossbach, M. Jetter, and P. Michler, *Influence of the Dark Exciton State on the Optical and Quantum Optical Properties of Single Quantum Dots*, Physical Review Letters **101** (14), 146402 (2008). (Cited on pages 21 and 83.)

[Ren05] R. Renner, N. Gisin, and B. Kraus, *Information-theoretic security proof for quantum-key-distribution protocols*, Physical Review A **72** (1), 1 (2005). (Cited on pages 12 and 13.)

[Riv78] R. L. Rivest, A. Shamir, and L. M. Adleman, *A Method for Obtaining Digital Signatures and Public-Key Cryptosystems*, CACM **21** (2), 120 (1978). (Cited on page 3.)

[Rod05] S. Rodt, A. Schliwa, K. Potschke, F. Guffarth, and D. Bimberg, *Correlation of structural and few-particle properties of self-organized InAs/GaAs quantum dots*, Physical Review B **71** (15), 155325 (2005). (Cited on pages 19, 20, 23, and 93.)

[Ros08] M. Rossetti, T. M. Smeeton, W. S. Tan, M. Kauer, S. E. Hooper, J. Heffernan, H. Xiu, and C. J. Humphreys, *Degradation of InGaN/GaN laser diodes analyzed by microphotoluminescence and microelectroluminescence mappings*, Applied Physics Letters **92** (15), 151110 (2008). (Cited on page 64.)

[Rud06] S. Rudin, T. L. Reinecke, and M. Bayer, *Temperature dependence of optical linewidth in single InAs quantum dots*, Physical Review B **74** (16), 161305 (2006). (Cited on page 89.)

[Sal10] C. L. Salter, R. M. Stevenson, I. Farrer, C. A. Nicoll, D. A. Ritchie, and A. J. Shields, *An entangled-light-emitting diode*, Nature **465** (7298), 594 (2010). (Cited on page 23.)

[Sca04] V. Scarani, H. de Riedmatten, I. Marcikic, H. Zbinden, and N. Gisin, *Four-photon correction in two-photon Bell experiments*, The European Physical Journal D **32** (1), 129 (2004). (Cited on page 4.)

[Sca08] V. Scarani, H. Bechmann-Pasquinucci, N. J. Cerf, M. Dusek, N. Lutkenhaus, and M. Peev, *The Security of Practical Quantum Key Distribution*, (2008). (Cited on page 13.)

[Sca09] V. Scarani, H. Bechmann-Pasquinucci, and N. Cerf, *The security of practical quantum key distribution*, Reviews of Modern Physics **81**, 1301 (2009). (Cited on page 11.)

[Sch07] A. Schliwa, M. Winkelnkemper, and D. Bimberg, *Impact of size, shape, and composition on piezoelectric effects and electronic properties of In(Ga)As/GaAs quantum dots*, Physical Review B **76** (20), 205317 (2007). (Cited on pages 18, 23, and 86.)

[Sch08] A. Schliwa, M. Winkelnkemper, and D. Bimberg, *Generation von verschränkten Photonenpaaren mittels Quantenpunkten, die auf einem (111)-Zincblende-Substrat gewachsen werden*, German Patent Application Nr. 10 2008 036 400.2 p. 10 2008 036 400.2 (2008). (Cited on pages 6 and 91.)

[Sch09] A. Schliwa, M. Winkelnkemper, A. Lochmann, E. Stock, and D. Bimberg, *(111)-Grown In(Ga)As/GaAs Quantum dots as ideal source of entangled photon pairs*, Physical Review B **80**, 161307 (2009). (Cited on pages 6, 23, 24, 25, and 91.)

[Seb02] K. Sebald, P. Michler, T. Passow, D. Hommel, G. Bacher, and A. Forchel, *Single-photon emission of CdSe quantum dots at temperatures up to 200 K*, Applied Physics Letters **81** (16), 2920 (2002). (Cited on page 82.)

[Seg05] R. Seguin, A. Schliwa, S. Rodt, K. Potschke, U. W. Pohl, and D. Bimberg, *Size-Dependent Fine-Structure Splitting in Self-Organized InAs/GaAs Quantum Dots*, Physical Review Letters **95** (25), 257402 (2005). (Cited on pages 6, 24, 69, and 96.)

[Seg06] R. Seguin, A. Schliwa, T. D. Germann, S. Rodt, K. Potschke, A. Strittmatter, U. W. Pohl, D. Bimberg, M. Winkelnkemper, T. Hammerschmidt, and P. Kratzer, *Control of fine-structure splitting and excitonic binding energies in selected individual InAs/GaAs quantum dots*, Applied Physics Letters **89** (26), 263103 (2006). (Cited on pages 6 and 24.)

[Sego8] R. Seguin, *Electronic Fine Structure and Recombination Dynamics in Single InAs Quantum Dots*, Dissertation, TU-Berlin (2008). [http://nbn-resolving.de/urn:nbn:de:kobv:83-opus-17658] (Cited on page 20.)

[Seio6] S. Seidl, M. Kroner, A. Hogele, K. Karrai, R. J. Warburton, A. Badolato, and P. M. Petroff, *Effect of uniaxial stress on excitons in a self-assembled quantum dot*, Applied Physics Letters **88** (20), 203113 (2006). (Cited on pages 6 and 24.)

[Sero8] K. a. Serrels, E. Ramsay, P. a. Dalgarno, B. Gerardot, J. O'Connor, R. H. Hadfield, R. Warburton, and D. Reid, *Solid immersion lens applications for nanophotonic devices*, Journal of Nanophotonics **2** (1), 021854 (2008). (Cited on page 102.)

[Sha49] C. Shannon, *Communication theory of secrecy systems*, Bell system technical journal **28** (4), 656 (1949). (Cited on pages 3 and 11.)

[Shio7] A. J. Shields, *Semiconductor quantum light sources*, Nature Photonics **1** (1), 215 (2007). (Cited on page 5.)

[Sieo9] E. Siebert, T. Warming, A. Schliwa, E. Stock, M. Winkelnkemper, S. Rodt, and D. Bimberg, *Spectroscopic access to single-hole energies in InAs/GaAs quantum dots*, Physical Review B **79** (20), 205321 (2009). (Cited on page 92.)

[Sinoo] S. Singh, *The Code Book: The Secret History of Codes & Code-Breaking*, Fourth Estate Limited (2000), ISBN 0007635745. (Cited on page 3.)

[Sino9] R. Singh and G. Bester, *Nanowire Quantum Dots as an Ideal Source of Entangled Photon Pairs*, Physical Review Letters **103**, 63601 (2009). (Cited on page 6.)

[Solo1] G. S. Solomon, M. Pelton, and Y. Yamamoto, *Single-mode Spontaneous Emission from a Single Quantum Dot in a Three-Dimensional Microcavity*, Physical Review Letters **86** (17), 3903 (2001). (Cited on pages 33 and 101.)

[Solo2] G. S. Solomon, *Quantum cryptography with a photon turnstile*, Lecture Notes in Computer Science **420** (December), 187904 (2002). (Cited on page 20.)

[Sono5] H. Z. Song, T. Usuki, S. Hirose, K. Takemoto, Y. Nakata, N. Yokoyama, and Y. Sakuma, *Site-controlled photoluminescence at telecommunication wavelength from InAs/InP quantum dots*, Applied Physics Letters **86** (11), 113118 (2005). (Cited on page 17.)

[Steo5] R. M. Stevenson, R. J. Young, P. See, C. E. Norman, A. J. Shields, P. Atkinson, and D. a. Ritchie, *Strong directional dependence of single-quantum-dot fine structure*, Applied Physics Letters **87** (13), 133120 (2005). (Cited on page 96.)

[Steo6] R. M. Stevenson, R. J. Young, P. Atkinson, K. Cooper, D. A. Ritchie, and A. J. Shields, *A semiconductor source of triggered entangled photon pairs.*, Nature **439** (7073), 179 (2006). (Cited on pages 6, 23, and 24.)

[Steo7] R. M. Stevenson, R. J. Young, P. Atkinson, K. Cooper, D. A. Ritchie, and A. J. Shields, *Quantum Information: Source of triggered entangled photon pairs? (Reply)*, Nature **445** (7124), E5 (2007). (Cited on page 23.)

[Steo8] R. M. Stevenson, A. J. Hudson, A. J. Bennett, R. J. Young, C. A. Nicoll, D. A. Ritchie, and A. J. Shields, *Evolution of Entanglement Between Distinguishable Light States*, Physical Review Letters **101** (17), 170501 (2008). (Cited on page 23.)

[Sti99] O. Stier, M. Grundmann, and D. Bimberg, *Electronic and optical properties of strained quantum dots modeled by 8-band-k.p theory*, Physical Review B **59**, 5688 (1999). (Cited on pages 3, 18, 19, and 23.)

[Str90] D. Strauch and B. Dorner, *Phonon dispersion in GaAs*, Journal of Physics: Condensed Matter **2**, 1457 (1990). (Cited on page 29.)

[Str99] G. B. Stringfellow, *Organometallic Vapor-Phase Epitaxy: Theory and Practice*, Acad. Pr., Boston, Boston, 2nd editio edition (1999). (Cited on page 16.)

[Stro1] M. A. Stroscio and M. Dutta, *Phonons in Nanostructures*, Cambridge University Press (2001), ISBN 0521792797. (Cited on page 27.)

[Sug95] Y. Sugiyama, Y. Sakuma, S. Muto, and N. Yokoyama, *Novel InGaAs/-GaAs quantum dot structures formed in tetrahedral-shaped recesses on (111)B GaAs substrate using metalorganic vapor phase epitaxy*, Applied Physics Letters **67** (2), 256 (1995). (Cited on pages 6 and 92.)

[Sze98] S. M. Sze, *Modern Semiconductor Device Physics*, John Wiley & Sons, Inc., New York, 1 edition (1998). (Cited on pages 26 and 63.)

[Töo] V. Türck, S. Rodt, O. Stier, R. Heitz, R. Engelhardt, U. Pohl, D. Bimberg, and R. Steingrüber, *Effect of random field fluctuations on excitonic transitions of individual CdSe quantum dots*, Physical Review B **61** (15), 9944 (2000). (Cited on pages 18, 69, and 94.)

[Tar10] G. Tarel and V. Savona, *Linear spectrum of a quantum dot coupled to a nanocavity*, Physical Review B **81** (7) (2010). (Cited on page 5.)

[Thoo1] R. Thompson, R. Stevenson, a. Shields, I. Farrer, C. Lobo, D. Ritchie, M. Leadbeater, and M. Pepper, *Single-photon emission from exciton complexes in individual quantum dots*, Physical Review B **64** (20), 1 (2001). (Cited on pages 69 and 80.)

[Thu95] P. Thurian, G. Kaczmarczyk, H. Siegle, R. Heitz, A. Hoffmann, I. Broser, B. Meyer, R. Hoffbauer, and U. Scherz, *Local Vibrational Modes of 3d Elements in Wurtzite Type ZnO and GaN Crystals*, Materials Science Forum **196-201**, 1571 (1995). (Cited on page 31.)

[Troo8] F. Troiani and C. Tejedor, *Entangled photon pairs from a quantum-dot cascade decay: The effect of time reordering*, Physical Review B **78** (15), 155305 (2008). (Cited on pages 23, 101, and 103.)

[Tsa98] F. Y. Tsai and C. P. Lee, *InGaAs/GaAs quantum dots on (111)B GaAs substrates*, J. Applied Physics **84** (5), 2624 (1998). (Cited on pages 6 and 92.)

[Turo6] L. Turyanska, A. Baumgartner, A. Chaggar, A. Patane, L. Eaves, and M. Henini, *Sharp-line electroluminescence from individual quantum dots by resonant tunneling injection of carriers*, Applied Physics Letters **89** (9), 92106 (2006). (Cited on page 50.)

[Ulh10] A. Ulhaq, S. Ates, S. Weiler, S. Ulrich, S. Reitzenstein, A. Löffler, S. Höfling, L. Worschech, A. Forchel, and P. Michler, *Linewidth broadening and emission saturation of a resonantly excited quantum dot monitored via an off-resonant cavity mode*, Physical Review B **82** (4) (2010). (Cited on page 5.)

[Usko0] A. Uskov, a. Jauho, B. Tromborg, J. Mork, and R. Lang, *Dephasing times in quantum dots due to elastic LO phonon-carrier collisions*, Physical Review Letters **85** (7), 1516 (2000). (Cited on page 6.)

[Usko6] A. Uskov, A. Jauho, B. Tromborg, J. Mø rk, and R. Lang, *Uskov et al. Reply:*, Physical Review Letters **96** (1), 237401 (2006). (Cited on page 6.)

[Vero2] A. Verevkin, J. Zhang, R. Sobolewski, A. Lipatov, O. Okunev, G. Chulkova, A. Korneev, K. Smirnov, G. N. Gol'tsman, and A. Semenov, *Detection efficiency of large-active-area NbN single-photon superconducting detectors in the ultraviolet to near-infrared range*, Applied Physics Letters **80** (25), 4687 (2002). (Cited on pages 41 and 43.)

[Wako2] E. Waks, K. Inoue, C. Santori, D. Fattal, J. Vuckovic, G. S. Solomon, and Y. Yamamoto, *Secure communication: quantum cryptography with a photon turnstile.*, Nature **420** (6917), 762 (2002). (Cited on pages 3 and 13.)

[Wan99] L.-W. Wang, J. Kim, and A. Zunger, *Electronic structures of [110]-faceted self-assembled pyramidal InAs/GaAs quantum dots*, Physical Review B **59** (8), 5678 (1999). (Cited on page 18.)

[War97] R. J. Warburton, C. S. Durr, K. Karrai, J. P. Kotthaus, G. Medeiros-Ribeiro, and P. M. Petroff, *Charged excitons in self-assembled semiconductor quantum dots*, Physical Review Letters **79** (20), 5282 (1997). (Cited on page 94.)

[Waro9] T. Warming, E. Siebert, A. Schliwa, E. Stock, R. Zimmermann, and D. Bimberg, *Hole-hole and electron-hole exchange interactions in single InAs/GaAs quantum dots*, Physical Review B **79** (12), 125316 (2009). (Cited on pages 24, 78, 96, and 101.)

[Wie83] S. Wiesner, *A special issue on cryptography*, ACM SIGACT News **15** (1983). (Cited on page 11.)

[Win99] D. W. Winston, *www.simwindows.com* (1999). [www.simwindows.com] (Cited on page 77.)

[Win06] M. Winkelnkemper, A. Schliwa, and D. Bimberg, *Interrelation of structural and electronic properties in InGaN/GaN quantum dots using an eight-band kp model*, Physical Review B **74** (15) (2006). (Cited on page 25.)

[Woo82] W. K. Wootters and W. H. Zurek, *A single quantum cannot be cloned*, Nature **299** (5886), 802 (1982). (Cited on pages 3 and 13.)

[Yos04] T. Yoshie, A. Scherer, J. Hendrickson, G. Khitrova, H. M. Gibbs, G. Rupper, C. Ell, O. B. Shchekin, and D. G. Deppe, *Vacuum Rabi splitting with a single quantum dot in a photonic crystal nanocavity.*, Nature **432** (7014), 200 (2004). (Cited on page 33.)

[You05] R. J. Young, R. M. Stevenson, a. J. Shields, P. Atkinson, K. Cooper, D. a. Ritchie, K. M. Groom, a. I. Tartakovskii, and M. S. Skolnick, *Inversion of exciton level splitting in quantum dots*, Physical Review B **72** (11), 1 (2005). (Cited on pages 6 and 24.)

[Yua02] Z. Yuan, B. E. Kardynal, R. M. Stevenson, A. J. Shields, C. J. Lobo, K. Cooper, N. S. Beattie, D. A. Ritchie, and M. Pepper, *Electrically driven single-photon source.*, Science **295** (5552), 102 (2002). (Cited on pages 4, 68, and 69.)

[Yua10] Z. L. Yuan, A. W. Sharpe, J. F. Dynes, A. R. Dixon, and A. J. Shields, *Multi-gigahertz operation of photon counting InGaAs avalanche photodiodes*, Applied Physics Letters **96** (7), 71101 (2010). (Cited on page 41.)

[Zim02] R. Zimmermann and E. Runge, *No Title*, in *Proc. 26th ICPS Edinburgh*, Edinburgh, UK (2002). (Cited on page 86.)

[Zin04] C. Zinoni, B. Alloing, C. Paranthoen, and A. Fiore, *Three-dimensional wavelength-scale confinement in quantum dot microcavity light-emitting diodes*, Applied Physics Letters **85** (12), 2178 (2004). (Cited on page 69.)

ORIGIN OF DATA IN FIGURES

FIG 4.1 on page 60 Sample NU2588F Diode M4 Spot C folder "2008/SpotC/map-scan" measured 14.03.2008

FIG 4.2 on page 61 Sample NU2588F Diode M4 Spot C 15 K: file "long-fine.dat" measured 14.03.2008; 60 K. "Voltagescan60K Additiv975nm" measured 28.05.2008

FIG 4.3 on page 62 Sample NU2588F Diode M4 Spot C file "llong-fine specktra at 1p315" measured 14.03.2008

FIG 4.5 on page 66 Sample NP1271-4 field 9-6 left panel: files "D3-2I14-9miA3-8V.dat" and "EL-15miA.dat" measured 21.04.2005 and 18.05.2005 respectively. Right panel:diode 32 and 33 files "D3-2I15miA-14K" and "I15miA3,8V.dat" measured 21. and 22.04.2005 respectively

FIG 4.5 on page 66 Sample NP1271-4 field 9-6 folder "feld9-6" measured 21.04.2005

FIG 4.6 on page 68 Sample Now1689, (a): file "Now1689-10K-1000mW--OD2.dat" measured 22.01.2005, (b) folder "uPL-Mesa13_Loch_A" (c) folder "30-04-2006" measured 30.04.2006

FIG 4.7 on page 69 Sample Now1689 field 12-8 device 32, folder "D32\09-04-2006\Neu" measured 09.04.2006

FIG 4.8 on page 70 Sample Now1689 field 12-8 device 32 file "smoothed.dat" measured 19.04.2006

FIG 4.9 on page 72 Sample AT64811 field 2417 device 8 file "EL_overview_-2p25V_20muA_1s" and "VScan_HD_add930nm_10s.vscan" measured 08.10.2009

FIG 4.10 on page 74 Sample AT64811 field 2418 device 3 left panel: file "overview_EL_maxofmap_2p08V_620nA_1s" measured 16.09.2009 right panel: file "corr_2p05V_450nA_10Std.cor" measured 30.09.2009

FIG 4.11 on page 75 Sample NowRC147 field 2519 diode 7 spectra: file "overview_pulsedEL_H1p72V_Lop35V_P1poons_Wop35ns_1s" measured 24.02.2009 EL image:

FIG 4.12 on page 76 Sample NowRC147 field 2519 diode 7 file "VScan_965nm_1s_add.vscan" measured 19.02.2009

FIG 4.13 on page 78 Sample NowRC147 field 2519 diode 7 Left: file "EL_1p49V_7p4nA_10s_add_pol90_above-obj" and " EL_1p49V_7p4nA_-10s_add_polo_above-obj" measured 20.02.2009 Right: file "VScan-Add fein.vscan" measured 10.05.2010

NOMENCLATURE

AFM Atomic force microscopy

APD Avalanche photodiodes

CCD Charged coupled device

CLSM confocale laser scanning microscope

DOS Density of states

EL Electroluminescence

FSS Finestructure splitting

FWHM Full widht of half maximum

HBT Hanbury-Brown Twiss

IRF instrumental response function

jc critical current density

LCVR Liquid crystal retarder

LED Light emitting diode

MBE Moleculare beam epitaxy

MCP Multichannel plate

MOCVD Metall organic chemical vapor phase deposition

NEP Noise equivallent power

NIR Near infrared range

PL Photoluminescence

PLE Photoluminescence excitation spectroscopy

PNS Photon number splitting attack

QBER Quantum bit error rate

QKD Quantum key distribution

RCLED Resonant cavity light emitting diode

SMF-28 Single mode fiber

SNR Signal to noise ratio

SSPD Superconducting single photon detector

TAC time to amplitude converter

TEM Transmission electron microscopy

VCSEL Vertical Cavity Surface Emitting Lasers

ZPL Zero phonon line

INDEX

The most exciting phrase to hear in science,
the one that heralds new discoveries,
is not "Eureka" (I found it) but
"That's funny.."

— Isaac Asimov

ACKNOWLEDGMENTS

First of all, I would like to thank Prof. Dieter Bimberg for the opportunity to work in his group and on this exciting subject as well as for his steady support of my research.

I am grateful to Prof. Vladimir Haisler for all the support during the last years. Not only once he flew more than 4,000 kilometers to bring new samples and to discuss any kind of physics. I promise to tell you, why we use copper pipes in Germany.

I am deeply indebted to Till Warming, who always found some parameters to adjust, even when everything seemed to be lost. His enthusiasm made staying in the lab the whole night fun and encouraged me when nothing worked.

The Mathe-Mensa gang: I owe a lot of discussions off subject even if we were far away of being experts. Paul, Andreas, Till and Tobias explained me why and more important how the world is turning.

Anatol Lochmann and Waldemar Unrau spent uncountable hours in the clean room under yellow light to process the samples I had the pleasure to measure.

Jan Amaru Töfflinger and Murat Özturk contributed a lot of work during their Diploma-thesis. Together with Alexander Dreismann and Ole Hitzemann they found almost eweri misstacke in tiz woark. I wish them a lot of fun with lonely photons!

Andrei Schliwa I have to thank for his support, proof reading at the last minute and countless discussions. I am sure your are going to fly to a conference on an A380 soon .

The cooperation with Andreas Knorr and Matthias-Rene Dachner helped me a lot to understand phonons and how theorists talk. Probably one of the intense weeks I had with Andreas Baumgartner. The measurements and discussions were so exciting, that we quiet often lost any sense of time.

Sven Rodt helped with any computer problem and was never lack an advice on any kind of questions. Alex Hoffmann played excellently the role of the good soul at the institute. Robert Seguin and Momme Winkelnkemper were excellent fellows since our diploma time. They helped me to feel like a scientist.

I thank all the (former and current) members of the Bimberg group I had the pleasure working with for the collegiate and enjoyable atmosphere.

I thank Sophia for her smile and Yulia for this present and her invaluable support.